



Modeling Galaxy Formation in Cosmological Simulations with CRK-HACC

NICHOLAS FRONTIERE ^{1,2} J.D. EMBERSON ¹ MICHAEL BUEHLMANN ¹ SALMAN HABIB ^{1,2} KATRIN HEITMANN ²
NESAR RAMACHANDRA ¹ AND CLAUDE-ANDRÉ FAUCHER-GIGUÈRE ³

¹*CPS Division, Argonne National Laboratory, Lemont, IL 60439, USA*

²*HEP Division, Argonne National Laboratory, Lemont, IL 60439, USA*

³*Department of Physics and Astronomy and Center for Interdisciplinary Exploration and Research in Astrophysics (CIERA), Northwestern University, Evanston, IL 60201, USA*

ABSTRACT

Self-consistently modeling baryonic effects in survey-scale cosmological simulations has become increasingly important as the diversity, precision, and statistical reach of modern observations continue to improve. The advent of exascale computing now enables a new generation of simulations that couple these physical processes across full-sky volumes with excellent statistical sampling of large-scale structure tracers such as galaxies, groups, and clusters. To support these efforts, we extend the CRK-HACC framework, a GPU-accelerated cosmological hydrodynamics code, with a suite of astrophysical subgrid models that simulate radiative cooling, star formation, stellar evolution, and AGN feedback within a numerically robust formulation optimized for scalability on modern exascale architectures. The models were selected and calibrated to reproduce observed galaxy stellar mass functions over the redshift range $0 < z < 2$ and cluster populations probed by cosmological surveys, capturing the large-scale baryonic evolution relevant for multi-wavelength, cross-correlated analyses. We describe the implementation and calibration of these models and demonstrate their consistency with observed galaxy population statistics and modern hydrodynamic simulations, establishing the baseline for exascale efforts that extend this framework to survey-scale volumes.

Keywords: methods: numerical – cosmology: theory – galaxies: formation – galaxies: evolution

1. INTRODUCTION

Simulating the formation of large-scale structure is a central tool in modern cosmology, providing a major component of the theoretical and modeling foundation for interpreting current and upcoming observational surveys. By solving for the gravitational evolution of matter from primordial fluctuations to the present-day cosmic web, large-volume gravity-only simulations link the initial conditions of the early universe to the complex distribution of galaxies, halos, and clusters observed today. Such simulation efforts offer computational efficiency and have yielded many foundational predictions and insights (see [Angulo & Hahn \(2021\)](#) for a recent review). However, as multi-wavelength surveys have grown increasingly informative, it has become necessary to incorporate baryonic processes through hydrodynamic simulations to produce mock observables and statistical predictions of sufficient fidelity for survey interpretation (e.g., [van Daalen et al. 2011](#); [Harnois-Déraps et al. 2015](#); [Copeland et al. 2018](#); [Chisari et al. 2019](#)).

Accurately modeling baryonic effects requires incorporating astrophysical processes such as radiative cooling, star formation, chemical enrichment, and feedback from supernovae and active galactic nuclei (AGN). These mechanisms operate below the resolution scale of simulations addressing cosmological volumes and must therefore be represented using sub-resolution (“subgrid”) models. As subgrid models are necessarily coarsened and phenomenological representations of the relevant physical processes, they often require calibration against observational constraints, balancing physical motivation with empirical tuning to achieve predictive accuracy.

Incorporating these baryonic processes at cosmological scales is computationally demanding. While many current hydrodynamic simulations are limited to modest box sizes by numerical cost, modern observational surveys increasingly require much larger volumes to capture rare objects, long-range correlations, and the full spatial extent needed for realistic mock survey realizations. This demand has motivated recent large-volume efforts (e.g., MillenniumTNG, [Pakmor et al. 2023](#); FLAMINGO,

Schaye et al. 2023), which trade spatial and mass resolution for cosmological volume.

With the advent of exascale computing and GPU-accelerated architectures, the effective dynamic range can now be expanded by more than an order of magnitude in total particle count and simulated volume, enabling simulations that combine the physical complexity of baryonic processes with the statistical power required for survey-scale analysis. An example is the Frontier-E exascale cosmological simulation (Frontiere et al. 2025), the first trillion-particle-class hydrodynamic run executed on the Frontier exascale system.⁴ Frontier-E evolved four trillion dark matter and baryonic particles to redshift zero within a $\sim 100 \text{ Gpc}^3$ volume, achieving a scale comparable to state-of-the-art gravity-only simulations while self-consistently modeling gas dynamics and astrophysical subgrid processes.

The Frontier-E simulation was performed with the CRK-HACC framework. Originally described by Frontiere et al. (2023) (hereafter **FRO23**), CRK-HACC extends the gravity-only HACC framework developed by Habib et al. (2016), which was designed for extreme scalability on modern supercomputers. It incorporates a high-order Lagrangian smoothed particle hydrodynamics (SPH) scheme to simulate baryonic evolution with high accuracy. In this work, we describe the astrophysical subgrid models implemented in CRK-HACC, which provide the foundation for self-consistent simulations of galaxy formation and feedback in large cosmological volumes, such as those used for Frontier-E.

This study is optimized for the simulation scale required by mock full-sky surveys, where achieving extreme volumes implies a comparatively coarse baryonic mass resolution (on the order of $10^8 M_\odot$ per particle). Within this regime, we prioritize subgrid formulations that are numerically robust while also scalable and GPU-efficient for exascale deployment. This focus contrasts with higher-resolution galaxy-formation and zoom-in studies that aim to resolve the internal structure and morphology of individual galaxies.

Given this scope, we set expectations accordingly. We do not aim to resolve the faintest galaxies, the earliest epochs where our particle masses become limiting, or detailed morphologies and chemical substructure. Instead, our goal is to deliver physically realistic, survey-scale predictions suited for mock all-sky analyses and instrument modeling. These include converged clustering and halo population statistics, realistic galaxy and cluster samples for synthetic survey generation, and large-

scale structure fields suitable for cross-probe predictions across optical, X-ray, and millimeter-band observables. In this context, we focus on reproducing galaxy stellar mass functions consistent with observations over the redshift range $0 < z < 2$ and on modeling cluster density profiles that remain realistic at our mass resolution, establishing the basis for the mock-sky and cosmological analyses enabled by CRK-HACC.

While a number of cosmological simulation codes implement subgrid physics, they differ in their modeling assumptions, numerical coupling strategies, and calibration approaches. Rather than attempting to survey this landscape (see, e.g., Somerville & Davé 2015; Naab & Ostriker 2017; Vogelsberger et al. 2020; Crain & van de Voort 2023 for detailed reviews), we focus here on the specific implementation adopted in CRK-HACC. Our fiducial model was selected after testing a range of candidate strategies from the literature, with final choices and modifications guided by the performance and fidelity requirements of simulating large-scale observational campaigns. A companion paper detailing the Bayesian model calibration procedure is presented in Ramachandra et al. (2025, in prep.).

The manuscript is organized as follows. Section 2 describes the numerical framework and astrophysical subgrid models implemented in CRK-HACC, including radiative cooling, star formation, feedback, and chemical enrichment, all built to support GPU acceleration and parallel scalability. Section 3 outlines the calibration procedure used to tune these models against selected observational benchmarks. Section 4 presents comparisons between the fiducial model and additional, non-calibrated observational measurements to evaluate its broader physical fidelity and overall performance. Finally, Section 5 summarizes the main findings and discusses future directions.

The appendices provide supplementary material, including detailed CRK-HACC solver updates required for subgrid physics (Appendix A), self-similar radiative cooling validation tests (Appendix B), a cluster code comparison study (Appendix C), the construction of the cooling and emissivity tables (Appendix D), and the integrated enrichment model used in our stellar-feedback implementation (Appendix E).

2. SOLVERS AND METHODS

We begin by describing the enhancements to the CRK-HACC framework introduced in **FRO23**, which extend its capabilities by incorporating astrophysical subgrid models that simulate galactic feedback processes within the context of large-scale structure formation. We then detail how these processes are implemented to ensure par-

⁴ <https://www.olcfornl.gov/frontier/>

Table 1. Overview of the physics modeled in CRK-HACC.

| Physical Process | Base Model(s) | Implementation in CRK-HACC |
|---|--|---|
| Gravity & Hydrodynamics Section 2.1 | TreePM + CRKSPH (Habib et al. 2016; Frontiere et al. 2017, 2023). | GPU-accelerated, high-order hydrodynamics and gravity solver using a hybrid particle-mesh and tree-based approach optimized for exascale performance. |
| Radiative Cooling & Heating Section 2.3 | Optically thin, ionization-equilibrium gas with a UV background from Faucher-Giguère (2020) and a metal-line cooling treatment similar to Wiersma et al. (2009). | Modeled consistently using metallicity-scaled, self-shielding-attenuated CLOUDY (Ferland et al. 2017) rates assuming relative solar abundances, applied via a modified exact-integration scheme (Townsend 2009). |
| Star Formation Section 2.4 | Two-phase ISM model (Springel & Hernquist 2003) with a softened equation of state. | Gas transitions smoothly into the ISM above a density threshold, with star formation integrated stochastically. ISM metallicity and helium floors model unresolved early enrichment. |
| Galactic Winds Section 2.5 | Modified kinetic wind model from Vogelsberger et al. (2013); Pillepich et al. (2018a). | Decoupled stochastic winds with energy-based mass loading and dark matter velocity-dispersion scaling (Oppenheimer & Davé 2006). Metal loading regulates ISM entrainment, with density/time-based recoupling. |
| Chemical Enrichment Section 2.6 | Supernovae II/Ia and stellar-wind yields and rates from Hopkins et al. (2023). | Stellar evolution modeled with time- and metallicity-dependent fits to integrated instantaneous rates, enabling exact, continuous tracking of metal and helium enrichment without time-discretization errors. |
| Black Hole Evolution Section 2.7.1–2.7.3 | Conceptual framework from Springel et al. (2005), modeling BHs as collisionless sink particles with separate internal-mass evolution. | Custom implementation with resolution-adaptive seeding at newly formed galaxy centers and stable repositioning-merging procedures that prevent spurious displacements. Unboosted Bondi accretion. Continuous mass growth as in Bahé et al. (2022). |
| AGN Feedback Section 2.7.4 | Two-mode thermal and kinetic AGN feedback model following Weinberger et al. (2016). | Synchronized energy injection with mode set by the Eddington ratio. Thermal feedback deposits heat continuously. Randomly oriented kinetic feedback is triggered when accumulated energy reaches a constant threshold defined by a simplified jet-velocity parameter. |

allel reproducibility and introduce a GPU-accelerated in situ analysis pipeline for galaxy finding, used for efficient black-hole seeding and simulation analysis. Table 1 summarizes the modeled physics, with detailed explanations provided in the sections below. In addition to expanding the scientific capabilities, several modifications to the CRK-HACC solver were required to accommodate subgrid source terms. These algorithmic updates are summarized separately in Appendix A.

Throughout this work, particle positions \mathbf{x}_i and smoothing lengths h_i are expressed in comoving coordinates. Consistent with FRO23, SPH interpolation employs a Wendland (1995) C^4 kernel, $W_{C^4}(|\mathbf{x}_{ij}|, h_i)$, which we denote compactly as $W_{ij}(h_i)$. Here, $|\mathbf{x}_{ij}| \equiv |\mathbf{x}_i - \mathbf{x}_j|$ is the separation between particles i and j . Unless otherwise noted, subgrid relations are formulated in proper units to remain consistent with their physical calibrations. Spatial quantities expressed in proper units are labeled accordingly (e.g., pkpc).

2.1. Gravity and Hydrodynamics

The CRK-HACC framework combines a highly scalable gravitational N -body solver with a modern SPH scheme to model the coevolution of dark matter and baryonic gas during cosmological structure formation. The gravitational potential is decomposed into slow- and fast-varying components, which define the long- and short-range force operators, respectively.

The slow component is computed using a particle-mesh (PM) method with high-order spectral filtering and a distributed FFT implementation, SWFFT,⁵ optimized for large-scale parallel performance. The fast component is handled with a tree-based method designed for GPU acceleration. The combined TreePM solver ensures low-noise force estimates and a compact handover scale, achieving accurate modeling of gravitational interactions across a wide dynamic range

⁵ <https://git.cels.anl.gov/hacc/SWFFT>

while maintaining excellent performance and portability on modern supercomputing architectures (Habib et al. 2016).

CRK-HACC models gas dynamics using Conservative Reproducing Kernel Smoothed Particle Hydrodynamics (CRKSPH), a Lagrangian method that improves upon traditional SPH by exactly reproducing linear fields while conserving mass, momentum, and energy (see Frontiere et al. (2017); henceforth FRO17). The reproducing kernel corrections enhance the accuracy of fluid interpolation and derivative estimates, particularly in shearing and mixing flows. To handle shocks, CRKSPH employs a modified artificial viscosity scheme with a limiter function that suppresses dissipation in smooth regions. The thermal evolution follows a “compatible energy” formalism that ties the energy update directly to the hydrodynamic work, thereby preserving entropy in adiabatic flows. In practice, local hydrodynamic interactions, including neighbor searches and SPH summations, use the same tree structure as the short-range gravity solver, resolving gas and dark matter dynamics at small scales.

An important feature of the combined gravity and hydrodynamics solver is its domain decomposition strategy, which uses “overloading” to duplicate particles near rank boundaries in adjacent domains (summarized in Section 3.4 of FRO23). These overlapping regions, analogous to ghost zones, allow particles to be integrated independently without inter-node communication until they are refreshed and synchronized across ranks at the coarser particle-mesh timescale. This approach maintains scalability and minimizes MPI overhead in large-scale runs, and it is especially effective for the astrophysical models discussed here, which require integration at finer timesteps and would otherwise demand more frequent communication.

2.2. Integration of Subgrid Operators

The gravitational and hydrodynamic solvers are coupled through a symplectic time-integration scheme that supports hierarchical timestepping: long-range gravitational updates are applied at coarser intervals (PM steps) with equal spacing in scale factor, while short-range forces are integrated within smaller, fixed “subcycles.” Hydrodynamic interactions are integrated on progressively finer timescales according to local dynamical CFL conditions, using power-of-two integration bins (see Section 3.1 in FRO23 for a detailed description). Note that we refer to particles as *active* when they are updated on a given timestep and *passive* when they reside on coarser levels of the timestepping hierarchy; this terminology is used throughout the manuscript.

The addition of subgrid operators introduces sources of momentum, energy, and acceleration, along with mechanisms for mass exchange and species tracking, to model complex astrophysical processes such as star formation and galactic feedback. These subgrid operators are coupled at the appropriate timestepping hierarchies (i.e., PM, subcycling, and hydrodynamic timesteps) and are integrated using first-order Strang splitting (Strang 1968).

Specifically, the discretized time propagators for the particle-mesh, short-range, and hydrodynamics operators, $\hat{U}(\Delta t)$, $\hat{U}_{\text{SR}}(\Delta t')$, and $\hat{U}_H(\Delta t'')$, as described by Eqs. (39), (40), and (42) in FRO23, are modified to include subgrid sources as

$$\hat{U}(\Delta t) \rightarrow \hat{U}(\Delta t) \hat{U}_{\text{PM}}^S(\Delta t) \quad (1)$$

$$\hat{U}_{\text{SR}}(\Delta t') \rightarrow \hat{U}_{\text{SR}}(\Delta t') \hat{U}_{\text{SR}}^S(\Delta t') \quad (2)$$

$$\hat{U}_H(\Delta t'') \rightarrow \hat{U}_H(\Delta t'') \hat{U}_H^S(\Delta t'') \quad (3)$$

where each source integrator $\hat{U}_{\{\text{PM}, \text{SR}, H\}}^S$ represents the composite of subgrid operators acting at the corresponding timestepping hierarchy.⁶ Here, Δt , $\Delta t'$, and $\Delta t''$ denote the progressively finer timestep sizes of each timestepping hierarchy.

The primary subgrid operators are composed as follows: the smallest hydrodynamic time interval operators are

$$\hat{U}_H^S = \hat{U}_H^{\text{Z-load}} \circ \hat{U}_H^{\text{recouple}} \circ \hat{U}_H^{\text{conv}} \circ \hat{U}_H^{\text{cool}}, \quad (4)$$

where \hat{U}_H^{cool} is radiative cooling (Section 2.3.2), \hat{U}_H^{conv} is the conversion of ISM gas to stars and wind (Section 2.5.1), and $\hat{U}_H^{\text{recouple}}$ and $\hat{U}_H^{\text{Z-load}}$ are wind recoupling and metal loading (Sections 2.5.2 & 2.5.3), respectively. The intermediate scale operators include

$$\hat{U}_{\text{SR}}^S = \hat{U}_{\text{SR}}^{\text{AGN-feed}} \circ \hat{U}_{\text{SR}}^{\text{AGN-acc}} \circ \hat{U}_{\text{SR}}^{\text{enrich}}, \quad (5)$$

modeling stellar enrichment $\hat{U}_{\text{SR}}^{\text{enrich}}$ (Section 2.6) as well as AGN accretion $\hat{U}_{\text{SR}}^{\text{AGN-acc}}$ and feedback $\hat{U}_{\text{SR}}^{\text{AGN-feed}}$ (Sections 2.7.3 & 2.7.4). Lastly, the PM subgrid operators consist of

$$\hat{U}_{\text{PM}}^S = \hat{U}_{\text{PM}}^{\text{AGN-merge}} \circ \hat{U}_{\text{PM}}^{\text{AGN-repos}} \circ \hat{U}_{\text{PM}}^{\text{AGN-seed}}, \quad (6)$$

which currently include AGN seeding $\hat{U}_{\text{PM}}^{\text{AGN-seed}}$ (Section 2.7.1), as well as merging $\hat{U}_{\text{PM}}^{\text{AGN-merge}}$ and repositioning $\hat{U}_{\text{PM}}^{\text{AGN-repos}}$ (Section 2.7.2).

⁶ \hat{U}_H^S follows the definition in Eq. (38) of FRO23; here, we extend the notation to include analogous source operators \hat{U}_{PM}^S and \hat{U}_{SR}^S for the PM and subcycle (short-range) levels, respectively.

As PM and subcycle timesteps are synchronized across all ranks, subgrid modules introduced at that cadence can be integrated consistently, which is important for particles in shared overloaded regions. For operators applied at the hydrodynamic level, where timestepping can vary between nodes, additional care is required to maintain consistent results (see Section 2.8 for further discussion).

The following sections describe the details of the subgrid implementations and the primary code modifications needed to support them.

2.3. Radiative Cooling and Heating

Radiative cooling and photoheating are fundamental processes in cosmological simulations, governing the formation of stars and galaxies and the thermal evolution of the intergalactic medium (IGM). As is standard in hydrodynamic frameworks (e.g., Illustris-TNG, Vogelsberger et al. 2013; Pillepich et al. 2018a; Horizon-AGN, Dubois et al. 2014; EAGLE, Schaye et al. 2015; SIMBA, Davé et al. 2019), we model the gas as optically thin and in ionization equilibrium, subject to a spatially uniform, time-dependent ultraviolet background (UVB) radiation field adopted from Faucher-Giguère (2020). This approximation avoids the computational cost of full radiative transfer and reionization calculations while capturing the dominant thermal influence of the UVB on diffuse gas in the IGM and circumgalactic medium (CGM).

Additional contributions include inverse Compton cooling off the CMB (e.g., Ikeuchi & Ostriker 1986), metal-line cooling dependent on total metallicity (analogous to the metallicity-scaled formulation in Wiersma et al. 2009), and a density- and redshift-dependent correction for self-shielding attenuation (Eq. A1 in Rahmati et al. 2013). In combination, these terms define a total radiative source function, $\Lambda(u, \rho, Z, Y, z)$, expressed as a function of gas internal energy u , density ρ , metallicity Z , helium fraction Y , and redshift z .

We next describe the metal-line cooling implementation in CRK-HACC, which employs CLOUDY-based rate tables under a scaled-solar abundance approximation. We then outline the exact integration scheme used to apply these rates during the hydrodynamic update (Townsend 2009), eliminating the stiffness and timestep constraints inherent to conventional explicit or implicit solvers.

2.3.1. Metal-Line Cooling

To generate the tabulated cooling and heating source function Λ , we use the photoionization code CLOUDY

version 17.02 (Ferland et al. 2017)⁷. Unlike early treatments that evaluate radiative cooling for a primordial hydrogen–helium mixture (e.g., Katz et al. 1995), CLOUDY self-consistently models the contributions from metal-line cooling. A detailed description of the CLOUDY table generation procedure, including parameter grids, UV background models, and self-shielding corrections, is provided in Appendix D.

Modern hydrodynamic codes (Illustris-TNG, EAGLE, FLAMINGO, Horizon-AGN, etc.) commonly track the abundances of individual gas elements such as carbon, oxygen, and nitrogen produced by chemical enrichment models. Previous studies of metal-line cooling (e.g., Smith et al. 2008; Wiersma et al. 2009) have shown that the cooling contributions of these elements can be tabulated with CLOUDY (or comparable codes) and applied directly to simulated particles. However, such precomputed cooling tables can become prohibitively large, as their dimensionality scales with the number of tracked elements. To mitigate this cost, the contribution of individual elements, assuming solar abundances, can be rescaled to approximate gas cooling for arbitrary compositions, as described by Wiersma et al. 2009.

Similar to the cooling treatment adopted in Illustris-TNG and in simulation codes that incorporate ionization and chemical processes with GRACKLE (Smith et al. 2017), CRK-HACC does not include the cooling contribution of individual metal elements. Instead, cooling rates are computed based on the hydrogen (X), helium (Y), and total metal (Z) mass fractions, assuming that the relative abundances of metals follow the solar pattern.

Specifically, the abundance of each metal element (Z_i) relative to hydrogen is scaled as

$$\frac{n_{Z_i}}{n_H} = R \left(\frac{n_{Z_i}}{n_H} \right)_{\odot}, \quad (7)$$

where the scaling factor $R \geq 0$ is applied uniformly to all metal species with number density n_{Z_i} . Combining Eq. (7) with the definitions of the mass fractions,

$$X = \frac{n_H m_H}{n_H m_H + n_{He} m_{He} + \sum_i n_{Z_i} m_{Z_i}}, \quad (8)$$

$$Y = X \frac{n_{He} m_{He}}{n_H m_H}, \quad (9)$$

$$Z = X \sum_i \frac{n_{Z_i} m_{Z_i}}{n_H m_H} = X R \sum_i \left(\frac{n_{Z_i}}{n_H} \right)_{\odot} \frac{m_{Z_i}}{m_H}, \quad (10)$$

the relationship between R and the total metallicity is given by

$$R = \frac{Z}{X} \left(\frac{X}{Z} \right)_{\odot}, \quad (11)$$

⁷ <https://gitlab.nublado.org/cloudy/cloudy/-/wikis/home>

where $(X/Z)_\odot$ denotes the solar hydrogen-to-metal mass fraction. In our cooling implementation, the index i runs over all 28 metal elements tracked in CLOUDY, each with atomic mass m_{Z_i} . Accordingly, we adopt solar mass fractions of $X_\odot = 0.706498$, $Y_\odot = 0.280555$, and $Z_\odot = 0.012947$, based on the CLOUDY solar composition from Grevesse & Sauval (1998); Holweger (2001); Prieto et al. (2001, 2002).

As described in Appendix D, the tabulated CLOUDY cooling rates Λ are sampled as a function of the metallicity scaling factor R . When particles are radiatively cooled (see Section 2.3.2), the local metallicity Z is converted to R for table lookup, thereby modeling metal-line cooling self-consistently with total metallicity under the assumption of relative solar abundances.

CRK-HACC forgoes individually tracking heavy elements for several practical reasons: 1) the elemental yields of enrichment models remain highly uncertain, 2) the baryon mass resolutions typical of large-volume simulations ($\sim 10^7\text{--}10^8 h^{-1}M_\odot$) are too coarse to reliably evolve detailed chemical abundances, 3) storing individual elemental state variables increases the memory overhead of large simulation campaigns, and 4) the differences in cooling rates between element-by-element and scaled-solar abundance treatments are modest (Wiersma et al. 2009).

To verify this last point, we computed cooling rates with CLOUDY using the individually tracked metal abundances of a random sample of one million particles drawn from the $z = 0$ snapshot of the m12a FIRE-3 simulation (Hopkins et al. 2023; Sultan et al. 2025). This simulation models a $2 \times 10^{12} M_\odot$ halo at $6 \times 10^4 M_\odot$ baryon mass resolution while tracking nine metal element abundances (C, N, O, Ne, Mg, Si, S, Ca, and Fe). The particles were randomly selected with weights chosen so that their metallicity distribution reproduces that of calibrated CRK-HACC runs, ensuring that the test sample reflects the range of values encountered in our simulations. For comparison, we calculated a second set of cooling rates assuming scaled-solar abundances, where the scaling factor R was computed from Eq. (11) using the X and Z values of each randomly drawn FIRE-3 particle. We restrict attention to metal-enriched ($Z/Z_\odot \geq 10^{-4}$) gas particles to avoid cases where metals have negligible impact on cooling.

Figure 1 shows the cumulative distribution function of the relative difference between the two methods for various bins in metallicity. In general, the relative error increases with metallicity but remains modest, with the median error of super-solar metallicity particles sitting in the few-percent range. Overall, we find that 93% (58%) of the sampled particles have relative errors below

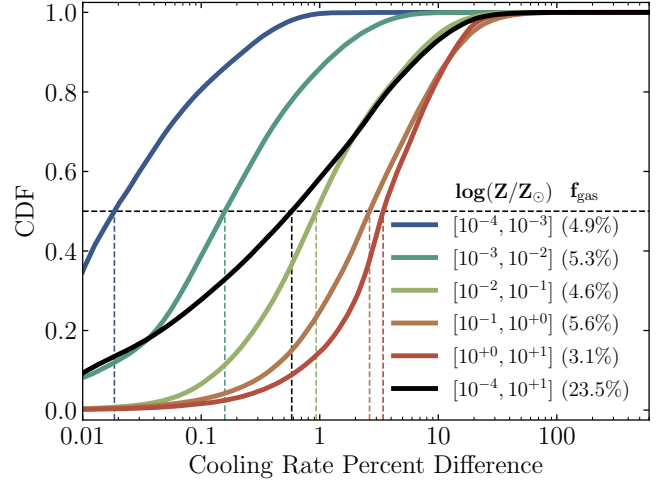


Figure 1. Cumulative distribution function of the relative difference in cooling rates computed with CLOUDY when using individual versus solar-scaled metal abundances. The individual-abundance cooling rates are calculated for one million randomly selected gas particles from the m12a FIRE-3 simulation (Hopkins et al. 2023; Sultan et al. 2025) that tracks nine metal elements. These are compared to rates derived assuming solar-scaled abundances. Square brackets in the legend indicate the metallicity bin of each curve with the round brackets denoting the fraction of CRK-HACC gas particles in that bin. Vertical dashed lines show the median error of each bin. Among metal-enriched gas particles with $Z/Z_\odot \geq 10^{-4}$, we find that 93% (58%) have relative errors below 10% (1%). This translates into 98% (90%) of all simulation particles, confirming that nearly all gas in CRK-HACC cools at rates consistent with element-by-element tracking.

10% (1%). Accounting for the majority of metal-poor ($Z/Z_\odot < 10^{-4}$) gas with minimal metal cooling, this corresponds to roughly 98% (90%) of all gas particles, confirming that the vast majority of particles in CRK-HACC exhibit cooling rates consistent to those obtained from fully element-by-element tracking.

In agreement with MillenniumTNG (Pakmor et al. 2023), we also find that evolving only the total metallicity has minimal impact on the coarse-scale galaxy properties resolved at our simulation resolution, though it can influence the calibration of subgrid parameters against observations. Given the mass resolution limits of large-volume simulations, a more reliable approach for reproducing observable properties is to apply post-processing models for galaxy spectral energy distributions (SEDs), including dust treatment, using observation-driven methods. Our framework employs a stellar population synthesis (SPS) model following Conroy et al. (2009); Conroy & Gunn (2010), applied to the star formation and metallicity histories of each galaxy. In addition, we incorporate Bayesian dust attenuation models from Nagaraj et al. (2022) to gener-

ate narrow-band spectra for individual galaxies. Details of this methodology and the resulting data products—including spectra and photometric catalogs—will be presented in a forthcoming publication.

2.3.2. Exact Integration

Simulated gas is subject to radiative cooling and heating subgrid source terms. The internal energy evolution due to these processes is described by the following ODE:

$$\frac{du}{dt} = -s \frac{\Lambda}{\rho}, \quad (12)$$

where Λ is the energy change per unit time and volume, ρ is the gas density, and $s = \pm 1$ distinguishes cooling ($s = +1$) from heating ($s = -1$).

Eq. (12) can be integrated exactly, following [Townsend \(2009\)](#), under the assumption that the source function Λ depends only on internal energy, while the gas density and chemical composition remain fixed. As the subgrid models in CRK-HACC are implemented using operator splitting (see Section 2.2 and [FRO23](#)), this condition is explicitly maintained, with the gas composition updated only when the density and chemical enrichment operators are performed.

Applying separation of variables to Eq. (12) and integrating across a timestep of length Δt yields

$$\int_{u^0}^{u^1} \frac{du}{\Lambda(u)} = -\frac{s}{\rho} \Delta t, \quad (13)$$

where u^0 and u^1 denote the internal energy of the particle at the beginning and end of the step, respectively. Defining a dimensionless integration function $I(u)$, anchored to a reference energy u_a , as

$$I(u) \equiv s \frac{\Lambda_a}{u_a} \int_{u_a}^u \frac{du'}{\Lambda(u')}, \quad (14)$$

Eq. (13) becomes:

$$[I(u^0) - I(u^1)] \frac{u_a}{s \Lambda_a} = -\frac{s}{\rho} \Delta t, \quad (15)$$

which can be inverted to solve for the internal energy at the end of the step,

$$u^1 = I^{-1} \left[I(u^0) + \frac{\Lambda_a}{u_a \rho} \Delta t \right] = I^{-1}[I(u^1)], \quad (16)$$

using $s^2 = 1$, $\Lambda_a \equiv \Lambda(u_a)$, and $I(u^1) \equiv I(u^0) + \frac{\Lambda_a}{u_a \rho} \Delta t$.

The evaluation of $I(u)$ and its inverse is straightforward when the source function is tabulated for discrete values $\Lambda_k = \Lambda(u_k)$ at logarithmically spaced energies u_k , and interpolated with piecewise power laws,

$$\Lambda(u) = \Lambda_k \left(\frac{u}{u_k} \right)^{\alpha_k}, \quad u_k \leq u \leq u_{k+1}, \quad (17)$$

where $\alpha_k \equiv \log(\Lambda_{k+1}/\Lambda_k)/\log(u_{k+1}/u_k)$ ensures continuity across bin edges. Substituting this form into Eq. (14) yields the recursive relation

$$I(u) = I_k + s \frac{\Lambda_a u_k}{\Lambda_k u_a} \begin{cases} \frac{1}{1-\alpha_k} \left[1 - \left(\frac{u}{u_k} \right)^{1-\alpha_k} \right], & \alpha_k \neq 1 \\ -\ln \left(\frac{u}{u_k} \right), & \alpha_k = 1 \end{cases} \quad (18)$$

with $I_k = I(u_k)$. The inverse function follows similarly as

$$I^{-1} = u_k \begin{cases} \left[1 - (I - I_k)(1 - \alpha_k) s \frac{\Lambda_k u_a}{\Lambda_a u_k} \right]^{\frac{1}{1-\alpha_k}}, & \alpha_k \neq 1 \\ \exp \left[-s \frac{\Lambda_k u_a}{\Lambda_a u_k} (I - I_k) \right], & \alpha_k = 1 \end{cases} \quad (19)$$

valid for $I_k \leq I \leq I_{k+1}$.

In practice, each particle is integrated independently using an anchor value chosen as its initial internal energy, $u_a = u^0$, which sets $I(u^0) = 0$ and $I(u^1) = \frac{\Lambda_a}{u_a \rho} \Delta t$. For heating (cooling) source functions, Eq. (18) is recursively evaluated over successively higher (lower) energy bins starting from the anchor energy. In both cases, $I(u)$ increases monotonically across each bin. The power-law slopes in Eq. (17) are obtained by log-linear interpolation of the tabulated source function at the bin edges, using the fixed particle composition values for density, metallicity, and helium fraction.

The integration proceeds until $I(u)$ exceeds $I(u^1)$, at which point the enclosing bin is identified such that $I_k \leq I(u^1) \leq I_{k+1}$. The corresponding bin edge u_k , together with its stored I_k , is then used to compute the final internal energy u^1 by evaluating Eq. (19) with $I = I(u^1)$.

The integration procedure can employ any bin width, with narrower bins providing a more accurate piecewise power-law representation of Λ . A special case arises when the equilibrium energy is reached, corresponding to the bin where the source function Λ changes sign. Care must be taken in this regime, as the integral diverges when $\Lambda \rightarrow 0$. To ensure numerical stability, we instead integrate that bin using a constant source function defined as the maximum of the two bin-edge values, $\Lambda = \max(\Lambda_k, \Lambda_{k+1})$, and constrain the energy not to exceed the equilibrium value determined by linearly interpolating the zero crossing. Using this approach, the integration converges smoothly in all cases when adopting a conservative bin width of 0.004 dex.

As described in [Townsend \(2009\)](#), the exact integration method offers several advantages over traditional explicit or implicit solvers for internal energy evolution. In particular, it eliminates the need for the small timesteps required by explicit schemes to resolve short cooling times, while also avoiding the multiple roots and

discontinuous solutions that can arise in implicit formulations. The result is a stable and continuous evolution of internal energy across a wide range of thermodynamic conditions.

Arguably, the main drawback of the exact integration method is the potential computational cost associated with frequent tabular lookups of Λ , particularly during the evaluation and inversion of $I(u)$. However, on modern GPUs these table accesses are highly efficient, rendering the cooling kernel subdominant in the overall CRK-HACC timestepping cycle. Consequently, the solver retains the full accuracy of the exact integration scheme while incurring only minimal computational overhead.

A dedicated validation of the radiative cooling module is presented in Appendix B, where we demonstrate that the CRKSPH hydrodynamics solver, combined with the exact integration scheme, reproduces self-similar evolution in idealized, scale-free cosmological simulations.

2.4. Star Formation

Detailed modeling of star formation and the interstellar medium (ISM) is precluded by the limited resolution of cosmological simulations. Consequently, we adopt a coarse-grained subgrid model following [Springel & Hernquist \(2003\)](#) (henceforth [SH03](#)), which represents the ISM as a two-phase medium in which cold, dense clouds are embedded within a hot ambient gas in pressure equilibrium. We summarize the numerical implementation and adopted star formation parameters below and refer the reader to [SH03](#) for a detailed derivation. We also incorporate algorithmic refinements and threshold criteria similar to those used in Illustris-TNG ([Vogelsberger et al. 2013](#)).

While the [SH03](#) model captures the local regulation of star formation within the ISM, it does not include galactic-scale winds that expel gas from galaxies and enrich the surrounding medium. These outflows are modeled separately, with the CRK-HACC implementation described in Section 2.5.

2.4.1. ISM Equation of State

In the [SH03](#) ISM model, the evolution of the two-phase medium is governed by mass and energy exchange between the cold and hot gas components, which occurs through three main channels: 1) cold gas with density ρ_c and internal energy u_c is converted into stars on a characteristic timescale $t_{\text{sfr}}(\rho) \propto \rho^{-1/2}$, consistent with gravitational free-fall and the Schmidt law. A short-lived fraction β of this newly formed stellar population consists of massive stars that promptly explode as core-collapse supernovae, injecting mass and energy into the hot gas phase at a fiducial temperature of $T_{\text{SN}} = 10^8$ K; 2) the supernova energy evapo-

rates additional cold clouds with an efficiency parameter $A_{\text{ev}}(\rho) \propto \rho^{-4/5}$ ([McKee & Ostriker 1977](#)); and 3) radiative cooling at a rate Λ condenses hot gas of density ρ_h and internal energy u_h back into the cold phase, establishing a self-regulated cycle of star formation.

The coupled processes yield an effective equation of state (EOS) that provides pressure support and mitigates runaway gravitational collapse in dense star-forming regions:

$$P_{\text{SH03}} = (\gamma - 1)(\rho_h u_h + \rho_c u_c) = (\gamma - 1)\rho u_{\text{eff}}, \quad (20)$$

where $\gamma = 5/3$ is the adiabatic index of a monatomic ideal gas, and the effective specific energy is given by $u_{\text{eff}} = (1 - x_c)u_h + x_c u_c$, with $x_c = \rho_c/\rho$ defining the mass fraction of gas in cold clouds.

The thermal energy of the cold clouds is fixed at $T_c = 10^3$ K. The remaining quantities, u_h and x_c , follow from the equilibrium solution derived in [SH03](#):

$$u_h = \frac{u_{\text{SN}}}{(A_{\text{ev}} + 1) + u_c}, \quad (21)$$

$$x_c = \frac{2y}{1 + 2y + \sqrt{1 + 4y}}, \quad (22)$$

$$y = \frac{t_{\text{sfr}}\Lambda(u_h, \rho, Z, Y, z)}{\rho[\beta u_{\text{SN}} - (1 - \beta)u_c]}, \quad (23)$$

where the ambient medium approaches equilibrium on a relaxation timescale

$$\tau_{\text{relax}} = t_{\text{sfr}} \frac{(1 - x_c)}{\beta(A_{\text{ev}} + 1)x_c}. \quad (24)$$

To evaluate the core-collapse mass fraction β , we adopt the [Kroupa \(2001\)](#) initial mass function (IMF), a three-part broken power law with slopes $\alpha = \{0.3, 1.3, 2.3\}$ over mass ranges $\{0.01 - 0.08, 0.08 - 0.5, 0.5 - 100\} M_{\odot}$.⁸ Integrating the IMF using a supernova progenitor cutoff of $8 M_{\odot}$ yields a massive star fraction of $\beta = 0.2$.

Equation (20) assumes maximal coupling of supernova feedback energy, which can lead to an overpressurized ISM. Following [Springel et al. \(2005\)](#) and [Hopkins & Quataert \(2010\)](#), we soften the ISM temperature using a dimensionless parameter q_{eos} that interpolates between the effective [SH03](#) model and an isothermal equation of state at $T_{\text{iso}} = 10^4$ K,

$$u_{\text{ISM}} = q_{\text{eos}} u_{\text{eff}} + (1 - q_{\text{eos}}) u_{\text{iso}}. \quad (25)$$

We adopt $q_{\text{eos}} = 0.3$, consistent with the observationally motivated range $q_{\text{eos}} \in [0.1, 0.3]$ from [Hopkins & Quataert \(2010\)](#) and used in [Vogelsberger et al. \(2013\)](#).

⁸ The Kroupa IMF is chosen to maintain consistency with the FIRE-3 stellar enrichment fits described in Section 2.6.

2.4.2. Numerical Implementation

Gas becomes eligible for star formation (SF) only if its hydrogen number density exceeds a fixed threshold, $n_{\text{Hp}} > n_{\text{sfr}} = 0.13 \text{ cm}^{-3}$. Here $n_{\text{Hp}} = \rho X_{\text{p}}/m_{\text{H}}$ is the hydrogen number density evaluated using a fixed primordial composition with $X_{\text{p}} = 0.75$ and $Y_{\text{p}} = 0.25$ in CRK-HACC.⁹ This convention ensures that the star formation threshold remains independent of local gas metallicity.

The density-dependent ISM parameters A_{ev} and t_{sfr} are evaluated using the same hydrogen number density convention:

$$A_{\text{ev}}(\rho) = A_0 \left(\frac{n_{\text{Hp}}}{n_{\text{sfr}}} \right)^{-4/5} \quad \text{and} \quad t_{\text{sfr}}(\rho) = t_0 \left(\frac{n_{\text{Hp}}}{n_{\text{sfr}}} \right)^{-1/2},$$

where the evaporation efficiency and star formation timescale factors are set to $A_0 = T_{\text{SN}}/10^5 \text{ K}$ and $t_0 = 2.2 \text{ Gyr}$, respectively.

For particles exceeding the n_{sfr} threshold, the local ISM energy u_{ISM} is computed from Eq. (25). To suppress spurious star formation in hot, dense gas, particles with $u > u_{\text{ISM}}$ are excluded from star formation eligibility. These particles continue to cool radiatively, but their thermal energy is prevented from dropping below u_{ISM} . Gas with $u \leq u_{\text{ISM}}$ constitutes the ISM phase and evolves thermally toward equilibrium over a relaxation timescale τ_{relax} as follows,

$$u_{\text{sfgas}}^1 = u_{\text{ISM}} + (u_{\text{sfgas}}^0 - u_{\text{ISM}})e^{-\Delta t/\tau_{\text{relax}}}, \quad (26)$$

where the energy is updated from u_{sfgas}^0 to u_{sfgas}^1 over a timestep Δt .

When a gas particle becomes eligible for star formation, we impose a minimum ISM metallicity floor, $Z_{\text{ISM}, \text{min}}$, to model unresolved early enrichment.¹⁰ This floor is set to match the typical ISM metallicity of galaxies with baryonic masses comparable to the simulation mass resolution, which defines the scale of the first resolved stellar populations. Without this floor, newly formed low-mass galaxies would remain artificially metal-poor, requiring delayed self-enrichment to reach the observed mass-metallicity relation (MZR). As shown in Figure 12 and discussed in Section 4.6, the CRK-HACC galaxy MZR at $z = 0$ agrees well with observational data, maintaining consistency even for the smallest resolved systems.

For the simulations presented here, we adopt a metallicity floor of $Z_{\text{ISM}, \text{min}} = 0.25 Z_{\odot}$, consistent with the

MZR of galaxies with stellar mass $M_{\star} \sim 10^8 h^{-1} M_{\odot}$ measured in the FIREBox simulations (Bassini et al. 2024). At this mass scale, the gas-phase metallicity varies by only $\lesssim 0.2\text{--}0.3$ dex over $0 < z < 3$, making a fixed floor adequate for the selected mass resolution. Nonetheless, a redshift-dependent prescription, such as those inferred from observations (e.g., Zahid et al. 2014; Curti et al. 2020; Sanders et al. 2021), can be readily incorporated into the imposed $Z_{\text{ISM}, \text{min}}$.

We likewise impose a floor on the ISM helium fraction by linearly interpolating between the primordial and solar helium abundances using the same fractional factor, $Y_{\text{ISM}, \text{min}} = Y_{\text{p}}(1 - f) + f Y_{\odot}$, where $f \equiv Z_{\text{ISM}, \text{min}}/Z_{\odot}$. As individual elemental abundances are not tracked in this work, disentangling contributions from specific enrichment channels is unnecessary, though such effects could be incorporated with more detailed MZR-based prescriptions.

The relaxation time in Eq. (26) ensures smooth thermal evolution of ISM particles. To maintain thermal energy continuity across the star formation threshold ($n_{\text{Hp}} = n_{\text{sfr}}$), we impose a density-dependent temperature floor that extends smoothly below the transition, motivated by Schaye & Dalla Vecchia (2008); Schaye et al. (2023):

$$u_{\text{min}} = u_{\text{ISM}}(n_{\text{sfr}}) \begin{cases} \left(\frac{n_{\text{Hp}}}{n_{\text{sfr}}} \right)^{1/3}, & n_{\text{sfr}} \geq n_{\text{Hp}} > 10^{-4} \text{ cm}^{-3} \\ 1, & n_{\text{Hp}} > n_{\text{sfr}} \end{cases} \quad (27)$$

where by construction $u_{\text{min}} = u_{\text{ISM}}$ at the density interface.¹¹ Gas particles evaluate $u_{\text{ISM}}(n_{\text{sfr}})$ using the local metallicity and helium fraction (subject to the minimum ISM values $Z_{\text{ISM}, \text{min}}$ and $Y_{\text{ISM}, \text{min}}$), to maintain energy continuity even when enrichment occurs upon crossing the star formation threshold.

To complete the implementation, gas particles governed by the ISM equation of state are not only thermally regulated but also act as sites of star formation by converting cold cloud mass into stars at a rate $\dot{\rho}_{\text{sfr}} \propto \rho_c/t_{\text{sfr}}$. Accordingly, the star formation rate (SFR) \dot{M}_{sfr} for ISM particles of mass m is given by

$$\dot{M}_{\text{sfr}} = \alpha x_c m/t_{\text{sfr}}, \quad (28)$$

where $\alpha = (1 - \beta)$ in the original SH03 formulation accounts for prompt stellar mass loss from core-collapse supernovae. In our implementation, stellar mass loss

⁹ In contrast, the total hydrogen number density n_{H} is computed using the evolved hydrogen mass fraction X from Eq. (8).

¹⁰ Regular gas is initialized with zero metallicity.

¹¹ This condition is applied in addition to the global temperature floor imposed on all baryonic particles, which ensures that no gas cools below the temperature expected from adiabatic expansion since thermal decoupling, i.e. $T > T_{\text{cmb}}/(1 + z_{\text{decouple}}) = 0.02 \text{ K}$, for $z_{\text{decouple}} = 129$.

is modeled explicitly through the chemical enrichment module (Section 2.6), which tracks the evolving stellar population and its ejecta over time. Consequently, adopting an SFR scaling factor of $\alpha = 1$ is more consistent. All star-forming gas particles store the instantaneous local SFR as an additional attribute, which supports downstream analyses of galaxy star formation histories and sets the rate at which gas is converted into stars.

To produce stars at a rate \dot{M}_{sfr} , Eq. (28) is integrated stochastically. Each star-forming gas particle is converted into a collisionless star particle of equal mass with probability

$$p_{\star} = 1 - e^{-\frac{\dot{M}_{\text{sfr}}}{m} \Delta t} \quad (29)$$

evaluated at each timestep.¹² This probabilistic formulation ensures that, on average, stars form at the expected rate while avoiding fractional particle spawning or continuous mass transfer. The integration procedure is extensible and can accommodate additional physics, such as galactic wind modeling, as described in the next section.

Once formed, star particles evolve purely under gravity and no longer participate in hydrodynamic interactions. Each particle represents a single stellar population (SSP) and stores additional properties such as stellar age, birth SFR, and initial stellar mass. These quantities are retained for analysis and for use in subsequent subgrid models, including chemical enrichment as described in Section 2.6.

2.5. Galactic Winds

Galactic winds are large-scale gas outflows driven by stellar feedback processes, including core-collapse supernovae, radiation pressure from young stars, and stellar winds from massive stars. Although the SH03-inspired model depicts the multiphase structure of the ISM and regulates star formation through an effective equation of state, it does not model bulk outflows from galaxies. As a result, galactic winds must be implemented separately to regulate star formation, mitigate runaway cooling, and enrich the circumgalactic medium (CGM). In our implementation, we adopt a subgrid wind model similar to that used in the Illustris-TNG simulations (Vogelsberger et al. 2013; Pillepich et al. 2018a).

In this model, wind particles are stochastically launched from star-forming regions at an outflow rate

\dot{M}_{w} proportional to the local star formation rate,

$$\dot{M}_{\text{w}} = \eta_{\text{w}} \dot{M}_{\text{sfr}}, \quad (30)$$

where η_{w} is the mass loading factor that controls the amount of gas ejected per unit stellar mass formed.

Wind particles are hydrodynamically decoupled from the surrounding gas upon launch, allowing them to escape the dense ISM and propagate into the CGM before recoupling based on local gas conditions. We have found that decoupled wind models facilitate robust convergence and simplify the calibration of multiredshift observables, such as the galaxy stellar mass function (see Figure 3). However, fully coupled wind schemes (e.g., Dalla Vecchia & Schaye 2008) can yield markedly different internal galaxy morphologies. While CRK-HACC does not aim to resolve internal galactic structure in detail, both decoupled and coupled wind formulations are implemented to enable broader experimentation and model flexibility.

The wind launch velocity v_{w} is tied to the local dark matter velocity dispersion σ_{DM} , following Oppenheimer & Davé (2006), with an added redshift-dependent scaling from the Illustris-TNG model:

$$v_{\text{w}} = \kappa_{\text{w}} \sigma_{\text{DM}} \left(\frac{H_0}{H(z)} \right)^{1/3}, \quad (31)$$

where κ_{w} is a dimensionless calibration parameter. The Hubble scaling compensates for the higher characteristic densities of virialized halos at early times, yielding wind velocities that are roughly redshift-independent (see Figure 6 of Pillepich et al. 2018a).

Unlike the Illustris-TNG model, we do not impose a minimum velocity floor or include a separate thermal energy component in the wind. Instead, the mass loading factor is computed directly from the available supernova energy per unit stellar mass:

$$\eta_{\text{w}} = \frac{2}{v_{\text{w}}^2} E_{\text{w}}, \quad \text{with} \quad E_{\text{w}} = e_{\text{w}} \cdot E_0. \quad (32)$$

Here e_{w} is a dimensionless calibration parameter, and E_0 is the specific energy available from core-collapse supernovae per solar mass of stars formed. For consistency, we adopt the normalization of Vogelsberger et al. (2013), $E_0 = 1.73 \times 10^{-2} \times 10^{51} \text{ erg } M_{\odot}^{-1}$, corresponding to 10^{51} erg per event and 1.73×10^{-2} supernovae per solar mass of star formation.¹³

¹² For star-forming gas particles, a timestep constraint $\Delta t < m/\dot{M}_{\text{sfr}}$ is imposed in addition to the standard hydrodynamic CFL conditions described by Eqs. (47)–(49) of FRO23.

¹³ Vogelsberger et al. (2013) assumes a Chabrier (2003) IMF, whereas our subgrid models adopt a Kroupa (2001) distribution. The latter yields a core-collapse event rate of 1.05×10^{-2} per solar mass, implying that our e_{w} values would increase by a factor of 1.65 to match the IMF normalization used in our simulations.

2.5.1. Numerical Implementation

The calibrated wind parameters at the resolution used in this study are $\kappa_w = 3.0$ and $e_w = 0.5$ (see Section 3). The dark matter velocity dispersion σ_{DM} required in Eq. (31) is computed by evaluating the velocity moments of nearby dark matter particles within a fixed proper radius of 30 pkpc around each gas particle. This radius provides a stable, local estimate of the gravitational potential while minimizing sensitivity to small-scale velocity noise.

For each wind particle at position \mathbf{x}_i , we compute an SPH-weighted mean dark matter velocity using the standard Wendland (1995) kernel with smoothing length selected to be $h_\sigma = 30$ pkpc:

$$\langle \mathbf{v}_{\text{DM}} \rangle_i = \frac{\sum_{j \in \text{DM}} \mathbf{v}_j W_{ij}(h_\sigma)}{\sum_{j \in \text{DM}} W_{ij}(h_\sigma)}, \quad (33)$$

summing over all neighboring dark matter particles within the kernel support. The local velocity dispersion is then given by

$$\sigma_{\text{DM},i}^2 = \frac{1}{3} (\langle \mathbf{v}_{\text{DM}} \cdot \mathbf{v}_{\text{DM}} \rangle_i - \langle \mathbf{v}_{\text{DM}} \rangle_i \cdot \langle \mathbf{v}_{\text{DM}} \rangle_i), \quad (34)$$

where angle brackets denote SPH-weighted spatial averages throughout.

The stochastic procedure for producing wind particles at the proper outflow rate \dot{M}_w follows Vogelsberger et al. (2013). Since both stars and winds originate from the ISM reservoir, we calculate a total mass conversion rate

$$\dot{M}_{\text{tot}} = \dot{M}_{\text{sfr}} + \dot{M}_w = (1 + \eta_w) \dot{M}_{\text{sfr}}. \quad (35)$$

The probability that a star-forming gas particle is converted into either a star or a wind particle during a timestep Δt is then

$$p_{\text{event}} = 1 - e^{-\frac{\dot{M}_{\text{tot}}}{m} \Delta t}. \quad (36)$$

By definition, this expression reduces to Eq. (29) when the wind outflow rate is zero. If an event occurs, the conditional probabilities for the resulting particle type follow

$$\begin{aligned} p(\star | \text{event}) &= \frac{\dot{M}_{\text{sfr}}}{\dot{M}_{\text{tot}}}, \\ p(w | \text{event}) &= \frac{\dot{M}_w}{\dot{M}_{\text{tot}}} \equiv 1 - p(\star | \text{event}). \end{aligned} \quad (37)$$

Numerically, each star-forming gas particle draws two random numbers, r_1 and r_2 , from a uniform distribution in the range $[0, 1]$. If $r_1 < p_{\text{event}}$, a conversion occurs: a star particle is spawned if $r_2 < p(\star | \text{event})$; otherwise, a wind particle is launched. In both cases, the spawned

particle inherits the parent gas mass, ensuring that, on average, mass is converted at the total rate \dot{M}_{tot} , with stars and winds forming at their respective rates \dot{M}_{sfr} and \dot{M}_w .

Following Pillepich et al. (2018a), winds are launched isotropically with velocity $\mathbf{v}_w = v_w \mathbf{n}_w$, where \mathbf{n}_w is a randomly oriented unit vector assigned for each launch event. As described in Section 2.8, we employ a counter-based random number generator (CBRNG) that uses the particle ID (unique integer label) and global timestep as input keys. This approach ensures that wind particles spawned in overloaded regions are consistent across MPI ranks without requiring communication. The same procedure is applied to assign directions for kinetic AGN feedback, as discussed in Section 2.7.4.

Once launched, wind particles record their age t_{wind} , launch velocity v_w , and mass loading factor η_w for diagnostics and analysis. While wind particles evolve without hydrodynamic force interactions, they are explicitly included in local gas density estimates:

$$\rho_i = \frac{\sum_{j \in g \uplus w} m_j V_{j,g \uplus w} \mathcal{W}_{ij}^R}{\sum_{j \in g \uplus w} V_{j,g \uplus w}^2 \mathcal{W}_{ij}^R}, \quad (38)$$

where \mathcal{W}_{ij}^R is the CRK-HACC reproducing kernel function described by Eq. (A1) in Appendix A.1. This formulation is identical to the gas density equation used in our previous studies (FRO17 & FRO23), with the modification that the particle volume definition extends to include wind particle neighbors if present, as does the summation above (denoted by $g \uplus w$, the disjoint union of gas and wind particle sets), as discussed in Appendix A.2.

2.5.2. Wind recoupling

Wind particles remain hydrodynamically decoupled until one of two recoupling criteria is met, following the Illustris-TNG model: (a) the local gas density drops below 5% of the star formation threshold, $\rho_{\text{couple}} = 0.05 \rho_{\text{sfr}}$; or (b) the particle has traveled for longer than 2.5% of the current Hubble time, $t_{\text{wind}} > 0.025 H_0^{-1}$. Consistent with Pillepich et al. (2018a), we find that the time criterion is rarely exceeded before the density threshold is satisfied. We support an option for decoupled wind particles to remain subject to radiative cooling and UV photoheating (see Section 2.3), which reduces spurious transients during reintegration. Once a recoupling condition is met, the wind particle is converted back into a hydrodynamically active gas particle.

2.5.3. Wind Metal Deposition

In addition to carrying mass and energy, galactic winds transport metals from the ISM into the circumgalactic medium. To model this process, we follow the

approach of [Vogelsberger et al. \(2013\)](#) and introduce a metal loading factor, γ_w , which controls the fraction of metals entrained by wind particles.

When a wind particle is launched, it inherits a fraction γ_w of the parent star-forming gas particle metal mass:

$$m_{Z_w} = \gamma_w m_{Z_{\text{ISM}}}. \quad (39)$$

The remaining fraction, $(1 - \gamma_w)$, is deposited locally into the ISM. The deposition follows SPH weighting, where each gas neighbor j with volume $V_{j,g}$ (see Eq. (A5)) receives a metal mass

$$m_{Z_{\text{deposit},j}} = A V_{j,g} W_{ij}(h_w) (1 - \gamma_w) m_{Z_{\text{ISM}}}, \quad (40)$$

with normalization

$$A = \left(\sum_j V_{j,g} W_{ij}(h_w) \right)^{-1}. \quad (41)$$

The kernel shape and wind smoothing length, h_w , are identical to those used in the hydrodynamic force solver for regular gas. Metallicities are updated accordingly as $Z_w = m_{Z_w}/m_w$ and $Z_{\text{ISM},j} = (m_{Z_{\text{ISM},j}} + m_{Z_{\text{deposit},j}})/m_{\text{ISM},j}$, leaving the total particle masses unchanged. Neighbors with metallicities exceeding $Z_{\text{max}} = 20 Z_{\odot}$ are excluded from both enrichment and normalization, although such cases are rare.

This deposition model is motivated by both physical and numerical considerations. Physically, galactic winds may preferentially entrain newly synthesized metals from supernova ejecta, enhancing metal transport into the CGM. Numerically, at finite mass resolution, unregulated metal loading can excessively deplete galaxies of metals, particularly when the resolution is insufficient to capture recycling flows and mixing within the ISM.

In our implementation, we find that maintaining realistic galaxy metallicities at the mass resolution used in this paper (baryon mass $\sim 2 \times 10^8 h^{-1} M_{\odot}$) requires a small value of $\gamma_w \in [0, 0.05]$, which yields the most robust results. We therefore adopt a fiducial value of $\gamma_w = 0$, meaning all metals are deposited locally in the ISM at wind launch.¹⁴ The choice of γ_w is resolution dependent and partly degenerate with the seed metallicity floor imposed on the ISM ($Z_{\text{ISM},\text{min}}$; see Section 2.4.2) when evaluating the galaxy mass–metallicity relation (MZR). The resulting ISM and stellar MZRs at the calibrated resolution of this study are shown in Figure 12 and discussed in Section 4.6.

¹⁴ Although we set $\gamma_w = 0$, metals deposited into the ISM at wind launch can still be transported into the CGM through subsequent gas flows, AGN-driven outflows, and large-scale dynamical evolution.

2.6. Chemical Enrichment

Each star particle in CRK-HACC represents a single stellar population (SSP) whose formation time is recorded at the moment it is converted from ISM gas. From that point onward, we integrate stellar mass-loss rates at every timestep to compute the total mass ($\Delta M_T^{\text{enrich}}$), helium ($\Delta M_Y^{\text{enrich}}$), and metal ($\Delta M_Z^{\text{enrich}}$) returned to the ISM by each SSP.

In the following, we consider stellar enrichment from two primary channels: discrete supernovae (Type Ia and core-collapse SNe) and continuous stellar winds from OB and AGB stars. By default, CRK-HACC adopts enrichment rates and yields from the FIRE-3 model ([Hopkins et al. 2023](#); hereafter **FIRE3**), which provides time- and metallicity-dependent stellar evolution and nucleosynthetic prescriptions.

Briefly summarizing the implementation, FIRE-3 employs the 2021 release of STARBURST99 with rotating stellar tracks from [Leitherer et al. \(2014\)](#), assuming a three-part [Kroupa \(2001\)](#) IMF. Core-collapse SNe yields follow modifications to [Sukhbold et al. \(2016\)](#); Type Ia SNe use the delay-time distribution of [Maoz & Graur \(2017\)](#) with ejecta compositions given by the average of the W7 and WDD2 models from [Leung & Nomoto \(2018\)](#); and continuous OB- and AGB-star winds adopt the STARBURST99 mass-loss rates combined with the yield models of [Cristallo et al. \(2015\)](#) and [Limongi & Chieffi \(2018\)](#). The earlier population-averaged FIRE-2 fits from [Hopkins et al. \(2018\)](#) are also available as an alternative configuration for the enrichment module in CRK-HACC.

2.6.1. Supernovae Mass Loss

Mass loss attributed to supernovae events over a given timestep Δt is calculated as:

$$\Delta M_c^{\text{SN}} = M_* \int_{t_0}^{t_0 + \Delta t} M^{\text{SN}}(t) R^{\text{SN}}(t) f_c^{\text{SN}}(t) dt, \quad (42)$$

where M_* is the initial star particle mass, $M^{\text{SN}}(t)$ is the ejecta mass per event, $R^{\text{SN}}(t)$ is the supernova rate per unit stellar mass, and $f_c^{\text{SN}}(t)$ is the time-dependent mass fraction yield for components $c = \{T, Y, Z\}$.

For Type Ia supernovae, the ejecta mass per event is fixed at $M^{\text{Ia}} = 1.4 M_{\odot}$, and the expelled material is assumed to be hydrogen- and helium-free ($f_T^{\text{Ia}} = f_Z^{\text{Ia}} = 1$, $f_Y^{\text{Ia}} = 0$). Thus, $\Delta M_T^{\text{Ia}} = \Delta M_Z^{\text{Ia}}$ and $\Delta M_Y^{\text{Ia}} = 0$. The SNIa rate, $R^{\text{Ia}}(t)$, is modeled as a power law (Eq. (3) in **FIRE3**) and is non-zero for stellar ages $t > 44$ Myr.

For core-collapse supernovae, the event rate $R^{\text{CC}}(t)$ is a piecewise power law (Eq. (2) in **FIRE3**), active over the stellar-age interval $3.7 \text{ Myr} \leq t \leq 44 \text{ Myr}$. CC events adopt a time-dependent ejecta mass $M^{\text{CC}}(t)$ and

yields $f_c^{\text{CC}}(t)$ with coefficients given in Eq. (7) and Table 1 of FIRE3.¹⁵ In both cases, Eq. (42) is integrated analytically, with closed-form solutions provided in Appendix E.1.

2.6.2. Stellar Outflows

Continuous stellar mass loss over the SSP lifetime, primarily from OB and AGB winds, is computed as

$$\Delta M_c^{\text{w}} = M_* \int_{t_0}^{t_0 + \Delta t} f_w(t) f_c^{\text{w}}(t) dt, \quad (43)$$

where $f_w(t)$ is the total wind mass-loss rate per unit stellar mass, and $f_c^{\text{w}}(t)$ is the yield fraction for each component.

The wind rate combines separate OB and AGB contributions, $f_w(t) = f_w^{\text{OB}}(t) + f_w^{\text{AGB}}(t)$, both given by Eq. (4) in FIRE3. OB winds are active for $t < 20$ Myr, while AGB winds become significant at later times ($t \approx 800$ Myr). OB winds depend on progenitor metallicity via fitted coefficients in a piecewise power law model, whereas AGB winds are metallicity-independent but have a more complex time dependence. For most elements, stellar wind yields match the progenitor abundances, but special channels for He, C, N, and O are tracked separately (Eq. (8) in FIRE3).

Equation (43) cannot be integrated analytically for all inputs, as several fitted segments from FIRE3 lack exact closed-form solutions. We therefore numerically integrate and fit the cumulative mass loss for the total, helium, and metal components (combining all individual channels). Table 5 in Appendix E.2 lists the fitted functions used in practice.

2.6.3. Numerical Implementation

At each timestep, the total mass for each component returned by all enrichment sources is

$$\Delta M_c^{\text{enrich}} = \Delta M_c^{\text{Ia}} + \Delta M_c^{\text{CC}} + \Delta M_c^{\text{w}}. \quad (44)$$

The terms in Eq. (44) correspond to the supernova and stellar wind contributions described above, with analytic and fitted formulations summarized in Appendix E. Although the resulting functional form is somewhat complex, the GPU implementation is straightforward: at each timestep, the cumulative solutions yield $\Delta M_T^{\text{enrich}}$, $\Delta M_Y^{\text{enrich}}$, and $\Delta M_Z^{\text{enrich}}$, which are then redistributed to gas neighbors.

¹⁵ FIRE3 tabulates yields for He and nine individual metal species. In CRK-HACC, we use the total metal return ΔM_Z^{CC} and fit the summed fraction $f_Z(t) = \sum_{i=1}^9 f_{Z_i}(t)$ to the same piecewise form.

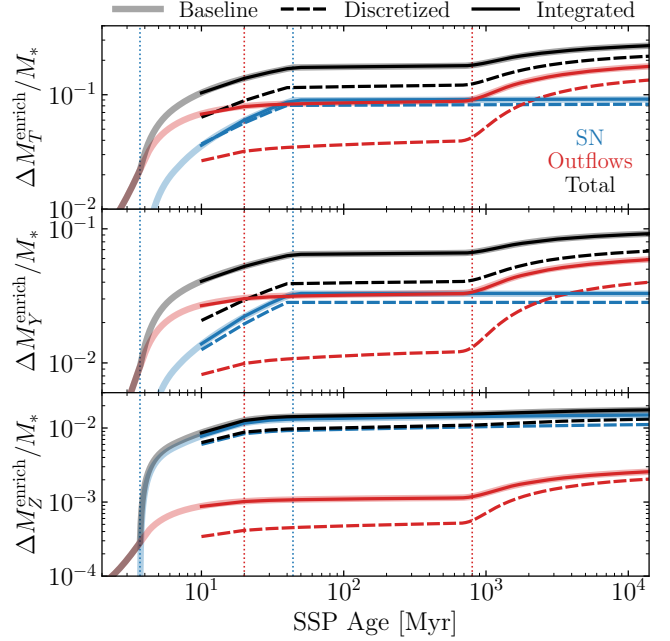


Figure 2. Cumulative mass lost for the total (top), helium (middle), and metal (bottom) mass components of an SSP with solar metallicity, a primordial helium fraction, and initial mass M_* . Blue and red curves separate the mass-loss contributions from supernovae and stellar winds, respectively, and the black curve shows their sum. Solid lines show results from the integrated method using a timestep of 10 Myr, representative of the largest hydrodynamic steps in CRK-HACC. Shaded lines indicate the baseline solution obtained by summing instantaneous FIRE-3 rates over very fine timesteps, while dashed lines show the discretized case, where instantaneous rates are sampled only at 10 Myr intervals. Vertical dotted blue lines mark 3.7 and 44 Myr, the characteristic timescales for core-collapse and Type Ia supernovae, and vertical dotted red lines mark 20 and 800 Myr, corresponding to OB and AGB stellar winds. The timestep-independent integration method matches the baseline to within 2% (set by the accuracy of the implemented fits), whereas coarse discretization of the instantaneous rates suppresses mass loss, primarily due to unresolved early stellar evolution.

Figure 2 shows the cumulative mass loss for the total, helium, and metal components, separating contributions from supernovae and stellar outflows and illustrating the underlying stellar evolution. The integration scheme provides an accurate, timestep-independent cumulative mass loss, analogous to the exact integration cooling treatment described in Section 2.3.2. The integrated method agrees with the baseline solution, obtained by summing the instantaneous FIRE-3 rates over very fine timesteps, with a small residual arising from AGB segments that cannot be integrated analytically. In contrast, evaluating the instantaneous rates only at coarse, discretized hydrodynamic intervals underestimates the

total mass loss by tens of percent due to incomplete sampling of the rapidly varying early stages of stellar evolution. Thus, this integration approach enables large-scale cosmological simulations to capture the cumulative effects of detailed stellar evolution without requiring prohibitively fine temporal integration.

The ejected mass is transferred to neighboring gas particles using SPH kernel weighting, while the star particle mass is reduced accordingly. Specifically, the mass component for gas neighbor j increases as

$$\Delta m_{c,j} = A V_{j,g} W_{ij}(h_*) \Delta M_c^{\text{enrich}}, \quad (45)$$

where h_* is the stellar smoothing length and A is the normalization constant spanning all gas neighbors of the star, analogous to Eq. (41) for wind ISM enrichment. This local coupling conserves mass and species, thereby ensuring consistent ISM enrichment.

To limit mass growth, we enforce that any gas particle with a mass exceeding four times the initial baryon mass is not enriched and is excluded from the normalization. As ISM mass increases only through incremental stellar enrichment, this case is rarely encountered. Consistent with the wind metal loading prescription (Section 2.5.3), outlier gas particles with metallicities exceeding $Z_{\text{max}} = 20 Z_{\odot}$ are likewise excluded from stellar enrichment.

In addition to mass transfer, linear momentum is also explicitly conserved. Star particles are treated as collisionless, so we do not directly apply momentum changes to them during enrichment. Instead, the lost momentum is transferred to neighboring gas particles according to

$$\mathbf{v}_g^{\text{new}} = \frac{m_g \mathbf{v}_g + \sum_{k^*} \Delta m_{T,k^*} \mathbf{v}_{j^*}}{m_g + \sum_{k^*} \Delta m_{T,k^*}}, \quad (46)$$

where k^* indexes all stellar neighbors that contribute mass to a given gas particle. Thus, star particle dynamics are minimally impacted by enrichment, and momentum is transferred to the gas, as is done in other subgrid operators (e.g., wind and AGN feedback).

2.7. Black Holes and AGN Feedback

Feedback from accreting supermassive black holes, commonly referred to as active galactic nuclei (AGN), plays a central role in regulating galaxy formation across cosmic time. Observational and theoretical studies indicate that AGN are required to quench star formation in massive halos, maintain hot gaseous atmospheres in galaxy clusters, and prevent runaway cooling in the cores of massive galaxies (e.g., Fabian 2012; Heckman & Best 2014). In large-scale cosmological simulations, these effects are typically modeled using subgrid prescriptions for black hole (BH) seeding, accretion, growth, and feedback energy injection, following approaches originating

from, e.g., Springel et al. (2005), Sijacki et al. (2007), and Booth & Schaye (2009).

In our simulations, BHs are represented as collisionless sink particles that serve as localized sources of energy and momentum injection into the surrounding medium. They are seeded during the early stages of galaxy formation and grow through gas accretion and mergers with other BHs. Although they do not exert hydrodynamic forces directly and interact with gas only through subgrid prescriptions, they contribute to the gravitational potential and evolve dynamically under gravity like any other collisionless particle (e.g., dark matter or stars). The following subsections summarize the implementation of each major component of AGN evolution.

2.7.1. Seeding

We initialize BHs directly within resolved galaxies. At regular intervals, galaxies are identified on the fly using a GPU-accelerated density-based spatial clustering (DBSCAN; Ester et al. 1996) algorithm applied to the star-particle distribution within each rank, together with a friends-of-friends (FOF; Davis et al. 1985) halo finder executed on all dark matter particles (see Section 2.9 for details). Owing to the efficiency of our GPU-based in situ analysis framework, AGN seeding is performed by default at every PM step. In practice, the results are largely insensitive to the specific interval, provided early galaxy formation is adequately captured.

For each identified galaxy, we define its center as the most bound star particle and construct a 50 pkpc aperture around it to extract all constituent particles, including baryons and nearby dark matter. Galaxies are considered for seeding only if they do not already host a BH particle. To ensure that the galaxy resides within a virialized structure, we locate the dark matter particle closest to the galactic center and verify its FOF group membership. If multiple galaxies exist within the same halo, only the *central* system — defined as the galaxy with the largest stellar mass — is eligible for seeding.

These criteria help suppress numerical artifacts, such as the reseeded of black holes displaced during interactions, and provide greater flexibility across multiple subgrid configurations. In most cases, a single galaxy in a low-mass halo is seeded only once; the additional logic primarily guards against special cases such as flybys or interacting substructures.

This galaxy-based strategy contrasts with the more common approach of seeding black holes at the centers of FOF halos once a fixed mass threshold is exceeded (e.g., Sijacki et al. 2007; Di Matteo et al. 2008). By instead tying BH formation to the resolved stellar mass, we avoid populating halos prematurely and ensure that seeding

occurs only once a galaxy is well formed. Consequently, the seeding prescription remains consistent across different simulation mass resolutions, adapting naturally as higher particle sampling resolves smaller and earlier galaxies that are then seeded accordingly. The FOF halo finder is used solely to verify that the galaxy resides within a virialized halo and to prevent duplicate seeding, not to impose an explicit mass threshold.

A BH is seeded by converting the gas particle closest to the galactic center into a BH particle and repositioning it exactly at that location. The new BH inherits the mass of its parent gas particle. However, this particle mass, m_{BH} , is typically much larger than a realistic astrophysical seed mass. Following the standard practice introduced by [Springel et al. \(2005\)](#), we evolve a separate internal mass, M_{BH} , representing the physical black hole mass used in accretion and feedback calculations. This internal mass is initialized to a calibration parameter M_{seed} , typically in the range 10^5 – $10^6 h^{-1} M_{\odot}$, depending on the simulation resolution. M_{BH} then grows continuously through AGN accretion, while the particle mass remains fixed until synchronization events such as mergers or explicit mass updates, as detailed below.

2.7.2. Repositioning and Mergers

To keep each BH centered within its host galaxy, we apply an explicit repositioning step at every PM update. Candidate locations are selected from star particles within a fixed interaction radius of 10 pkpc, which also sets the maximum allowed BH displacement. The local gravitational potential is computed from these neighboring stars using a softening length of 1 pkpc, and the BH is relocated to the position of the particle with the minimum potential. The BH velocity is then updated to the mass-weighted mean of nearby stars.

The adopted distance scales reflect typical galaxy sizes at intermediate redshift and are chosen to suppress noise in the local potential while preventing the BH from spuriously jumping between galaxies. Although these parameters are tunable, any choice consistent with characteristic galaxy extents yields stable and reliable repositioning. Only stars contribute to the potential calculation and candidate selection, as they trace the collisionless stellar core and are less affected by hydrodynamic forces or transient perturbations. This treatment helps keep the BH anchored to the true galactic center, avoiding misidentification with gas clumps or diffuse dark matter substructure.

BHs are merged when, after repositioning, two or more black hole particles occupy the same spatial location. This situation naturally occurs during galaxy mergers, as the repositioning scheme drives BHs toward

the local stellar potential minimum, ultimately placing them at the same central star particle. This method has proven robust in avoiding premature coalescence or artificial displacements and removes the need for additional merger criteria based on relative velocity or separation, such as those employed by [Springel et al. \(2005\)](#), [Booth & Schaye \(2009\)](#), and [Bahé et al. \(2022\)](#). These alternatives rely on assumptions about black hole kinematics that are not well resolved in our simulations. Likewise, we do not adopt more complex prescriptions such as dynamical friction models (e.g., [Tremmel et al. 2015](#)), as they offer no clear advantage in our context.

Merging is executed in parallel on the GPU using a lock-based protocol that guarantees unique, non-overlapping pairings during each iteration. If a black hole is eligible to merge with multiple partners, atomic locks ensure that only a single merge is carried out per pass, and the routine is repeated until no eligible pairs remain. To maintain consistency across domain boundaries, mergers are allowed only when both black holes are either owned by the same MPI rank or by none (i.e., both are overloaded particles). This restriction may delay a merger by at most one PM step but ensures consistent behavior across overlapping rank domains.

After merging, the resulting BH inherits the center-of-mass position (which, in our implementation, coincides with the original input locations) and the center-of-momentum velocity of the pair. Both the internal and particle masses are summed, and the less massive BH is deactivated (flagged as “dead”) but retained in the simulation for post-processing analysis.

2.7.3. Accretion

We model black hole accretion using the canonical Bondi–Hoyle–Lyttleton formalism ([Hoyle & Lyttleton 1939](#); [Bondi & Hoyle 1944](#)), as is standard in many cosmological simulations. The accretion rate is

$$\dot{M}_{\text{Bondi}} = \alpha \frac{4\pi G^2 M_{\text{BH}}^2 \rho}{(c_s^2 + v_{\text{rel}}^2)^{3/2}}, \quad (47)$$

where M_{BH} is the internal black hole mass, ρ is the ambient gas density and c_s is the local sound speed (both measured within an SPH kernel of smoothing length h_{BH}), and v_{rel} is the relative velocity between the black hole and surrounding gas. The dimensionless factor α serves as a calibration parameter to account for unresolved small-scale gas structure. Following [Weinberger et al. \(2016\)](#), we fix $\alpha = 1$, as its impact is largely degenerate with the seed mass M_{seed} .

Rather than estimating v_{rel} directly, we adopt a fixed sub-resolution value of $v_{\text{rel}} = 8 \text{ km s}^{-1}$, motivated by the typical velocity dispersion of ISM gas ([Dib et al.](#)

2006). This choice avoids artificial divergences in the Bondi denominator and reflects the fact that BH–gas relative velocities are not reliably resolved at our simulation scale. Although v_{rel} is formally tunable, its impact is modest across physically reasonable values (a few to tens km s^{-1}) and does not significantly affect global black hole growth or the star formation history.

To prevent unphysically large accretion rates, we impose an upper limit set by the Eddington rate,

$$\dot{M}_{\text{Edd}} = \frac{4\pi G M_{\text{BH}} m_p}{\epsilon_r \sigma_T c}, \quad (48)$$

where m_p is the proton mass, σ_T is the Thomson cross section, c is the speed of light, and ϵ_r is the radiative efficiency.¹⁶ Typical values of ϵ_r range from 0.1 to 0.2; we adopt $\epsilon_r = 0.2$, consistent with Weinberger et al. (2016). The resulting accretion rate is then

$$\dot{M}_{\text{BH}} = \min(\dot{M}_{\text{Bondi}}, \dot{M}_{\text{Edd}}), \quad (49)$$

which is computed and stored for each black hole after every AGN operator call, including repositioning and merging steps at the PM level, as well as post-feedback updates executed at the end of each gravity subcycle.

The internal black hole mass is updated continuously, following the procedure of Bahé et al. (2022). At each drift timestep (synchronized across all particles; see Appendix A.4), the internal mass increases by

$$\Delta M_{\text{BH}} = (1 - \epsilon_r) \dot{M}_{\text{BH}} \Delta t. \quad (50)$$

When the internal mass exceeds the particle mass ($M_{\text{BH}} > m_{\text{BH}}$), the excess is drawn from neighboring gas particles using SPH kernel weights during each gravity subcycle. The mass contribution from gas neighbor j is

$$\Delta m_j = A V_{j,g} W_{ij}(h_{\text{BH}}) (M_{\text{BH}} - m_{\text{BH}}), \quad (51)$$

where A is a normalization factor defined analogously to Eq. (41). No gas particle is allowed to fall below half its initialized baryon mass; in such rare cases, the residual mass is redistributed to other eligible neighbors in the following subcycle.

Mass transfer also carries momentum. To conserve linear momentum, we preserve gas particle velocities and update the black hole velocity according to

$$\mathbf{v}_{\text{BH}}^{\text{new}} = \frac{m_{\text{BH}} \mathbf{v}_{\text{BH}} + \sum_j \Delta m_j \mathbf{v}_j}{m_{\text{BH}} + \sum_j \Delta m_j}. \quad (52)$$

¹⁶ Super-Eddington accretion is observed and simulated in some contexts (e.g., Jiang et al. 2019; Du et al. 2018), but lies beyond the scope of the simplified subgrid model adopted here, where the Eddington limit serves as a numerical safeguard against unresolved or extreme accretion rates.

This procedure mirrors Eq. (46) for stellar enrichment, where the mass recipient also absorbs the momentum change. Given our fiducial implementation of manual AGN repositioning, this correction has minimal impact on AGN evolution, but is more consequential when employing alternative repositioning or dynamical prescriptions implemented in CRK-HACC.

2.7.4. Feedback

We implement a two-mode AGN feedback model using a modified Illustris-TNG thermal and kinetic scheme (Weinberger et al. 2016). The feedback mode is determined by the dimensionless accretion state parameter

$$\chi = \frac{\dot{M}_{\text{BH}}}{\dot{M}_{\text{Edd}}}. \quad (53)$$

We adopt the same mode-switching threshold,

$$\chi_{\text{thresh}} = \min \left[\chi_0 \left(\frac{M_{\text{BH}}}{10^8 M_{\odot}} \right)^{\beta}, \chi_{\text{max}} \right], \quad (54)$$

using identical parameter values to those in Illustris-TNG: $\chi_0 = 0.002$, $\beta = 2.0$, and $\chi_{\text{max}} = 0.1$, which regulate the thermal-to-kinetic transition.

At each gravity subcycle, the energy released by AGN feedback is computed as

$$\Delta E_{\text{AGN}} = \epsilon \dot{M}_{\text{BH}} c^2 \Delta t, \quad (55)$$

where the effective coupling efficiency ϵ depends on the current accretion mode:

$$\epsilon = \begin{cases} \epsilon_{\text{high}} \epsilon_r, & \chi \geq \chi_{\text{thresh}} \\ \epsilon_{\text{kin}}, & \chi < \chi_{\text{thresh}} \end{cases} \quad (56)$$

with $\epsilon_{\text{high}} = 0.1$ as in Illustris-TNG, and ϵ_{kin} a tunable calibration parameter. Evaluating feedback at the subcycle interval, rather than on the local hydrodynamic timestep, ensures that all gas particles are synchronized at each injection event and that subsequent CFL constraints are immediately enforced.

If the feedback mode is thermal ($\chi \geq \chi_{\text{thresh}}$), the AGN energy ΔE_{AGN} is injected immediately. In the kinetic mode ($\chi < \chi_{\text{thresh}}$), the energy instead accumulates until it exceeds a minimum injection threshold defined as

$$E_{\text{thresh}} = \frac{1}{2} M_{\text{enclosed}} v_{\text{jet}}^2, \quad (57)$$

where $M_{\text{enclosed}} = N_{\text{BH}} \times m_0$ is the idealized enclosed gas mass within the AGN kernel, with $N_{\text{BH}} = 48$ neighbors (see Appendix A.2) and m_0 the initialized baryon particle mass. The parameter v_{jet} serves as a second

tunable calibration constant. We found this constant-threshold formulation numerically preferable to the potentially noisier dark matter velocity dispersion parameterization used in Illustris-TNG (see Eq. 13 in Weinberger et al. 2016).

When feedback energy is injected — either immediately (thermal mode) or after exceeding the threshold (kinetic mode) — it is distributed to neighboring gas particles using SPH kernel weighting:

$$\Delta E_j = A V_j W_{ij}(h_{\text{BH}}) \Delta E_{\text{AGN}}, \quad (58)$$

where the normalization constant A is defined similarly to that used in the accretion and wind enrichment calculations (Eqs. (40) and (51)).

If the feedback mode is thermal, the injected energy is deposited as internal energy:

$$\Delta u_j = \Delta E_j / m_j. \quad (59)$$

If the mode is kinetic, the energy is instead converted into a velocity impulse directed along a single, randomly chosen unit vector \mathbf{n}_{jet} :

$$\Delta \mathbf{v}_j = \sqrt{2 \Delta E_j / m_j} \mathbf{n}_{\text{jet}}. \quad (60)$$

To ensure consistent directionality across MPI ranks for AGNs located in overloaded zones, we employ a counter-based random number generator (CBRNG) seeded by a composite key derived from the unique particle ID and the global accumulated subcycle timestep (see Section 2.8). This guarantees synchronized and reproducible injection without inter-node communication, a practical advantage of injecting feedback at the regular subcycle interval.

If the AGN switches from kinetic to thermal mode before the accumulated energy exceeds the threshold, all stored energy is immediately converted to thermal feedback and injected accordingly. Each black hole particle continuously tracks the accumulated feedback energy as an additional attribute, along with other evolved quantities such as the internal mass M_{BH} , the accretion rate \dot{M}_{BH} , and the particle age (time since seeding). These quantities are updated throughout the simulation and together define the instantaneous state of the AGN model.

2.8. Stochastic Integration and Parallel Reproducibility

Many of the subgrid models introduced above involve stochastic integration or randomized sampling — for example, probabilistically converting star-forming gas into stars, launching galactic winds, or selecting AGN feedback orientations. As the CRK-HACC solver advances

particles independently on each MPI rank during a PM step (using particle overloading), it is important to evaluate stochastic processes consistently across overlapping domain boundaries to maintain parallel reproducibility.

This poses a challenge for subgrid operators that act at the hydrodynamic timestep level, which may vary between ranks depending on local conditions. Unlike the PM and gravity subcycle intervals — which are fully synchronized — local hydrodynamic timesteps may desynchronize stochastic updates if not carefully controlled.

To resolve this, we employ a CBRNG with a key defined by the combination of each particle unique ID and a global timestep counter.¹⁷ The global timestep represents an artificially small integration interval, specified at the start of the simulation, that defines the finest level of the timestep hierarchy. Although particles do not explicitly evolve on this interval, all stochastic integrators do. For example, rather than evaluating the probability of a star-forming gas particle spawning a wind or star over its entire local timestep, we integrate that probability repeatedly at the global timestep scale. This guarantees that stochastic events remain synchronized across ranks, even when local integration intervals differ due to domain decomposition.

Although this approach can require many more random number draws, it remains computationally tractable because the chosen CBRNG (“squares” RNG; Widynski 2020) relies solely on simple multiplication and bitwise operations that are highly efficient on GPUs. Moreover, since stochastic events are integrated independently for each particle, these operations add negligible cost compared to neighbor traversal and force interaction kernels. As such, this strategy ensures consistent stochastic behavior and fully reproducible results across arbitrary parallel decompositions, without requiring additional MPI communication or incurring significant computational cost.

2.9. In Situ Galaxy Finding

The new physics modules implemented in CRK-HACC, while coarsening complex physical processes, are computationally expensive. Increasing the fidelity and diversity of modeled feedback sources drives smaller timesteps and more frequent updates, placing heavy demands on the numerical infrastructure.

¹⁷ Since multiple subgrid operators may require random draws during the same interval, an additional subgrid index key is included to allow for multiple independent random sequences using the same particle ID and timestep counter.

To maintain performance at exascale, CRK-HACC leverages an optimized GPU architecture featuring a tree solver that minimizes rebuild overhead, fully GPU-resident short-range gravity and hydrodynamic kernels that eliminate host-device transfers, and a “warp-splitting” strategy that improves thread occupancy and memory efficiency across interacting particle groups. Together, these optimizations keep more than 90% of the total runtime on device and enable state-of-the-art simulations to complete within a week on modern supercomputers — computations that would otherwise require nearly a year on equivalently scaled CPU systems (Frontiere et al. 2025).

A crucial component of this architecture is the in situ analysis module, implemented through the CRK-HACC framework (see Section 3.8 in FRO23) and extended to meet the demands of subgrid physics. In addition to its native friends-of-friends (FOF; Davis et al. 1985; Klypin & Shandarin 1983) and spherical-overdensity (SO; Lacey & Cole 1994) halo finders, CRK-HACC now supports galaxy identification and measurement.

Galaxies are identified using a GPU-accelerated implementation of the density-based spatial clustering algorithm (DBSCAN; Ester et al. 1996), applied to all stellar particles on each rank. DBSCAN generalizes FOF by introducing a minimum neighbor count parameter, `minPts`, where FOF corresponds to the special case `minPts` = 1. We identify galaxies as DBSCAN clusters using a fixed proper linking length of 50 pkpc and `minPts` = 10. This compact search criterion provides a robust measure of the stellar galactic extent, enabling reliable identification of the stellar potential minimum.

Galaxy properties are then measured using an aperture cutout centered on this position, including all particle species within a fixed radius of $r_{\text{cutout}} = 50$ pkpc. This choice is motivated by De Graaff et al. (2022), who demonstrated using the EAGLE simulation that a 50 pkpc spherical aperture yields stable integrated galaxy measurements across resolution and feedback variations. The same aperture size has since been adopted by more recent simulations such as FLAMINGO (Schaye et al. 2023) and COLIBRE (Schaye et al. 2025).

All clustering operations are executed entirely on GPUs using the open-source ArborX library (Lebrun-Grandié et al. 2020; Prokopenko et al. 2025), enabling structure identification at every PM step with negligible computational overhead. The GPU-accelerated galaxy finder, in particular, supports rapid AGN seeding and efficient galaxy-halo membership tracking, as discussed in Section 2.7.1.

With the full suite of subgrid and analysis components in place, the remaining task is to determine the numer-

ical values of the calibration parameters — specifically, the galactic wind variables κ_w and e_w from Section 2.5, and the AGN model quantities M_{seed} , ϵ_{kin} , and v_{jet} described in Section 2.7. The calibration of these parameters to observational targets is presented in the following section.

3. MODEL CALIBRATION

In gravity-only simulations, the primary model parameters are determined entirely by the chosen cosmology. Hydrodynamic simulations, however, introduce additional complexity through subgrid models that account for a wide range of unresolved baryonic processes. These subgrid models include their own parameters, which must be calibrated against observations to produce realistic predictions.

Model calibration can be performed by running suites of simulations in which subgrid parameters are systematically varied, followed by emulation of the resulting observables to identify the regions of parameter space that best match specific observational targets (e.g., Bower et al. 2010; Jo et al. 2023; Kugel et al. 2023; Chaikin et al. 2025a). This approach enables both the constraint of model parameters and the quantification of degeneracies and uncertainties inherent in subgrid assumptions.

While, in principle, all subgrid parameters could be treated as free, many are physically motivated or theoretically constrained. For example, quantities such as the star formation timescale or metal yields may be based on empirical or theoretical priors and held fixed. In contrast, parameters governing feedback processes — particularly those controlling energy or momentum injection — often encode complex, unresolved physics and require empirical calibration to reproduce key observables such as the galaxy stellar mass function, halo gas fractions, or cluster properties.

A further complication for large-volume simulations is that coarsened subgrid models may exhibit explicit dependence on mass resolution, as is the case in our CRK-HACC implementation. As such, the calibration procedure must be repeated as a function of resolution to maintain consistency across simulation campaigns, similar to the efforts described in Kugel et al. (2023).

The full details of our calibration campaign are presented in Ramachandra et al. (2025, in prep.). Here, we briefly summarize the approach and identify the primary observational targets used to constrain our fiducial model.

3.1. Calibration Parameters

In Section 2, we described the primary subgrid models implemented in CRK-HACC. For calibration, we vary

five physically motivated parameters that govern the strength and character of galactic winds and AGN feedback: the wind velocity scaling κ_w , the supernova energy fraction available for wind injection e_w , the black hole seed mass M_{seed} , the AGN kinetic feedback efficiency ϵ_{kin} , and the jet velocity v_{jet} .

As discussed in Section 2.7.3, the black hole seed mass is largely degenerate with the accretion boost factor α at our examined mass resolution. Rather than varying both simultaneously, we fix $\alpha = 1$ and calibrate M_{seed} to regulate AGN growth and thermal feedback efficiency at our target resolution.

The wind parameters e_w and κ_w directly set the mass loading and velocity of galactic outflows, thereby modulating stellar mass assembly and the star formation rate. Likewise, ϵ_{kin} and v_{jet} determine the onset and effectiveness of AGN-driven kinetic feedback, with important consequences for gas content in massive halos.

Calibration parameters were sampled using a symmetric Latin hypercube design of 64 simulations in an $L_{\text{box}} = 128 h^{-1}\text{Mpc}$ box, complemented by a nested suite of 16 larger-volume runs ($L_{\text{box}} = 256 h^{-1}\text{Mpc}$) to constrain cluster-scale gas profiles. The full parameter ranges and additional calibration results are presented in Ramachandra et al. (2025, in prep.), and the resulting calibrated values adopted in our fiducial model are listed in Table 2.

Table 2. Calibrated subgrid model parameters.

| Parameter | Description | Value |
|-------------------------|------------------------------------|-----------------|
| κ_w | Wind velocity scaling factor | 3.0 |
| e_w | Wind energy factor | 0.5 |
| ϵ_{kin} | AGN kinetic efficiency | 1.3 |
| v_{jet} | AGN jet velocity [km/s] | 5.1 |
| M_{seed} | AGN seed mass [$M_\odot h^{-1}$] | 8×10^5 |

3.2. Calibrated Observables

To constrain our fiducial subgrid model, we calibrate against two categories of observational measurements: galaxy stellar mass functions (GSMFs) and intracluster gas density profiles. The GSMF provides a sensitive probe of the efficiency of star formation and stellar feedback across cosmic time. We use measurements of the GSMF over $0 < z < 2$ to calibrate the galactic wind parameters κ_w and e_w , as well as thermal AGN feedback through the seed mass M_{seed} . The results presented here are based on an $L_{\text{box}} = 256 h^{-1}\text{Mpc}$ calibration run using the fiducial parameter set summarized in Table 2.

The simulation is initialized at $z = 200$ with 1024^3 dark matter particles and an equal number of bary-

onic gas particles. These correspond to particle masses of $m_{\text{dm}} = 1.13 \times 10^9 h^{-1}M_\odot$ and $m_b = 2.12 \times 10^8 h^{-1}M_\odot$, matching the mass resolution calibrated in Ramachandra et al. (2025, in prep.). The gravitational softening length is set to the minimum of $10 h^{-1}\text{kpc}$ (comoving) and $6 h^{-1}\text{kpc}$ (proper), such that the softening follows the comoving scale at high redshift and transitions to a fixed proper value at late times. The adopted cosmology follows Planck Collaboration et al. (2020), with parameters $(\Omega_c, \Omega_b, \sigma_8, n_s, h) = (0.26067, 0.04897, 0.8102, 0.9665, 0.6766)$. This setup represents a down-scaled realization of the Frontier-E simulation (Frontiere et al. 2025), employing an identical parameter configuration.

Figure 3 shows the GSMF measured from the calibrated simulation at redshifts $z = 0, 1$, and 2, using stellar masses within a 50 pkpc aperture. Gray shaded regions denote stellar masses below $M_* \lesssim 10^{10} M_\odot$, corresponding to ~ 30 star particles, where the mass function becomes resolution limited. At low redshift, we compare with measurements from the SDSS and GAMA surveys, reported by Bernardi et al. (2017) and Driver et al. (2022), respectively. At intermediate and high redshift, we include GSMFs from the DEVILS survey (Thorne et al. 2021) and the COSMOS2020 catalog (Weaver et al. 2023). The observational datasets correspond to survey redshift bins that bracket each simulation snapshot, ensuring consistent coverage around the targeted epochs. Across all redshifts, we also show the empirical predictions from the UniverseMachine model (Behroozi et al. 2019), which self-consistently reproduces the observed stellar mass functions, star formation rates, and quenched fractions over $0 < z < 10$. These predictions provide continuous redshift coverage and serve as a reference calibration target for the evolving GSMF.

At all three redshifts, the CRK-HACC results track closely with the UniverseMachine calibration target and, by construction, are consistent with the presented observational datasets. For qualitative comparison, we also include GSMF measurements from several recent cosmological hydrodynamic simulations, including EAGLE (Furlong et al. 2015), SIMBA (Davé et al. 2019), COLIBRE (Chaikin et al. 2025b), Illustris-TNG (Pillepich et al. 2018b), FLAMINGO (Schaye et al. 2023), and MillenniumTNG (Pakmor et al. 2023). These provide representative examples of current large-scale galaxy formation models and help contextualize the calibration of our fiducial subgrid parameters. As expected, the scatter among simulations is modest at $z = 0$, where most models are calibrated to local observables, and increases toward higher redshift as differences in feedback imple-

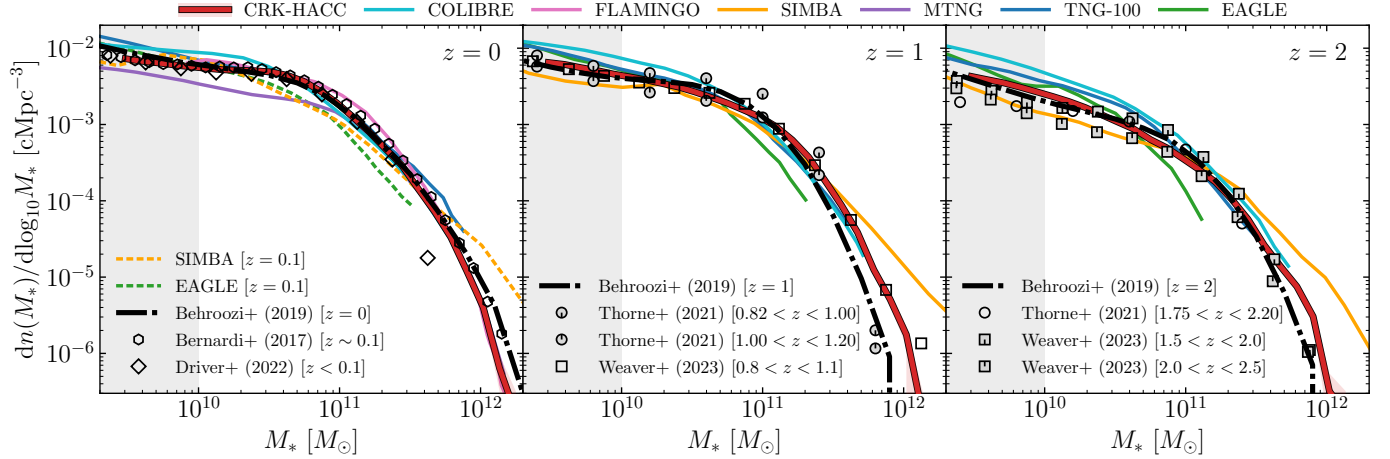


Figure 3. Galaxy stellar mass function (GSMF) measurements from the calibrated CRK-HACC simulation at redshifts $z = 0, 1$, and 2 , with red shaded regions indicating Poisson uncertainties. Gray shaded regions mark the resolution limit of the CRK-HACC results. Observational datasets (Bernardi et al. 2017; Driver et al. 2022; Thorne et al. 2021; Weaver et al. 2023) and empirical predictions from UniverseMachine (Behroozi et al. 2019; the calibration target) are included for reference. Results from selected cosmological hydrodynamic simulations — EAGLE (Furlong et al. 2015), SIMBA (Davé et al. 2019), COLIBRE (Chaikin et al. 2025b), Illustris-TNG (Pillepich et al. 2018b), FLAMINGO (Schaye et al. 2023), and MillenniumTNG (Pakmor et al. 2023) — are also shown for qualitative comparison. The CRK-HACC GSMFs closely match both the observational constraints and the UniverseMachine predictions across all presented redshifts, including at high redshift where the spread among different simulation predictions becomes more pronounced.

mentation and star formation efficiency become more pronounced.

To constrain the AGN kinetic feedback parameters ϵ_{kin} and v_{jet} , we calibrate against low-redshift X-ray measurements of intracluster gas density profiles. Our primary calibration target is the stacked profile of McDonald et al. (2017), derived from deep *Chandra* observations of 27 massive, X-ray-selected clusters at $z \lesssim 0.1$ (originally from the Vikhlinin et al. 2009 sample). As shown in Figure 4, the stacked CRK-HACC profiles are consistent with the target measurement after applying a mass cut of $M_{500c} > 3 \times 10^{14} M_{\odot}$, which yields 37 clusters, comparable to the 27-cluster sample analyzed by McDonald et al. (2017).

We also include the nearby X-COP reference from Ghirardini et al. (2019, 2021), drawn from a 12-cluster Planck-selected sample, and the *eROSITA* all-sky stack of 38 Planck-selected clusters from Lyskova et al. (2023), based on the CHEX-MATE sample (CHEX-MATE Collaboration et al. 2021). The McDonald et al. (2017) and Lyskova et al. (2023) profiles show consistent normalization with CRK-HACC, while the X-COP profiles are systematically higher, collectively spanning the plausible range of gas densities in low-redshift clusters.

For qualitative context, we again include results from several recent cosmological simulations, noting that the exact mass selections and measurement methodologies differ between studies. These comprise TNG-Cluster (Lehle et al. 2024), MillenniumTNG (Pakmor et al.

2023), FLAMINGO (Braspenning et al. 2024), and the SIMBA and GADGET-X clusters from *The Three Hundred Project* (Li et al. 2023). The CRK-HACC profiles lie near the midpoint of the simulation spread and are nearly coincident with the selected MillenniumTNG curve, which corresponds to clusters in the $10^{14.6} < M_{500c}/M_{\odot} < 10^{14.8}$ range.

As an additional validation, we simulate the nIFTy high-mass cluster from Sembolini et al. (2016a,b) in Appendix C, benchmarking the calibrated CRK-HACC model against published radiative cluster simulations. The comparison likewise shows consistency across modern hydrodynamic solvers, with CRK-HACC agreeing with other codes on the cluster profile measurements considered.

Finally, while we calibrate to high-mass cluster gas-density profiles, several large-volume simulations instead target gas fractions in group-scale and low-mass clusters (e.g., McCarthy et al. 2016; Schaye et al. 2023; Kugel et al. 2023). In Ramachandra et al. (2025, in prep.), we tested both observables but found they could not be simultaneously matched within a single subgrid parameter set. Gas-fraction calibration required significantly stronger feedback, whereas the gas-density approach adopted here achieves a better balance with observed low-redshift, high-mass cluster structure.

This calibration choice is particularly well-suited to next-generation, exascale-class simulations, where reproducing realistic massive-cluster profiles is a key ob-

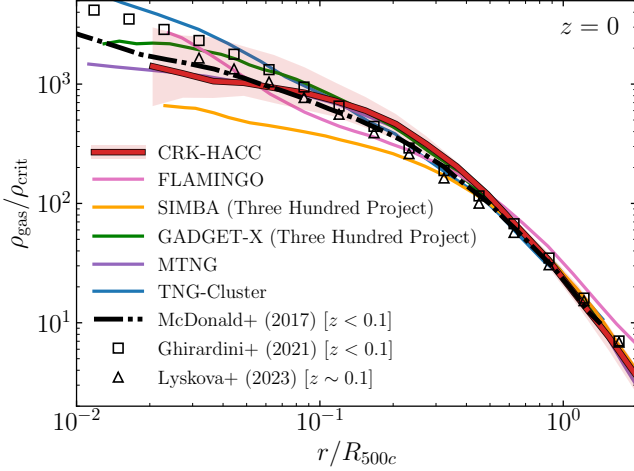


Figure 4. Median cluster gas density profiles from the fiducial CRK-HACC simulation at $z = 0$ for halos with $M_{500c} > 3 \times 10^{14} M_{\odot}$. The shaded region shows the 16th–84th percentile range. Observational measurements are shown from McDonald et al. (2017) (calibration target), Ghirardini et al. (2021), and Lyskova et al. (2023). Results from recent cosmological simulations include TNG-Cluster (Lehle et al. 2024), MillenniumTNG (Pakmor et al. 2023), FLAMINGO (Braspenning et al. 2024), and the SIMBA and GADGET-X clusters from *The Three Hundred* project (Li et al. 2023). The calibrated CRK-HACC profile lies near the midpoint of both the observational and simulation ranges, indicating consistency with current constraints on intracluster gas structure.

jective given the large statistical samples available for study. The Frontier-E flagship simulation, for example, resolves more than 500,000 clusters with $M_{500c} > 10^{14} h^{-1} M_{\odot}$, enabling robust statistical population analyses (Frontiere et al. 2025). The alternative CRK-HACC parameter set calibrated to gas fractions is described in Ramachandra et al. (2025, in prep.) and will be explored in future targeted studies.

In summary, the GSMF and halo profile calibrations jointly constrain our feedback model from galactic to cluster scales, ensuring consistency with the selected observational benchmarks and yielding physically reasonable galaxies and high-mass halos within the calibrated regimes. In the following section, we examine how the fiducial model performs for a broader suite of non-calibrated observables, spanning galaxy scaling relations, baryon fractions, and metallicity trends, to evaluate its predictive fidelity and any residual tensions beyond the direct calibration targets.

4. COSMOLOGICAL SIMULATION MEASUREMENTS

We now evaluate the predictive performance of the fiducial CRK-HACC model against a broad set of ob-

servational benchmarks using the calibrated $L_{\text{box}} = 256 h^{-1} \text{Mpc}$ simulation introduced in Section 3. With its modest volume, this run enables a converged study of galaxy- and halo-scale properties and provides sufficient statistical power to assess how the calibrated feedback and enrichment prescriptions shape galaxy and halo populations across mass and environment. Synthetic sky-projected observables, light-cone measurements, and massive-cluster analyses are deferred to forthcoming studies based on our leadership-class simulations (e.g., Frontier-E; Frontiere et al. 2025), which possess the necessary volume to robustly render these observables.

We begin by examining global stellar evolution and mass buildup across cosmic time (Sections 4.1–4.2), then turn to galaxy-scale properties — sizes, star-formation activity and quenching, and scaling relations in stellar mass, halo mass, and metallicity (Sections 4.3–4.6). We next assess black-hole growth and its co-evolution with host galaxy mass (Section 4.7), and conclude with baryon fraction measurements in massive halos (Section 4.8) to evaluate model performance across environments.

A visual overview of the simulation domain is shown in Figure 5, illustrating the large-scale distributions of gas temperature, metallicity, and density, together with the stellar component produced by the calibrated model. The accompanying analyses draw on a suite of derived physical quantities and structure catalogs generated in situ and subsequently post-processed using our parallel, optimized Python framework HAvCC (the HACC Analysis and Validation to Observational Constraints Code),¹⁸ which performs distributed measurements of halo, galaxy, and environmental properties directly from particle-data outputs.

Throughout this study, we compare results from CRK-HACC with both large-volume simulations, such as MillenniumTNG (MTNG740; Pakmor et al. 2023) and FLAMINGO (L2p8_m9; Schaye et al. 2023), and higher-resolution reference suites, including EAGLE (Ref-L100N1504; Schaye et al. 2015), Illustris-TNG (TNG100 and TNG300; Nelson et al. 2019), SIMBA (m100n1024; Davé et al. 2019), and COLIBRE (L200m6; Schaye et al. 2025). Key numerical parameters for these simulations — box size, particle counts, mass resolution, and gravitational softening — are summarized in Table 3.

When comparing to observational datasets, all stellar quantities have been converted to a Chabrier (2003) initial mass function (IMF) for consistency. For all pre-

¹⁸ <https://git.cels.anl.gov/hacc/HAvCC>

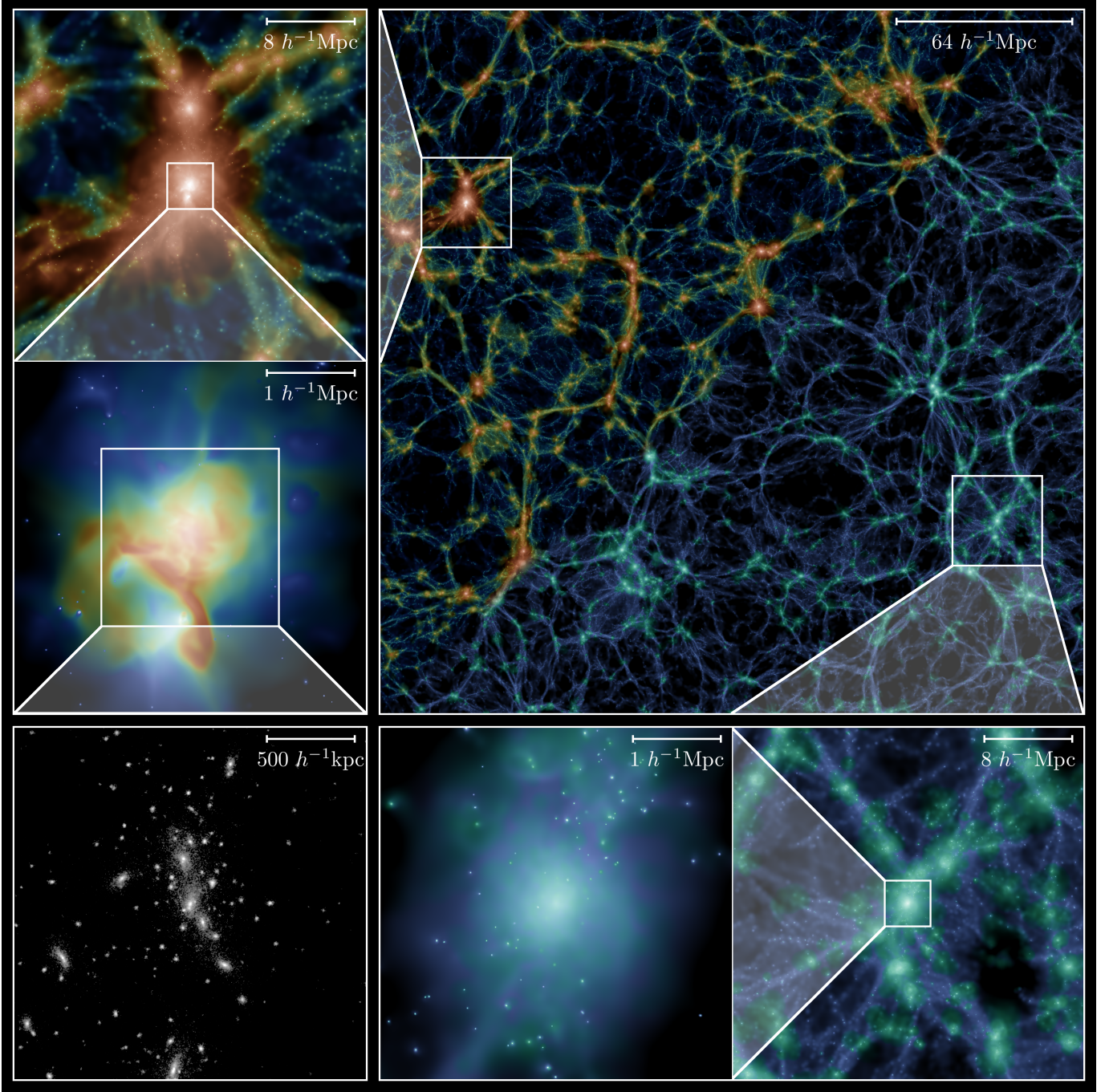


Figure 5. The large central panel shows a slice of the gas density field across the full simulation domain ($256 h^{-1}$ Mpc on a side) with a slice depth of $4 h^{-1}$ Mpc. The left half of this panel is color-mapped by temperature (cold in blue, hot in red), while the right half is color-mapped by metallicity (metal-poor in blue, metal-rich in green). The panels along the left column present successive zooms into the most massive halo in the volume ($M_{200c} = 1.2 \times 10^{15} h^{-1} M_{\odot}$), and the panels along the bottom row show progressive zooms into a second massive cluster ($M_{200c} = 1.4 \times 10^{14} h^{-1} M_{\odot}$). The lower-left panel shows the stellar density field in the central region of the largest halo.

sented CRK-HACC results involving galaxy stellar mass, gray shaded regions denote $M_{*} \lesssim 10^{10} M_{\odot}$ (approximately 30 star particles), indicating the mass resolution limit as in the calibration figures.

These comparisons are used to identify where the coarsened model predictions are consistent with established simulation results despite differences in resolution and calibration, and where reduced sampling and force

Table 3. Summary of comparison simulations referenced in this study. Listed are the comoving box length L_{box} , number of gas and dark matter particles ($N_{\text{gas,DM}}$), baryon and dark matter particle masses (m_b , m_{dm}), gravitational softening length ϵ_{soft} , and the primary reference.

| Name | L_{box} [Mpc] | $N_{\text{gas,CDM}}$ | m_b [M_{\odot}] | m_{dm} [M_{\odot}] | ϵ_{soft} [pkpc] | Reference |
|-----------------------|------------------------|--|-----------------------|---------------------------------|---------------------------------|----------------------|
| CRK-HACC ^a | 378.4 | 1024 ³ | 3.1×10^8 | 1.7×10^9 | 8.9 | this work |
| FLAMINGO (L2p8_m9) | 2800 | 5040 ³ | 1.1×10^9 | 5.7×10^9 | 5.7 | Schaye et al. (2023) |
| MillenniumTNG | 740 | 4320 ³ | 3.1×10^7 | 1.7×10^8 | 3.7 | Pakmor et al. (2023) |
| TNG300 | 302.6 | 2500 ³ | 1.1×10^7 | 5.9×10^7 | 1.5 | Nelson et al. (2019) |
| SIMBA (m100n1024) | 147.1 | 1024 ³ | 1.8×10^7 | 9.6×10^7 | 0.7 | Davé et al. (2019) |
| EAGLE (Ref-L100N1504) | 100 | 1504 ³ | 1.8×10^6 | 9.7×10^6 | 0.7 | Schaye et al. (2015) |
| TNG100 | 110.7 | 1820 ³ | 1.4×10^6 | 7.5×10^6 | 0.7 | Nelson et al. (2019) |
| COLIBRE (L200m6) | 200 | 3008 ³ (4×3008^3) ^b | 1.8×10^6 | 2.4×10^6 | 0.7 | Schaye et al. (2025) |

^a Down-scaled calibration run of the 4655.6 Mpc Frontier-E simulation (Frontiere et al. 2025).

^b COLIBRE simulates four times more dark matter than gas particles to maintain nearly uniform particle masses.

resolution begin to limit physical fidelity. In doing so, we aim both to demonstrate the physical realism of stellar and baryonic buildup within the survey-scale regime targeted by CRK-HACC and to delineate where resolution limitations impact predictions — for example, in high-redshift star formation or the internal structure of individual galaxies. Naturally, the reference simulations themselves exhibit non-negligible differences across several regimes, as well as inconsistencies with observations, so agreement or tension among models should be interpreted as an indicator of relative rather than absolute physical fidelity.

4.1. Cosmic Star Formation Rate Density

We begin by examining the cosmic star formation rate density (CSFRD), a well-studied global diagnostic of galaxy formation models that traces the buildup of stellar mass across cosmic time. Observationally, the CSFRD rises rapidly from the early universe, peaks near $z \sim 2$, and declines by nearly an order of magnitude to the present day. In CRK-HACC, we measure the CSFRD from the instantaneous star formation rates of gas particles at each PM timestep.¹⁹

Figure 6 compares the CSFRD from the fiducial CRK-HACC simulation with recent observational constraints (Bouwens et al. 2015; Novak et al. 2017; Traina et al. 2024) and with predictions from representative hydrodynamical simulations (EAGLE; Furlong et al. 2015, Illustris-TNG and MillenniumTNG; both from Pakmor et al. 2023, SIMBA; Davé et al. 2019, and FLAMINGO; Schaye et al. 2023). We also include the data compila-

tion of Behroozi et al. (2019), showing both their aggregated pre-2016 multiwavelength CSFRD measurements (listed in their Table C3) and the associated empirical UniverseMachine model curves that self-consistently link galaxy star formation to halo growth. The observational datasets span complementary tracers, including rest-frame UV at high redshift (Bouwens et al. 2015), dust-unbiased radio estimates (Novak et al. 2017), and infrared/submillimeter measurements (Traina et al. 2024), while the UniverseMachine framework provides a synthesis of earlier surveys and a bias-corrected baseline for comparison.

At high redshift ($z \gtrsim 3$), CRK-HACC predicts a lower CSFRD than both the UV-based estimates of Bouwens et al. (2015) and the higher-resolution hydrodynamical simulations. This difference reflects the relatively coarse mass resolution of the CRK-HACC results — set to match the configuration of survey-scale production runs — compared to simulations such as Illustris-TNG, MillenniumTNG, EAGLE, and SIMBA, which better resolve the population of faint, low-mass halos that dominate early star formation (see Table 3). By contrast, FLAMINGO employs a comparable resolution and likewise shows a suppression at high redshift, though with a somewhat steeper recovery toward intermediate epochs.

Between $z = 3$ and $z = 0$, CRK-HACC converges with the other hydrodynamical simulations, generally tracking the middle of their spread. Relative to the observational data, the CRK-HACC CSFRD agrees well with the measurements of Novak et al. (2017) and Traina et al. (2024) across most of the resolved redshift interval. Divergences appear primarily at the highest measured redshifts, where observational uncertainties increase and the CRK-HACC estimate falls below the data due to limited resolution. In contrast, the simulation remains

¹⁹ Integrating the stellar mass formed over each step, using the initial masses of newly created star particles, yields a consistent CSFRD measurement.

below the Behroozi et al. (2019) compilation and the “observed” CSFRD predicted by UniverseMachine, which reproduces the higher normalization of those datasets (light-gray shaded curve and points in Figure 6).

The discrepancy between star-formation rate indicators and the growth of the stellar mass density is a long-recognized problem (e.g., Wilkins et al. 2008; Leja et al. 2015; Yu & Wang 2016), and it provides the motivation for the bias framework adopted in UniverseMachine. In this model, redshift-dependent corrections are applied, with the strongest adjustments at $z \sim 2$, the epoch of peak star-formation activity, where the tension is most severe, and modest reductions at higher redshift. This yields a lower, bias-corrected “true” CSFRD estimate that falls below the observational compilations near the peak epoch (dark-gray shaded curve).

Interestingly, CRK-HACC follows the “true” UniverseMachine prediction very closely, matching both shape and normalization from $z \sim 4$ to $z = 0$. This consistency is notable, given that the CSFRD was not part of the calibration (Section 3), which relied solely on the galaxy stellar mass function (spanning $0 < z < 2$) and low-redshift cluster density profiles. While the agreement may be partly coincidental, it suggests that the calibrated model reproduces the global efficiency of star formation in a manner consistent with empirically bias-corrected expectations.

4.2. Cosmic Stellar Mass Density

A complementary observable to the cosmic star formation rate density is the buildup of the cosmic stellar mass density (CSMD), which provides a cumulative record of how efficiently baryons are converted into long-lived stars. Whereas the CSFRD measures the instantaneous rate of star formation, the CSMD integrates this history over cosmic time (accounting for stellar mass loss) and tests whether a simulation reproduces the observed stellar mass assembly.

Figure 7 compares the evolution of the CSMD from the fiducial CRK-HACC run (computed for stars in galaxies and for the total simulated volume) against recent observational estimates and predictions from three other hydrodynamical simulations. The observational datasets span a broad redshift range and include the compilation of Madau & Dickinson (2014), the homogeneous multi-survey analysis of Driver et al. (2018), the COSMOS2020 stellar mass functions of Weaver et al. (2023), and the recent JWST-based measurements of Shuntov et al. (2025). We also include predictions from the COLIBRE (Chaikin et al. 2025b), EAGLE (Furlong et al. 2015), and SIMBA (Thomas et al. 2019) simulations, which serve as representative benchmarks for

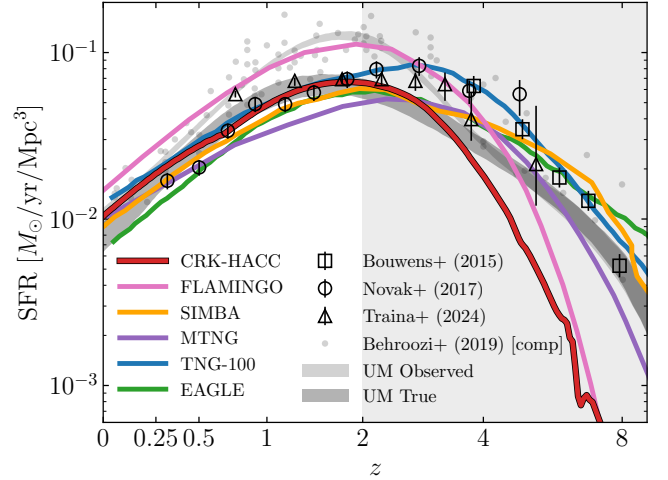


Figure 6. Cosmic star formation rate density (CSFRD) as a function of redshift. Results from the fiducial CRK-HACC simulation are compared with observational estimates from Bouwens et al. (2015) (UV), Novak et al. (2017) (radio), and Traina et al. (2024) (submillimeter), and with predictions from hydrodynamical simulations (EAGLE; Furlong et al. 2015, Illustris-TNG and MillenniumTNG; Pakmor et al. 2023, SIMBA; Davé et al. 2019, and FLAMINGO; Schaye et al. 2023). Also shown are the results of Behroozi et al. (2019), including their compiled pre-2016 multi-wavelength dataset and empirical UniverseMachine model curves, which distinguish “observed” (bias-affected) and “true” (bias-corrected) CSFRD histories. Over the resolved redshift range $0 \leq z \lesssim 3$, CRK-HACC is consistent with other simulations and closely follows the UniverseMachine “true” prediction as well as recent observations. At higher redshifts, both CRK-HACC and FLAMINGO underpredict the observational estimates and higher-resolution simulations, as expected from the reduced contribution of low-mass halos in coarser-resolution runs. For reference, the region at $z > 2$ is shaded to indicate epochs beyond the redshift range calibrated by the GSMF (see Section 3).

galaxy formation models calibrated to different observational constraints.

In all cases, the stellar mass density reported by the simulations (solid lines) is measured from stars residing in galaxies. This approach mirrors that of observational estimates, which derive stellar mass densities from galaxy stellar mass functions and therefore exclude intra-halo light (IHL) contributions. Following our analysis pipeline (Section 2.9), CRK-HACC measures galaxy properties within fixed 50 pkpc apertures, as does COLIBRE. The EAGLE results adopt 30 pkpc apertures, while SIMBA reports stellar masses including all bound star particles. For reference, the dashed CRK-HACC curve in Figure 7 includes all stars in the simulation (both galaxy and diffuse IHL components) and serves as an upper bound on the stellar mass locked in galaxies.

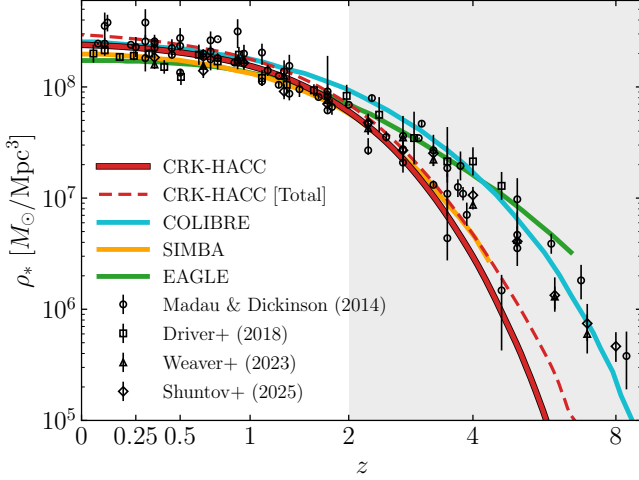


Figure 7. Cosmic stellar mass density (CSMD) as a function of redshift. Results from the fiducial CRK-HACC simulation are compared with observational estimates from [Madau & Dickinson \(2014\)](#), [Driver et al. \(2018\)](#), [Weaver et al. \(2023\)](#), and [Shuntov et al. \(2025\)](#), and with predictions from the COLIBRE ([Chaikin et al. 2025b](#)), EAGLE ([Furlong et al. 2015](#)), and SIMBA ([Thomas et al. 2019](#)) simulations. The solid CRK-HACC curve shows the stellar mass density from stars residing in galaxies, while the dashed curve labeled [Total] includes all stars in the simulation, capturing both galaxy and intra-halo light contributions. Comparisons among simulations are based on galaxy-only measurements, adopting fixed apertures of 50 pkpc for CRK-HACC and COLIBRE, 30 pkpc for EAGLE, and all bound stars for SIMBA. The CRK-HACC results closely match the observed stellar mass density over the resolved redshift range ($0 \leq z \lesssim 3$), consistent with the level of agreement seen for the CSFRD in Figure 6, beyond which resolution effects begin to suppress early stellar mass formation. For reference, the region at $z > 2$ is shaded to indicate epochs beyond the redshift range calibrated by the GSMF (see Section 3).

The CRK-HACC results demonstrate the expected buildup of stellar mass across cosmic time. At high redshift ($z \gtrsim 3$), the predicted stellar mass density gradually falls below the observational estimates, consistent with the suppressed CSFRD at early times shown in Figure 6. From $z \sim 2$ –3 to the present, CRK-HACC follows the overall spread of observational datasets, remaining within their combined scatter across this interval. As emphasized by [Behroozi et al. \(2019\)](#), systematic uncertainties in stellar mass functions are notably smaller than those affecting SFR indicators and diminish further toward low redshift. The close agreement between CRK-HACC and the observed stellar mass density over the resolved redshift range is therefore reassuring.

Relative to other hydrodynamical simulations, CRK-HACC closely follows the shape and normalization of COLIBRE at low redshift ($z < 1$), remaining systemati-

cally above the EAGLE and SIMBA predictions. Toward intermediate epochs ($1 \lesssim z \lesssim 2$), the CRK-HACC stellar mass density falls slightly below COLIBRE, aligning more closely with SIMBA. At higher redshift, it declines more steeply, crossing below EAGLE and later SIMBA, reflecting the increasing sensitivity of early stellar mass assembly to numerical resolution and feedback efficiency.

4.3. Galaxy Sizes

With the global buildup of stellar mass established, we next examine the internal structure of galaxies beginning with morphology. A central structural property of galaxies is their size, commonly quantified by the radius enclosing half the stellar mass, $R_{1/2}$. In simulations, galaxy sizes are particularly sensitive to numerical resolution and the adopted feedback prescriptions, which together shape the morphology and spatial distribution of stars.

Consequently, large-volume simulations with gravitational force resolutions approaching galactic scales (\sim kpc), such as CRK-HACC, MillenniumTNG, and FLAMINGO (see Table 3), are not expected to reproduce precise size–mass relations but can still provide meaningful qualitative benchmarks. Reported sizes are further influenced by measurement details such as projection effects and aperture cutoffs. In Figure 8, we present a set of CRK-HACC size measurements for comparison, spanning both 2D projected and 3D configurations.

The CRK-HACC curves illustrate three representative size definitions that together bracket the range of predicted galaxy radii. Our default measurement (solid line) adopts a 2D half-mass radius within a fixed 50 pkpc aperture, where stellar mass is summed over the projected stellar distribution. This aperture choice causes the measured radii to saturate at high stellar masses. Expanding the projected region to 100 pkpc leaves the low-mass sizes unchanged but increases radii at the massive end, where extended stellar envelopes become significant. Finally, we include a 3D half-mass radius computed from all DBSCAN-assigned stars (see Section 2.9). This definition does not saturate at high mass and, as expected, yields systematically larger radii than the 2D measurements because projection compresses stars along the line of sight (see, e.g., Appendix C of [Furlong et al. 2016](#)).

To contextualize these measurements, we compare them to recent observational datasets. [Behroozi et al. \(2022\)](#) provide an empirical fit (their Eq. 13) to SDSS measurements of galaxy sizes, converted to three-dimensional half-mass radii, which we show as a continuous curve. [Hardwick et al. \(2022\)](#) present direct measurements of projected stellar half-mass radii, de-

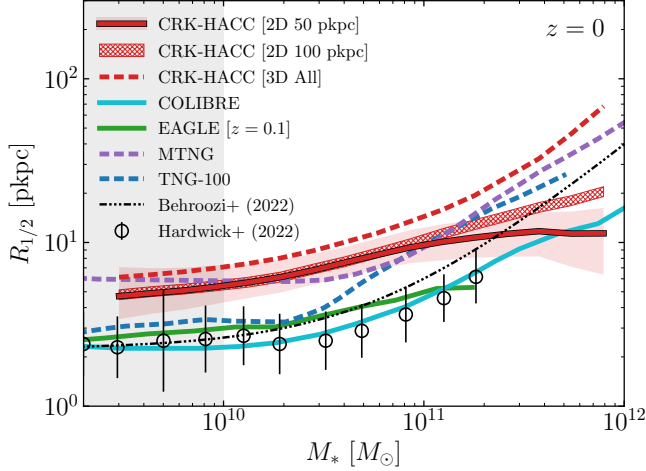


Figure 8. Stellar half-mass radius as a function of stellar mass at $z = 0$. The CRK-HACC results are shown for three size definitions: projected radii within 50 pkpc (solid), projected radii within 100 pkpc (hatched), and three-dimensional radii from all DBSCAN-assigned stars (dashed). Lines indicate median relations, with the red shaded region denoting the 16th–84th percentile range for the default measurement. Gray shaded regions mark the regime where the CRK-HACC results are resolution limited. Observational constraints include the 3D empirical fit to SDSS ($z < 0.2$) data from Behroozi et al. (2022) and the 2D projected measurements from Hardwick et al. (2022) for nearby xGASS galaxies ($z < 0.05$). Comparison simulation results for 2D measurements (solid lines) are drawn from EAGLE (Schaye et al. 2015; at $z = 0.1$) and COLIBRE (Schaye et al. 2025), while 3D results (dashed) are from Illustris-TNG and MillenniumTNG (Pakmor et al. 2023). 2D observations and predictions are systematically lower than 3D owing to projection and aperture effects. High-resolution simulations (EAGLE, COLIBRE, Illustris-TNG) reproduce the observed size–mass relation, while lower-resolution runs (MillenniumTNG, CRK-HACC) yield larger radii at low masses but converge toward the others at high masses.

rived from stellar mass surface density profiles in deep imaging of xGASS galaxies, which we include as discrete points. Together, these datasets provide both a 3D empirical relation and its direct 2D observational counterpart, spanning a broad range of stellar masses at $z = 0$. As shown in Figure 8, the datasets are mutually consistent, with the Hardwick et al. (2022) points lying systematically lower, as expected from projection effects.

For theoretical context, we also compare with predictions from several hydrodynamical simulations, which span different mass resolutions. The EAGLE (Schaye et al. 2015) and COLIBRE (Schaye et al. 2025) results are reported as projected half-mass radii within fixed apertures and were directly calibrated against the observed size–mass relation. We also include results from

Illustris-TNG and MillenniumTNG, taken from Pakmor et al. (2023), which present intrinsic three-dimensional half-mass radii measured from all stars bound to each subhalo. Owing to these differing measurement conventions, the comparison to CRK-HACC should be regarded as qualitative rather than quantitative.

As shown in Figure 8, the high-resolution simulations reproduce the observed size–mass relation well. The EAGLE and COLIBRE curves closely follow the Hardwick et al. (2022) data points, as expected given that these simulations report projected half-mass radii and were calibrated to match the observed relation. The three-dimensional Illustris-TNG measurements are broadly consistent with the Behroozi et al. (2022) fit, though they lie slightly above it at the highest stellar masses.

The lower-resolution MillenniumTNG curve lies systematically above both the observational constraints and the higher-resolution simulations. This offset reflects the impact of finite force softening and mass resolution, which broaden stellar distributions and inflate measured radii. At high stellar masses, however, MillenniumTNG converges toward the Illustris-TNG relation once galaxies become sufficiently resolved. A similar behavior is seen in other large-volume runs, such as FLAMINGO, where both star-forming and quenched galaxies exhibit systematically larger radii at lower masses, as shown in Figure 14 of Schaye et al. (2023).

Our CRK-HACC results follow the same overall trend. At low stellar masses, the predicted radii are consistent with MillenniumTNG, as expected given our coarser resolution. The three-dimensional half-mass definition provides the closest analog to the MillenniumTNG measurement, though it may be slightly inflated because DBSCAN-defined galaxies can include additional intra-halo light. At high masses, the 2D CRK-HACC measurements begin to approach the smaller radii reported by COLIBRE, while the 3D definition remains consistent with the Illustris-TNG and MillenniumTNG curves. Together, these comparisons show how measurement choices bracket the predicted range of galaxy sizes and emphasize that CRK-HACC results are resolution-limited but aligned with expectations from other large-volume simulations.

4.4. Galaxy Star Formation Activity and Quenching

Accurately reproducing galactic stellar evolution poses a challenging constraint on astrophysical subgrid models. Although the GSMF was calibrated to match the observed stellar mass distribution over $0 < z < 2$, this constraint alone does not determine the star-formation activity or quenching efficiency of the galaxy population. To assess these processes in CRK-HACC, we

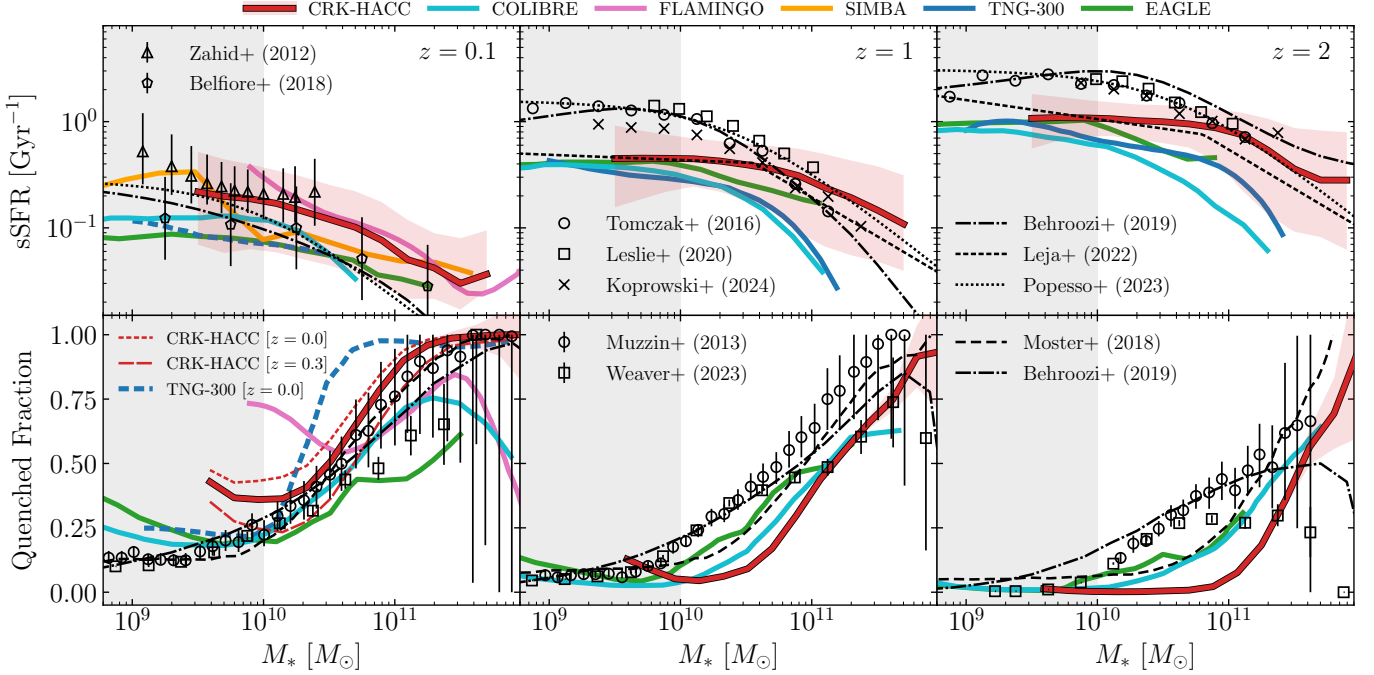


Figure 9. Top: Median sSFR as a function of stellar mass for CRK-HACC galaxies at $z = 0.1$, $z = 1$, and $z = 2$ (red shaded 16th–84th percentile range), compared with simulation results from Illustris-TNG (sSFR: [Donnari et al. 2019](#); quenched: [Donnari et al. 2021](#)), EAGLE ([Furlong et al. 2015](#)), COLIBRE ([Chaikin et al. 2025b](#)), SIMBA ([Davé et al. 2019](#)), and FLAMINGO ([Schaye et al. 2023](#)). Observational datasets include optical spectroscopy ([Zahid et al. 2012](#); [Belfiore et al. 2018](#)), NIR photometry ([Tomczak et al. 2016](#)), radio stacking ([Leslie et al. 2020](#)), and FIR stacking ([Koprowski et al. 2024](#)), as well as empirical ([Behroozi et al. 2019](#); [Popesso et al. 2023](#)) and SED-based ([Leja et al. 2022](#)) fits. Data points correspond to [Zahid et al. \(2012\)](#) ($z < 0.1$), [Belfiore et al. \(2018\)](#) ($z \sim 0.028$), [Tomczak et al. \(2016\)](#) ($0.75 < z < 1$; $1.5 < z < 2$), [Leslie et al. \(2020\)](#) ($0.8 < z < 1.1$; $1.5 < z < 2.0$), and [Koprowski et al. \(2024\)](#) ($0.75 \leq z < 1.0$; $1.6 \leq z < 2.2$). **Bottom:** Quenched fractions for the full galaxy population in CRK-HACC compared to the same set of simulations, with observational constraints from [Muzzin et al. \(2013\)](#) ($0.2 \leq z < 0.5$; $0.5 \leq z < 1$; $1.5 \leq z < 2$) and [Weaver et al. \(2023\)](#) ($0.2 < z \leq 0.5$; $0.8 < z \leq 1.1$; $1.5 < z \leq 2$) and semi-empirical predictions from EMERGE ([Moster et al. 2018](#)) ($0 < z \leq 0.5$; $0.5 < z \leq 1$; $1.5 < z \leq 2$) and UniverseMachine ([Behroozi et al. 2019](#)). Additional $z=0.0$ and $z=0.3$ CRK-HACC curves are shown in the $z=0.1$ panel to illustrate rapid low- z evolution. In all panels, gray shaded regions mark the regime below the CRK-HACC mass resolution limit. Overall, CRK-HACC follows the trends of other simulations, showing low- z sSFR agreement with observations but systematic high- z offsets, except for the lower SFRs inferred by [Leja et al. \(2022\)](#). The resolved high-mass CRK-HACC prediction shows good agreement with data. Quenched fractions are similar, with residual differences primarily set by the resolution of each simulation — limited SFR sampling drives the low-mass upturn, while unresolved faint systems suppress early growth and delay quenching at high redshift (see text).

examine the specific star formation rate (sSFR) and the passive fraction of galaxies as a function of redshift.

Throughout this analysis, we distinguish star-forming (main-sequence) galaxies from passive systems using the commonly adopted threshold $\text{sSFR} > 0.2 t_H(z)^{-1}$, where $t_H(z)$ is the Hubble time at redshift z (e.g., [Gallazzi et al. 2014](#); [Pacifci et al. 2016](#)). We compare our results with corresponding measurements from COLIBRE ([Chaikin et al. 2025b](#)), Illustris-TNG ([Donnari et al. 2019](#), [2021](#)), EAGLE ([Furlong et al. 2015](#)), SIMBA ([Davé et al. 2019](#)), and FLAMINGO ([Schaye et al. 2023](#)). Measurement and aperture definitions, as well as the adopted main-sequence thresholds, differ among simulations; the comparisons shown here are therefore qualitative.

4.4.1. Specific Star Formation Rate

The specific star formation rate is defined as $\text{sSFR} \equiv \text{SFR}/M_*$, quantifying the instantaneous growth of stellar mass relative to the existing stellar population. The top panel of Figure 9 presents the median sSFR– M_* relation for CRK-HACC galaxies at $z = 0.1$, $z = 1$, and $z = 2$, with red shaded regions showing the 16–84th percentile range.

Alongside the comparison simulation curves, we include observational datasets spanning optical spectroscopy ([Zahid et al. 2012](#); [Belfiore et al. 2018](#)), near-infrared photometry ([Tomczak et al. 2016](#)), radio stacking ([Leslie et al. 2020](#)), and far-infrared stacking ([Koprowski et al. 2024](#)). As broader references across all redshifts, we overlay the empirical relation from

Behroozi et al. (2019) and the harmonized fit of modern SFR observations from Popesso et al. (2023). Lastly, we show the analysis of Leja et al. (2022), which infers systematically lower SFRs (by ~ 0.2 – 0.5 dex) from panchromatic SED modeling that accounts for dust heating by older stellar populations.

At $z = 0.1$, the selected simulation results cluster together and are in broad agreement with the mutually consistent reference relations from Behroozi et al. (2019) and Popesso et al. (2023). The CRK-HACC measurement lies within this grouping, toward the upper envelope alongside FLAMINGO. All curves fall between the optical spectroscopic constraints of Zahid et al. (2012) and Belfiore et al. (2018), which bracket the local normalization of the star-forming main sequence.

At higher redshifts ($z = 1$ and $z = 2$), the simulations remain closely grouped but diverge systematically from the bulk of observational measurements. While surveys and empirical fits indicate higher sSFR normalizations, the simulations are uniformly lower, reflecting a long-standing tension between models and observations (e.g., Daddi et al. 2007; Somerville & Davé 2015). This offset is often attributed to differences in how SFRs are defined, being measured directly in simulations but inferred observationally through modeling assumptions.

An important exception is the analysis of Leja et al. (2022), which, as noted above, infers lower SFRs and agrees more closely with the simulation trends. In this regime, CRK-HACC again follows the upper edge of the simulation grouping, matching particularly well with the Leja et al. (2022) relation. Notably, this agreement extends to the high-mass end, where all observational datasets converge. A similar pattern appears in the EAGLE results at $z = 1$ and persists in the CRK-HACC measurements through $z = 2$. We find a corresponding agreement in the quenched fraction at high masses, as discussed below.

4.4.2. Quenched Fraction

A complementary measurement to the sSFR is the evolution of the passive fraction of galaxies over cosmic time, tracing the buildup of the quenched population and the efficiency with which galaxies transition out of the star-forming sequence. The lower panels of Figure 9 show the CRK-HACC quenched fraction as a function of stellar mass at $z = 0.1$, $z = 1$, and $z = 2$. We include the simulation results from Illustris-TNG, FLAMINGO, EAGLE, and COLIBRE where available.

For observational context, we include quenched fractions derived from near-infrared-selected samples (Muzzin et al. 2013) and from wide-area multiwavelength photometric surveys (Weaver et al. 2023). We

also show semi-empirical predictions from EMERGE (Moster et al. 2018) and UniverseMachine (Behroozi et al. 2019), which connect galaxy growth to dark matter halo assembly. We again note that sSFR thresholds, SFR timescales, and apertures differ among simulations, and that many observational constraints are both redshift-binned and inference-dependent (e.g., SED modeling and dust corrections). Consequently, cross-survey and cross-simulation comparisons should be interpreted qualitatively.

At $z = 0.1$, the quenched fractions from the selected simulations form a relatively tight grouping, with CRK-HACC lying near the upper edge of the band. The supplemental $z = 0$ and $z = 0.3$ curves illustrate the rapid recent growth of the passive population in CRK-HACC, bracketing the observational estimates from Muzzin et al. (2013) and Moster et al. (2018), and lying at a slightly higher normalization than Behroozi et al. (2019) and Weaver et al. (2023).

A notable feature of the CRK-HACC relation is the upturn in the quenched fraction below the mass resolution limit at $M_* \lesssim 10^{10} M_\odot$. Similar behavior is seen across all simulations at mass scales set by their respective resolutions, where galaxies with sparsely sampled star-forming gas can artificially appear quenched. The upturn occurs at a higher mass for the lower-resolution FLAMINGO run and at smaller masses for the higher-resolution simulations Illustris-TNG, EAGLE, and COLIBRE, as expected.

At earlier redshifts, the observed quenched fractions are systematically higher than those predicted by the simulations, except for the semi-empirical results from Moster et al. (2018), which fall closer to the data. Within the simulation set, CRK-HACC consistently lies at the low end, reflecting the elevated sSFRs seen in the top panels. This combination of enhanced star-formation activity and reduced quenching aligns with the deficit in the CSFRD at high redshift (see Figure 6), where unresolved low-mass galaxies suppress early growth and shift stellar assembly to later times. As a result, CRK-HACC maintains a larger star-forming population at $z = 1$ – 2 , delaying quenching relative to observations and higher-resolution simulations. At the well-sampled high-mass end, however, the CRK-HACC relation converges toward the observational estimates, consistent with the agreement seen in the sSFR relations.

We next examine the quenched fraction separately for centrals and satellites, two populations expected to follow distinct quenching pathways. Satellites are typically more quenched than centrals at fixed stellar mass because infall halts fresh gas accretion and exposes galax-

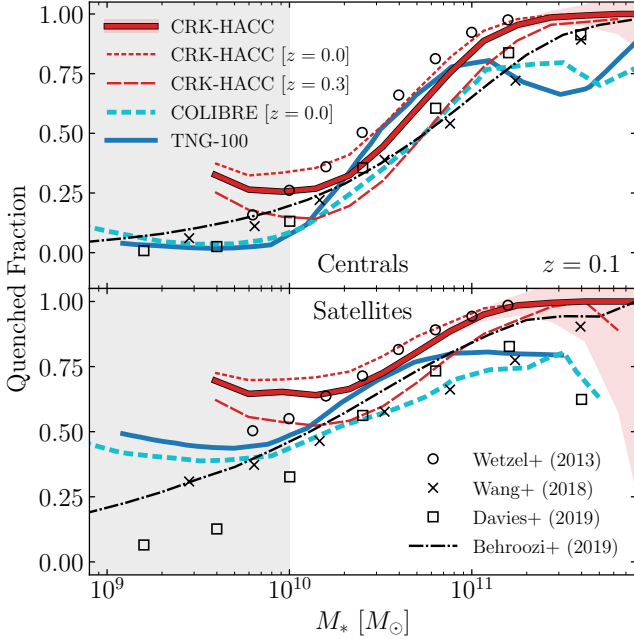


Figure 10. Quenched fractions for central (top) and satellite (bottom) galaxies at $z = 0.1$ in CRK-HACC, with additional $z = 0.0$ and $z = 0.3$ curves shown to illustrate rapid late-time evolution. Red shaded regions indicating Poisson uncertainties are shown for the $z = 0.1$ curve. Gray shaded regions mark the regime below the CRK-HACC mass resolution limit. Results are compared with Illustris-TNG (Donnari et al. 2021) and COLIBRE (Chaikin et al. 2025b; measured at $z = 0$), as well as local ($z < 0.2$) observational estimates from SDSS (Wetzel et al. 2013; Wang et al. 2018) and GAMA (Davies et al. 2019). Semi-empirical predictions from UniverseMachine at $z = 0.1$ are also shown. Observational surveys primarily probe group and cluster environments, whereas the simulations represent the full satellite population. CRK-HACC lies between the other simulations for centrals and near the upper edge for satellites, in reasonable agreement with the spread of observational estimates. Each simulation exhibits a resolution-dependent low-mass upturn in the quenched fraction, consistent with the trends shown in Figure 9.

ies to environmental processes (such as ram-pressure and tidal stripping) that accelerate gas depletion. Figure 10 shows the CRK-HACC passive fractions for both populations at $z = 0.1$, compared with COLIBRE (measured at $z = 0$) and Illustris-TNG, as well as observational estimates from SDSS (Wetzel et al. 2013; Wang et al. 2018) and GAMA (Davies et al. 2019). We also include empirical predictions from UniverseMachine (Behroozi et al. 2019).

For centrals, the predictions from Illustris-TNG, COLIBRE, and CRK-HACC all fall within the envelope of the observational datasets, with the CRK-HACC curve lying near the middle for intermediate and high stellar masses. Specifically, CRK-HACC lies between the esti-

mates of Wetzel et al. (2013) and Davies et al. (2019), and above the lower normalizations reported by Wang et al. (2018) and UniverseMachine. At lower masses, we again see the upturn noted in Figure 9, which reflects numerical resolution limits. The supplemental $z = 0.0$ and $z = 0.3$ curves further highlight the rapid recent evolution of the central passive population in CRK-HACC, consistent with the trends already evident in the full galaxy sample.

For satellites, shown in the lower panel of Figure 10, the overall interpretation is similar, though in this case the UniverseMachine predictions track the CRK-HACC results more closely. The observational constraints show a wider spread, partly because the relevant surveys target satellites in specific group or cluster environments rather than the full satellite population represented in simulations. Even so, CRK-HACC lies near the upper edge of the simulation set, predicting a more quenched satellite population at low redshift.

4.5. Stellar Mass–Halo Mass Relation

The stellar mass–halo mass (SMHM) relation measures the fractional stellar content of central galaxies as a function of host halo mass. Empirically, it peaks near Milky Way–mass halos ($M_{200c} \sim 10^{12} M_{\odot}$), where galaxy formation is most efficient, and declines toward both lower and higher halo masses. In simulations, the SMHM relation traces how star formation and feedback prescriptions regulate galactic growth within the context of hierarchical halo assembly.

Figure 11 compares the CRK-HACC SMHM relation for central galaxies with three observational baselines. The Moster et al. (2013) curve represents a classical abundance-matching result that links the observed stellar and halo mass functions. The median Behroozi et al. (2019) (UniverseMachine) relation employs forward modeling to jointly reproduce multiple galaxy statistics and provides a posterior distribution for the intrinsic scatter. At high halo masses, the Kravtsov et al. (2018) relation accounts for extended stellar envelopes and intracluster light (ICL), increasing the inferred stellar fractions by approximately 0.2–0.3 dex at $M_{200c} \gtrsim 10^{13.5} M_{\odot}$. Together, these three curves span the roughly factor-of-two range among current observational estimates, with ICL treatment remaining the dominant systematic uncertainty at the high-mass end.

The fiducial CRK-HACC SMHM measurement in Figure 11 adopts a 50 pkpc aperture and includes only central galaxies, defined as the most stellar-massive system within each halo. We report the relation for halos with $M_{200c} \gtrsim 10^{11} M_{\odot}$, corresponding to the smallest galaxies reliably resolved in the simulation. For compar-

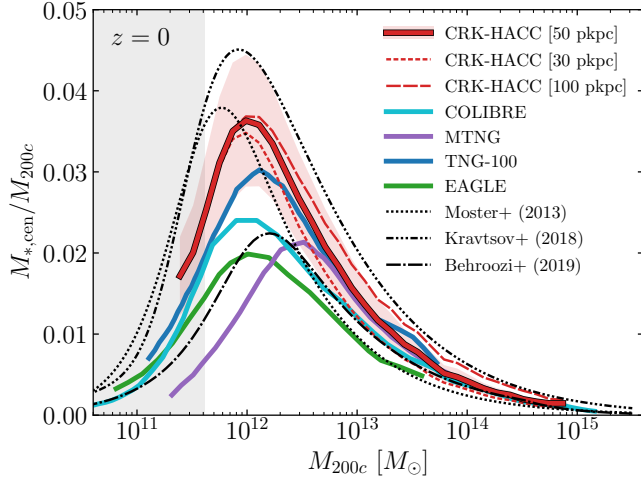


Figure 11. Stellar mass–halo mass (SMHM) relation for central galaxies at $z = 0$. The median CRK-HACC prediction is shown for fixed physical apertures of 30, 50 (default), and 100 pkpc, with the red shaded region indicating the 16th–84th percentile range for the default choice. Observational constraints from Moster et al. (2013), Behroozi et al. (2019), and Kravtsov et al. (2018) are shown, spanning a mutual spread of ~ 0.3 dex across halo masses. Results from the EAGLE (Schaye et al. 2015), Illustris-TNG (Pakmor et al. 2023), MillenniumTNG (Pakmor et al. 2023), and COLIBRE (Schaye et al. 2025) simulations are included for comparison, each shown over its reported mass range. Gray shaded regions mark the regime below the CRK-HACC mass resolution limit ($M_{*,\text{cen}} \lesssim 10^{10} M_{\odot}$). The fiducial 50 pkpc CRK-HACC measurement lies within the observational envelope with a normalization similar to Moster et al. (2013), and is consistent with other simulations and observations at higher masses. The 30 pkpc and 100 pkpc curves illustrate the aperture dependence of stellar mass, with the latter converging toward the Kravtsov et al. (2018) prediction, consistent with capturing intra-halo light contributions at group and cluster scales.

ison, we also show results from the EAGLE (Schaye et al. 2015), Illustris-TNG (Pakmor et al. 2023), MillenniumTNG (Pakmor et al. 2023), and COLIBRE (Schaye et al. 2025) simulations, which extend to lower halo masses owing to their higher mass resolution.

The CRK-HACC relation lies well within the observational envelope and most closely follows the shape and normalization of the Moster et al. (2013) relation, though it is slightly shifted toward higher halo masses. Relative to other simulations, the halo mass of peak efficiency ($M_{200c} \sim 10^{12} M_{\odot}$) lies near the center of the published range, while the corresponding stellar fraction is somewhat higher in CRK-HACC at this mass scale. At larger halo masses, all simulations and most observational inferences converge, with the Kravtsov et al. (2018) relation remaining elevated due to its inclusion of ICL at group and cluster scales.

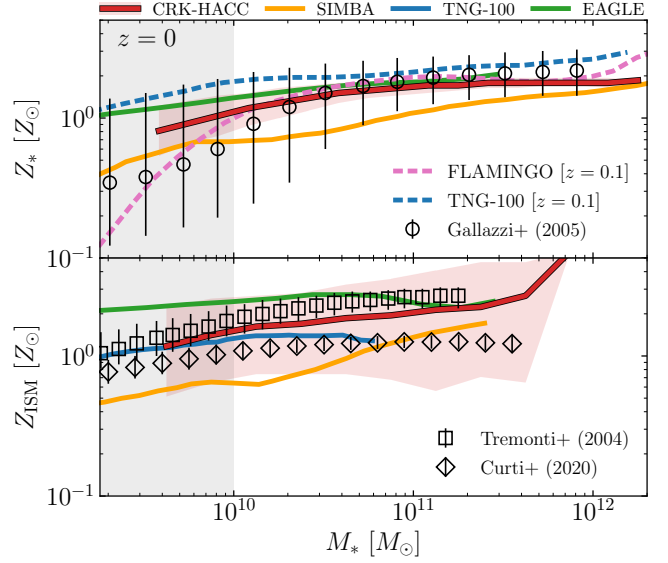


Figure 12. Galaxy mass–metallicity relations (MZR) from the fiducial CRK-HACC simulation (red shaded 16th–84th percentile range) compared to observational measurements and predictions from the EAGLE (Schaye et al. 2015), SIMBA (Davé et al. 2019), Illustris-TNG (stellar: Nelson et al. 2017; ISM: Torrey et al. 2019), and FLAMINGO (Schaye et al. 2023) simulations. All metallicities are expressed in solar units with $Z_{\odot} = 0.0129$. Gray shaded regions mark the regime below the CRK-HACC mass-resolution limit. **Top:** Stellar metallicity relation, with local ($z < 0.22$) SDSS-based estimates from Gallazzi et al. (2005). **Bottom:** ISM metallicity relation, compared to local ($z \sim 0.1$) SDSS strong-line results from Tremonti et al. (2004) and T_e -based calibrations from Curti et al. (2020). The CRK-HACC results reproduce observed stellar metallicities across the resolved mass range and predict ISM abundances bracketed by observational systematics.

To illustrate the impact of aperture choice, Figure 11 also shows CRK-HACC measurements using 30 pkpc and 100 pkpc apertures. The smaller aperture is consistent with all other simulations shown here except COLIBRE (which uses our default 50 pkpc aperture) and yields a lower inferred stellar fraction by excluding extended stellar light. The larger aperture includes more diffuse stellar components and shifts the relation upward, converging toward the Kravtsov et al. (2018) curve at the highest halo masses where ICL contributions become significant. For large-volume simulations, this underscores the importance of matching the level of intra-halo light included in specific observational analyses when comparing stellar mass fractions in groups and clusters.

4.6. Stellar Mass–Metallicity Relations

The galaxy mass–metallicity relation (MZR) provides an important constraint on galaxy evolution models, linking stellar mass growth to the efficiency of metal

production and retention. Two complementary forms of the MZR are commonly considered: the stellar metallicity relation, which reflects the integrated enrichment history imprinted on long-lived stars, and the ISM metallicity relation, which captures the present-day abundance of heavy elements in star-forming gas. Together, these observables probe both the cumulative and instantaneous regulation of baryons and metals in galaxies.

The top panel of Figure 12 shows the stellar mass–metallicity relation from the fiducial CRK-HACC simulation compared with SDSS-based measurements from Gallazzi et al. (2005) and predictions from other hydrodynamical simulations. The observational relation indicates that galaxies with $M_* \gtrsim 10^9 M_\odot$ are already substantially enriched, with only a weak residual dependence on stellar mass.

CRK-HACC reproduces the observed stellar metallicities well across the resolved mass range. This agreement supports the parameter choices in our metallicity model, where star-forming gas is initialized with a minimum metallicity floor of $Z_{\text{ISM}, \text{min}} = 0.25 Z_\odot$ (Section 2.4.2), and galactic winds are assumed to be metal-poor ($\gamma_w = 0$; Section 2.5.3) at the coarse resolution. Together, these settings seed unresolved early galaxies with the enrichment they would have produced and ensure that those metals remain in the ISM rather than being expelled in outflows.²⁰

Relative to other simulations, CRK-HACC most closely follows the predictions of EAGLE (Schaye et al. 2015), despite operating at a much lower mass resolution. The Illustris-TNG relation (Nelson et al. 2017) lies slightly above both CRK-HACC and the observational mean but remains consistent within the scatter, whereas SIMBA (Davé et al. 2019) predicts a shallower relation with systematically lower stellar metallicities. FLAMINGO (Schaye et al. 2023) shows a spurious ramp at low masses caused by resolution effects, but converges toward the observational relation for $M_* \gtrsim 10^{10} M_\odot$.

The comparison with FLAMINGO is particularly informative, as both simulations operate at similar resolution. FLAMINGO models metal production self-consistently, without imposing an artificial metallicity floor, which leads to a delayed enrichment ramp-up until galaxies are sufficiently resolved. In contrast, CRK-HACC enforces early enrichment through a resolution-dependent initialization, allowing the stellar metallicity

relation to match observations across the reported mass range.

We now turn to the metallicity relation of the star-forming ISM, shown in the bottom panel of Figure 12. The canonical SDSS analysis of Tremonti et al. (2004) inferred gas-phase abundances from strong emission-line ratios using photoionization models, yielding relatively high metallicities at fixed stellar mass. In contrast, calibrations tied to direct T_e -based abundance measurements (e.g., Curti et al. 2020) produce a lower normalization by about 0.2–0.3 dex. The T_e method is generally regarded as the more reliable standard, as it avoids the model dependencies inherent to strong-line techniques, though systematic uncertainties remain. Together, these two determinations are representative of the range spanned by current observations of the ISM MZR.

CRK-HACC predicts ISM metallicities that fall between the two observational measurements, with substantial scatter such that both the Tremonti et al. (2004) and Curti et al. (2020) relations lie within its spread. The median trend most closely resembles that of Illustris-TNG (ISM data from Torrey et al. 2019), whose predictions align well with the T_e -based calibration of Curti et al. (2020). In contrast, EAGLE yields systematically higher metallicities consistent with the Tremonti et al. (2004) relation, while SIMBA produces lower values across the full mass range. Overall, CRK-HACC predicts an ISM MZR intermediate between the two observational calibrations and bracketed by their systematic uncertainties.

We note that all results in Figure 12 have been renormalized to our adopted solar abundance of $Z_\odot = 0.0129$ (see Section 2.3.1) for consistency. In addition, the simulations differ in how metallicities are defined and averaged (e.g., mass-weighted, as used here, versus SFR- or light-weighted), so comparisons should be regarded as qualitative.

4.7. Black Hole Mass–Stellar Mass Relation

The black hole–stellar mass (BHSM) relation characterizes the coevolution of galaxies and their central supermassive black holes. Observationally, black hole masses correlate with bulge stellar mass and velocity dispersion, though both the slope and scatter depend strongly on galaxy morphology. In cosmological simulations, black holes cannot be resolved directly and are instead modeled through subgrid prescriptions that capture their growth and feedback. As a result, relations such as the BHSM are not predicted from first principles but serve as informative benchmarks for assessing whether these coarse-grained models reproduce the inte-

²⁰ At higher resolution, this choice becomes less restrictive, as metal loading factors near the conventional value of $\gamma_w = 0.4$ (as used in Illustris-TNG) can be adopted in our model without oversuppressing enrichment, and the imposed $Z_{\text{ISM}, \text{min}}$ correspondingly decreases as earlier enrichment is directly resolved.

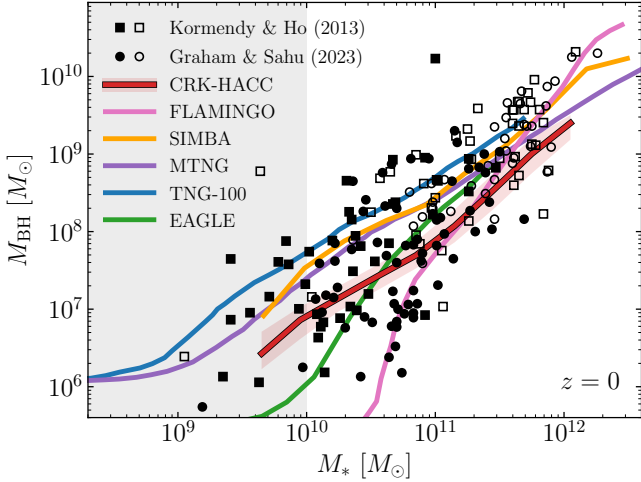


Figure 13. Black hole–stellar mass relation at $z = 0$ from the fiducial CRK-HACC simulation, with the red shaded region denoting the 16th–84th percentile range. Gray shaded regions mark the regime below the CRK-HACC mass resolution limit. Results are compared to hydrodynamical models including EAGLE (Schaye et al. 2015), Illustris-TNG (Pakmor et al. 2023), MillenniumTNG (Pakmor et al. 2023), FLAMINGO (Schaye et al. 2023), and SIMBA (Thomas et al. 2019), as well as local ($z \lesssim 0.05$) observational compilations (Kormendy & Ho 2013; Graham & Sahu 2023). In the observational data, filled and open markers denote disk and elliptical galaxies, respectively. The Kormendy & Ho (2013) points are reported in terms of bulge masses (M_{bulge}). The CRK-HACC relation exhibits a slope consistent with Illustris-TNG, MillenniumTNG, and SIMBA, and lies within the broad observational scatter.

grated buildup of black hole mass and provide a physically consistent feedback energy budget within their host galaxies.

Figure 13 compares the BHSM relation from the fiducial CRK-HACC simulation with predictions from other hydrodynamical models, including EAGLE (Schaye et al. 2015), Illustris-TNG (Pakmor et al. 2023), MillenniumTNG (Pakmor et al. 2023), FLAMINGO (Schaye et al. 2023), and SIMBA (Thomas et al. 2019). Local observational compilations from Kormendy & Ho (2013) and Graham & Sahu (2023) are also shown. The Kormendy & Ho (2013) dataset reports bulge stellar masses (M_{bulge}), while the Graham & Sahu (2023) sample provides total galaxy stellar masses ($M_{*, \text{gal}}$). Filled and open symbols denote disk and elliptical galaxies, respectively.

The implementation of AGN feedback in CRK-HACC closely follows that of Illustris-TNG (Weinberger et al. 2016), adopting identical values for the radiative accretion and high-accretion mode feedback efficiencies, $\epsilon_r = 0.2$ and $\epsilon_{\text{high}} = 0.1$ (see Section 2.7). Furthermore, in CRK-HACC the calibrated seed mass independently

converged to $M_{\text{seed}} = 8 \times 10^5 h^{-1} M_{\odot}$, the same value adopted in Illustris-TNG.²¹

Given this alignment, it is not surprising that Figure 13 shows similar BHSM slopes for CRK-HACC, Illustris-TNG, and MillenniumTNG. The horizontal offsets among these models arise in part from resolution: in CRK-HACC, black holes are seeded only once host galaxies exceed $M_* \sim 10^9 M_{\odot}$, the effective resolution limit, whereas Illustris-TNG and MillenniumTNG reach lower masses owing to their finer mass resolution. That said, given differences in the black hole evolution model, as well as the broader CRK-HACC subgrid framework and calibration targets, the apparent agreement in normalization may be partly coincidental.

Relative to observations, the scatter in black hole mass at fixed stellar mass is large, reflecting both intrinsic variation and morphological dependence. The predictions from all simulations fall within this broad observational envelope. EAGLE and FLAMINGO seed black holes at low masses and exhibit a more rapid subsequent growth, while Illustris-TNG, MillenniumTNG, SIMBA, and CRK-HACC follow higher, more elliptical-like relations. The CRK-HACC trend lies on the lower edge of the observed scatter, consistent with the adopted efficiency parameters and the coarse simulated mass resolution. Overall, the adopted black hole growth and feedback prescriptions appear to plausibly capture the black hole–galaxy coevolution.

4.8. Halo Gas Fraction

We conclude with a measurement of the halo gas mass fraction, $f_{\text{gas}} = M_{\text{gas}}(r < R_{500c})/M_{500c}$, for halos spanning group to cluster scales, comparing our results with a representative suite of X-ray observations and large-volume hydrodynamic simulations. The gas fraction provides a sensitive probe of feedback strength, as more energetic models drive stronger outflows that deplete halos and lower their total baryonic content.

The predicted CRK-HACC $f_{\text{gas}}-M_{500c}$ relation is shown in Figure 14. Our observational comparison sample includes the *Chandra* study of nearby galaxy groups by Sun et al. (2009), the *XMM-Newton* REXCESS cluster sample analyzed by Pratt et al. (2009), the *ROSAT*-selected *XMM-Newton* group sample of Lovisari et al. (2015), and the joint *XMM-Newton*+*Planck* SZ analy-

²¹ The primary feedback distinction relative to Illustris-TNG is the kinetic implementation, where CRK-HACC employs a constant low-accretion efficiency of $\epsilon_{\text{kin}} = 1.3$ and a jet velocity of $v_{\text{jet}} = 5.1 \text{ km s}^{-1}$, calibrated to reproduce the observed cluster gas density profiles at the fiducial resolution (see Section 3). The kinetic mode contributes only weakly to shaping the BHSM relation compared to the other feedback parameters.

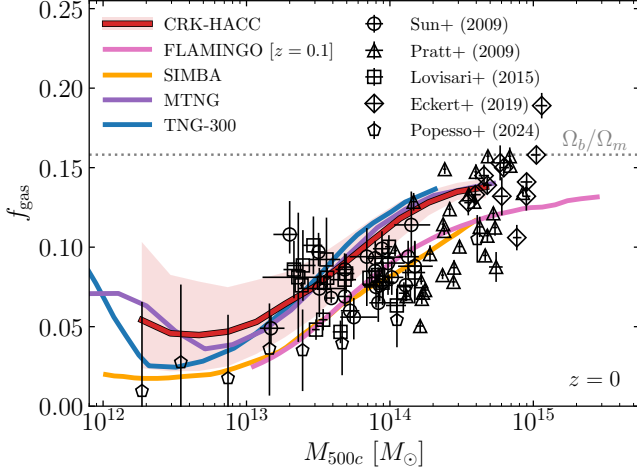


Figure 14. Halo gas fraction as a function of mass at $z=0$ for the calibrated CRK-HACC simulation, with the shaded region indicating the 16th–84th percentile range. Results are compared to local ($z < 0.2$) X-ray measurements from Sun et al. (2009), Pratt et al. (2009), Lovisari et al. (2015), Eckert et al. (2019), and Popesso et al. (2024), where all but Eckert et al. (2019) assume hydrostatic equilibrium without explicit bias correction. For reference, we also include predictions from the Illustris-TNG (Pakmor et al. 2023), MillenniumTNG (Pakmor et al. 2023), SIMBA (Davé et al. 2019), and FLAMINGO (Schaye et al. 2023) simulations. The CRK-HACC calibration closely matches the Illustris-TNG and MillenniumTNG relations while lying above SIMBA and FLAMINGO, which employ more aggressive AGN feedback. This modestly higher normalization reflects the choice to calibrate on observed cluster gas density profiles, prioritizing accurate modeling of the intracluster gas distribution over achieving lower group-scale gas fractions.

sis of massive clusters by Eckert et al. (2019). We also include a recent *eROSITA* measurement from Popesso et al. (2024) based on optically selected groups stacked in X-ray maps, which reports systematically lower gas fractions at fixed mass than earlier X-ray–bright samples. Taken together, these measurements span two orders of magnitude in halo mass but exhibit substantial intrinsic scatter, underscoring the challenge of constraining f_{gas} observationally.

The CRK-HACC results in Figure 14 are in close agreement with the predicted $f_{\text{gas}}-M_{500c}$ relations from the Illustris-TNG and MillenniumTNG simulations, reproducing both the normalization and the characteristic rise of the gas fraction toward the cluster mass scale. By contrast, the predicted gas fractions lie systematically above those of SIMBA and FLAMINGO. This behavior is expected, as SIMBA employs more aggressive AGN jet feedback that efficiently removes gas from group-scale halos, while FLAMINGO explicitly tuned its param-

eters to reproduce observed baryon fractions, resulting in lower f_{gas} by construction.

One of the most important systematics affecting observational measurements is the assumption of hydrostatic equilibrium (HSE) when deriving total masses from X-ray data. Cosmological simulations predict that non-thermal pressure support leads to a ~ 10 –30% underestimate of M_{500c} in typical systems (see Pratt et al. 2019), with smaller biases in dynamically relaxed clusters (e.g., Eckert et al. 2019). As no correction for this bias is applied in Figure 14, the observed f_{gas} values are systematically overestimated, which in turn increases the apparent tension with models that predict higher gas retention.

The close agreement with Illustris-TNG and MillenniumTNG is noteworthy given that the CRK-HACC AGN feedback calibration was performed independently, using cluster gas density profiles as the primary target observable. As discussed in Section 3 and in Ramachandra et al. (2025, in prep.), this calibration strategy was motivated by the goal of producing realistic cluster populations for survey-scale predictions. Attempts to calibrate directly to f_{gas} — as done in e.g., FLAMINGO — were found to strongly alter cluster density profiles under our chosen subgrid implementation. The adopted calibration therefore preserves the observed intracluster gas distribution at the cost of slightly elevated f_{gas} at group scales. Modified AGN feedback models, including redshift-dependent prescriptions, are currently being explored to help reconcile this remaining tension.

Finally, we emphasize that the intrinsic scatter in f_{gas} measurements remains considerably larger in the data than in simulations. Future work employing synthetic X-ray pipelines to estimate M_{gas} and M_{500c} in an observationally consistent manner will be necessary for determining whether these residual offsets primarily reflect measurement biases or limitations of the feedback model itself. For applications where reproducing the mean observed f_{gas} is the primary objective, Ramachandra et al. (2025, in prep.) also provide an alternative calibration with stronger AGN feedback that yields lower gas fractions, suitable for targeted investigations.

5. CONCLUSIONS

Modern precision cosmology efforts have delivered percent-level constraints on the growth of structure through increasingly sophisticated multi-probe surveys, setting new requirements for theoretical accuracy. At this level of precision, baryonic processes significantly affect the matter distribution probed by these surveys, and must therefore be modeled alongside dark matter to ensure reliable predictions of observed signals. More-

over, simulations must encompass full survey-scale volumes in order to capture the statistical reach of current and upcoming experiments. Meeting this challenge remains difficult. The inclusion of baryonic physics substantially increases computational cost, while the underlying astrophysical processes span wide dynamic ranges and require sub-resolution models whose fidelity and consistency are continually being refined.

Fortunately, the necessary components for a new generation of survey-scale modeling efforts are now in place. Exascale computing platforms provide the throughput to include complex baryonic physics at cosmological volumes, while decades of progress in hydrodynamic simulation have yielded physically motivated formulations that can be systematically refined and integrated into modern frameworks. In recent years, we have already witnessed a dramatic increase in the scope and volume of hydrodynamic cosmological simulations — a trend that must continue to meet the demands of upcoming survey analyses.

This study extends the CRK-HACC framework with a physically motivated suite of subgrid models for galaxy formation and feedback, enabling self-consistent treatment of baryonic physics within cosmological volumes comparable to gravity-only simulations. The implementation incorporates radiative cooling, a subgrid multiphase interstellar medium with stochastic star formation, kinetic galactic winds, and two-mode AGN feedback, all coupled to the hydrodynamics and gravity solvers through an operator-split source-term formalism. Designed for GPU acceleration, the framework achieves high performance and scaling on leadership-class supercomputers, providing the computational throughput required for full-physics simulations at exascale volumes and resolutions relevant for survey-scale synthetic-sky generation.

To calibrate the models, we adopt a subgrid parameter set tuned to reproduce the observed galaxy stellar mass function over a survey-relevant redshift range ($0 < z < 2$) as well as the gas-density profiles of massive clusters — an important target for large-volume simulations aimed at studying statistically representative cluster populations. We then carried out an $L_{\text{box}} = 256 h^{-1} \text{ Mpc}$ cosmological simulation using this fiducial model to evaluate the fidelity of the resulting galaxy and halo populations produced by the hydrodynamic framework.

The simulation predictions yield realistic global stellar evolution, reproducing the observed buildup of stellar mass and the decline of star formation across cosmic time. On galactic scales, it produces plausible levels of star-formation activity and quenching, along with chem-

ical enrichment, black-hole growth, and halo gas fractions comparable to those found in other modern simulations. Across these comparisons, there are clear indications of where limited resolution constrains predictive accuracy, particularly in reproducing detailed galactic structures, while the model nevertheless demonstrates the accuracy required to capture the global trends and baryonic couplings that underpin survey-scale observables. In general, balancing model complexity and resolution with simulation scale will remain an ongoing challenge, motivating continued efforts to refine subgrid physics and numerical treatments as computational capabilities improve.

Looking ahead, we will continue to expand the CRK-HACC subgrid framework through increasingly ambitious large-volume hydrodynamic simulations and targeted studies. The framework has already been deployed in an exascale production run, the Frontier-E simulation (Frontiere et al. 2025), demonstrating that hydrodynamic cosmological simulations at trillion-particle scales are now computationally achievable. Building on this foundation, upcoming campaigns will extend both the physical realism and statistical reach of our models, combining flagship large-volume runs with ensembles of hundred-megaparsec simulations that systematically vary cosmological parameters and subgrid prescriptions. Collectively, these efforts will strengthen the predictive power of CRK-HACC and advance its role in supporting next-generation survey science.

ACKNOWLEDGMENTS

We recognize the efforts of past and current HACC team members David Daniel, Patricia Fasel, Hal Finkel, Patricia Larsen, Vitali Morozov, Adrian Pope, Esteban Rangel, and Tom Uram. We thank Damien Lebrun-Grandié, Andrey Prokopenko, and the ArborX team for their critical contributions to the analysis framework. We thank Andy Marszewski for providing FIRE simulation data. We acknowledge the continued collaboration with Mike Owen and Cody Raskin on CRK-SPH solver discussions and development. NF, SH, and KH are also grateful for the insightful discussions and guidance provided during the 2023 summer program “Groups and Clusters of Galaxies at the Crossroad between Astrophysics and Cosmology” at the Aspen Center for Physics.

This research was supported by the Exascale Computing Project (17-SC-20-SC), a collaborative effort of the U.S. DOE Office of Science and NNSA and by the U.S. Department of Energy, Office of Science, Office of Advanced Scientific Computing Research and Office of High

Energy Physics, Scientific Discovery through Advanced Computing (SciDAC) program. Work at Argonne National Laboratory was supported under the U.S. Department of Energy contract DE-AC02-06CH11357. This research used resources of the National Energy Research Scientific Computing Center, a DOE Office of Science User Facility supported by the Office of Science of the U.S. Department of Energy under Contract DE-AC02-05CH11231. This research also used resources of the Argonne Leadership Computing Facility, which is a DOE Office of Science User Facility supported under Contract DE-AC02-06CH11357. Additionally,

this work used resources of the Oak Ridge Leadership Computing Facility, which is a DOE Office of Science User Facility supported under Contract DE-AC05-00OR22725. We gratefully acknowledge use of the Improv cluster in the Laboratory Computing Resource Center at Argonne National Laboratory. CAFG was supported by NSF through grants AST-2108230 and AST-2307327; by NASA through grants 21-ATP21-0036 and 23-ATP23-0008; and by STScI through grant JWST-AR-03252.001-A. Lastly, NF thanks his mother for helping translate his thoughts into something resembling English, for which the other authors wish to express their undying gratitude.

APPENDIX

A. CRK SOLVER MODIFICATIONS

The inclusion of subgrid models necessitates several key modifications to the original reproducing kernel (RK) solver described in FRO23. In particular, coupling complex astrophysical processes introduces deeper timestepping hierarchies, species conversions, and irregular particle topologies resulting from rapid cooling and strong feedback. These effects pose new challenges for numerical stability and solver efficiency. In the following, we briefly summarize the principal solver updates and highlight the most relevant implementation details.

A.1. Reproducing Kernel Relaxation

High-order reproducing kernels are a defining feature of CRKSPH, providing improved accuracy over traditional SPH by exactly reproducing linear fields. The corrected kernel is given by

$$\mathcal{W}_{ij}^R = A_i(1 + \mathbf{B}_i \cdot \mathbf{x}_{ij})W_{ij}(h_i), \quad (\text{A1})$$

where A_i and \mathbf{B}_i are correction coefficients derived from local geometric moments (see Appendix A in FRO17). These coefficients depend solely on the spatial distribution of neighboring particles, making the corrections sensitive to unphysical, high-frequency irregularities in the local point topology. This tradeoff is typical for higher-order methods, where Gibbs-like ringing effects can appear when the local distribution is poorly resolved and is usually handled by artificial viscosity damping. However, when unresolved subgrid sources drive abrupt local changes in momentum, energy, or mass, they can still generate irregular topologies that degrade interpolation accuracy and produce spurious over-expansion or collapse.

To mitigate unphysical forces arising from irregular kernel shapes, we introduce a simple reproducing ker-

nel regularization procedure based on the velocity divergence of each particle. Recall that the RK formulation provides an accurate measurement of the velocity gradient,

$$\nabla \mathbf{v}_i = - \sum_j V_j (\mathbf{v}_i - \mathbf{v}_j) \otimes \nabla \mathcal{W}_{ij}^R, \quad (\text{A2})$$

which is critical for constructing an artificial viscosity limiter that suppresses excessive dissipation in smooth flows (see Section 2.2 in FRO23).

In the context of regularization, the RK correction is relaxed whenever the particle volume is predicted to expand or contract by more than a factor of eight (equivalently, by a factor of two radially). The expected volume change over a timestep Δt can be approximated using the volumetric continuity equation,

$$\frac{dV_i}{dt} = V_i \nabla \cdot \mathbf{v}_i \implies V(\Delta t) = V_i \exp[\nabla \cdot \mathbf{v}_i \Delta t], \quad (\text{A3})$$

where the divergence is computed from the trace of the velocity gradient, $\nabla \cdot \mathbf{v}_i \equiv \text{Tr} \nabla \mathbf{v}_i$. The relaxation condition is enforced by reverting to the standard SPH kernel if

$$\exp[|\nabla \cdot \mathbf{v}_i| \Delta t] > 8 \implies A_i = 1, \mathbf{B}_i = 0, \quad (\text{A4})$$

which prevents unphysical over-expansion or collapse. This condition does not imply that the timestep is too large; rather, it guards against unphysical forces that arise from poorly conditioned RK corrections even when the timestep is properly limited.

While more sophisticated metrics were tested — such as directly examining higher moments of the local point distribution — the simple velocity divergence condition proved both robust and computationally efficient in practice. When triggered, the relaxation is applied

symmetrically: any pairwise force interaction involving a regularized particle is computed without RK corrections for that pair, ensuring consistent momentum exchange without requiring all neighbors to be regularized.

Overall, regularization events are rare because the RK scheme is generally robust for typical gas evolution. Only exceptionally strong subgrid events lead to unrecoverable topologies, and this safeguard prevents pathological configurations from forming. Notably, the stable evolution observed in our subgrid simulations allows us to retain several efficiency strategies from non-radiative runs, such as reusing previously computed correction coefficients for particles that are passive (i.e., not updating forces) during a given timestep. This avoids unnecessary recomputation and yields significant performance gains, especially given the deep timestepping hierarchies required for astrophysical modeling. One caveat is that subgrid species conversions can alter the spatial configuration of active neighbors, requiring any tree leaf that includes transformed particles to recompute its RK correction coefficients to maintain force accuracy. Such leaves are marked for update, minimizing cost by recalculating only where necessary.

A.2. Multi-Species Interaction Domains

The inclusion of astrophysical subgrid processes requires CRK-HACC to consistently handle multiple particle species, each with uniquely defined interaction domains for exchanging mass, energy, and momentum. In what follows, we describe the state properties of each species and how these domains are constructed in practice. Here, we refer to “gas” as the combined set of normal and star-forming gas particles, since both contribute to the hydrodynamic force solver in the usual way (summarized in FRO23). Star-forming gas is distinct only in its ability to spawn wind and star particles and in being subject to thermal evolution governed by an equation of state (Section 2.4). We further refer to subgrid particles as the joint set of wind, star, and black hole particles.

We begin with the modified volume estimate for gas particles. As processes such as stellar enrichment and AGN accretion cause individual particle masses to deviate from the initialized baryon mass, we generalize the gas particle volume definition to

$$V_{i,g}^{-1} = m_{i,g}^{-1} \sum_{j \in g} m_{j,g} W(|\mathbf{x}_{ij}|, h_i), \quad (\text{A5})$$

which reduces to the number density formulation used in FRO23 when all m_i are equal. This expression is equivalent to the standard SPH relation $V_i = m_i / \rho_i^{\text{SPH}}$, where ρ_i^{SPH} is the usual SPH density estimate.

The summation in Eq. (A5) spans only gas particle neighbors, and the resulting volume is used for most hydrodynamic force operators. The only exception is the gas density calculation, which instead uses the modified form given by Eq. (38) and requires a volume that encompasses both gas and wind particles (labeled $V_{i,g \uplus w}$ in that expression). This alternate volume is obtained by expanding the sum in Eq. (A5) to include wind neighbors and is stored separately for use when updating wind and gas densities.

Subgrid particle volumes follow a similar definition: each subgrid species acts as an SPH-like element in the solver but defines its own interaction kernel based exclusively on the surrounding gas. For example, stars redistribute mass to gas through stellar enrichment, black holes inject feedback energy, and wind particles deposit metals into the ISM when launched. All such operations require that the subgrid neighbor sets be defined purely with respect to the physical gas they affect.

Unlike the gas volume estimate, which is mass-weighted, subgrid neighbor definitions are designed to act on a well-defined number of surrounding gas neighbors, emphasizing consistent local coupling rather than mass density alone. Accordingly, it is natural to define the effective volume of each subgrid particle using the SPH number density of local gas neighbors,

$$V_{i,s}^{-1} = \sum_{j \in g \uplus i} W(|\mathbf{x}_{ij}|, h_j), \quad (\text{A6})$$

where the index $s \in \{\star, w, \text{BH}\}$ denotes each subgrid species. The summation explicitly includes the self-interaction, such that $g \uplus i$ denotes the disjoint union of the (non-subgrid) gas neighbors with the subgrid particle itself. This formulation is similar to the original number density formalism in FRO23, except here the SPH sum uses the “scatter” definition (Hernquist & Katz 1989), in which the smoothing length of each gas neighbor, h_j , determines the kernel contribution rather than the subgrid particle extent. This choice ensures that the interaction region of each subgrid element adapts self-consistently to the local gas distribution and allows its domain of influence to be determined entirely by the gas it affects.

The subgrid volume also determines the particle smoothing length, $h_s \propto V_{i,s}^{1/3}$, where all enrichment and feedback interactions are subsequently weighted by the neighboring gas volumes $V_{j,g}$ and kernels $W(|\mathbf{x}_{ij}|, h_s)$ using the “gather” definition (reflected in Eqs. (40), (45) and (58)). To support efficient multi-species neighbor interactions, we sort the particle members within each tree leaf by species type, ensuring that kernels (e.g., for

hydrodynamic forces) operate only on the relevant contiguous subsets and skip unrelated particle types.

All particles use the same [Wendland \(1995\)](#) C^4 kernel of radius h as in [FRO23](#), ensuring consistent force estimates and neighbor sampling across species.²² Each particle type defines its smoothing length based on a target neighbor count appropriate to its physical role. Following previous work, gas particles use $n_{h_g} = 4$ particles per kernel radius, yielding a neighbor count of $N_g = \frac{4\pi}{3} n_{h_g}^3 \approx 268$. Wind particles adopt the same resolution, $n_{h_w} = n_{h_g}$, to contribute consistently to gas density estimates and allow smooth recoupling.

In contrast, stars and black holes use more compact interaction domains with $n_{h_*} = n_{h_{\text{BH}}} = 2.25$, corresponding to approximately $N_* = N_{\text{BH}} \approx 48$ neighbors. This choice maintains localized enrichment and feedback near galaxies while avoiding excessive diffusion into low-density regions. For simulations run at different mass resolutions, these parameters can be adjusted to preserve consistent physical scales and overall accuracy.

The evolution of the smoothing length for all particles is computed using a modified approach based on [Thacker et al. \(2000\)](#), as described in [Appendix A.3](#). For subgrid particle transformations, each h_s is initialized from the volume of the progenitor particle according to the relation $h_s = n_{h_s} V^{1/3}$. This prescription applies when stars or wind particles are spawned from star-forming gas (with volume V_g) and when AGN particles are seeded or repositioned to stellar particle locations (with volume V_*).

When considering the gravitational contribution of each particle species, we adopt a single uniform softening length, ϵ_{soft} , to maintain consistent force resolution between dark matter and baryons. Gas smoothing lengths are constrained to remain larger than ϵ_{soft} to prevent spurious fragmentation near the local resolution limit. In contrast, stars and black holes, which do not participate in hydrodynamic forces, can employ much smaller smoothing lengths, down to $h_s = 0.01 \epsilon_{\text{soft}}$, enabling highly localized interaction kernels for enrichment and feedback. This approach preserves stable gravitational interactions even as individual smoothing lengths evolve dynamically.

A.3. Smoothing Length Integration

In the original CRK-HACC implementation (Section 3.6 of [FRO23](#)), the smoothing length update followed the method of [Thacker et al. \(2000\)](#), which stabilizes the neighbor count without requiring an iterative

solver,

$$h_i^{\text{T}} = h_i(1 - \lambda + \lambda \Delta_N), \quad (\text{A7})$$

where h_i^{T} is the Thacker estimate, λ is a weighting coefficient, and $\Delta_N^3 \equiv N_{\text{res}}/N_i = V_i n_{h_i}^3/h_i^3$ represents the ratio of target to measured neighbor counts defined for each species in the previous section. During drift operations, the smoothing length was adjusted accordingly, with passive particles additionally updating their volume using the continuity equation estimate from [Eq. \(A3\)](#).

However, when coupled with deeper timestepping hierarchies and abrupt subgrid transformations, this scheme can produce oscillatory smoothing length estimates as particles transition between active and passive states, undermining the original motivation for adopting the Thacker method.

To address this, we now compute a total smoothing length derivative, \dot{h}_i , that combines the Thacker neighbor constraint with the local volumetric continuity condition. This approach ensures that both active and passive particles evolve h_i smoothly and continuously, preventing discontinuities in the neighbor count.

For each active particle, \dot{h}_i is computed as

$$\dot{h}_i = \dot{h}_i^{\text{T}} + \dot{h}_i^{\text{cont}}, \quad (\text{A8})$$

where

$$\dot{h}_i^{\text{T}} = \frac{h_i^{\text{T}} - h_i}{\Delta t_a}, \quad \dot{h}_i^{\text{cont}} = \frac{1}{3} h_i \nabla \cdot \mathbf{v}_i, \quad (\text{A9})$$

and Δt_a is the current active timestep. This combined formulation is analogous to the smoothing length update in [Springel et al. \(2001\)](#). At each drift operation (integrated with timestep $\Delta t \leq \Delta t_a$), all particles update their smoothing length using the stored \dot{h}_i ,

$$h_i^{\text{new}} = h_i \exp\left[\frac{\dot{h}_i}{h_i} \Delta t\right], \quad (\text{A10})$$

yielding a smooth and continuous estimate even in the presence of deep integration hierarchies and rapid subgrid-driven changes.

Likewise, passive state variables such as volume and density are updated as

$$V_i^{\text{new}} = \left(\frac{h_i^{\text{new}}}{n_h}\right)^3, \quad \rho_i^{\text{new}} = \rho_i \exp\left[-\nabla \cdot \mathbf{v}_i \Delta t\right]. \quad (\text{A11})$$

This modification retains the advantages of the original Thacker method — avoiding a fully implicit solver — while ensuring that the smoothing length evolves in a physically stable and well-behaved manner, even under the abrupt transitions imposed by the subgrid operators.

²² A common source of confusion in SPH implementations is that kernels are sometimes quoted with a radius of $2h$.

A.4. Adaptive Kick Corrections for Timestep Refinement

In CRK-HACC, hydrodynamic evolution is advanced using a hierarchical kick-drift-kick (KDK) integrator applied to particle leaves (subdomains) grouped into power-of-two timestep bins (see Section 3.1 in FRO23). In typical configurations, each leaf contains a few hundred particles. The following describes the timestep refinement procedures implemented to handle abrupt changes in momentum and energy introduced by subgrid source terms.

All particles within a leaf evolve over an assigned active timestep interval Δt_a , determined by the local CFL condition, while the smallest timestep among all leaves on a given rank is denoted Δt_{\min} . Over an active interval, the standard KDK update for each leaf is

$$\begin{aligned} \text{K: } \mathbf{v}^{1/2} &= \mathbf{v}^0 + \frac{1}{2} \mathbf{a}^0 \Delta t_a \\ \text{D: } \mathbf{x}^1 &= \mathbf{x}^0 + \mathbf{v}^{1/2} \Delta t_a \\ \text{K: } \mathbf{v}^1 &= \mathbf{v}^{1/2} + \frac{1}{2} \mathbf{a}^1 \Delta t_a \\ &= \mathbf{v}^0 + \frac{1}{2} (\mathbf{a}^0 + \mathbf{a}^1) \Delta t_a \end{aligned} \quad (\text{A12})$$

where superscripts 0 and 1 denote quantities evaluated at the beginning and end of the timestep, respectively.

Particle leaves on coarser timestep levels become passive after completing their first kick. During this passive period, the drift operator is executed incrementally by accumulating position updates over smaller substeps. The total displacement across the full active interval is given by

$$\mathbf{x}^1 = \mathbf{x}^0 + \sum_j \mathbf{v}^{1/2} \Delta t_{\min}^{(j)}, \quad (\text{A13})$$

where each $\Delta t_{\min}^{(j)}$ denotes the smallest local-rank timestep applied during subinterval j , and $\sum_j \Delta t_{\min}^{(j)} = \Delta t_a$. Once the accumulated drift spans the entire active interval, the second kick is applied to complete the KDK cycle.

Following Saitoh & Makino (2009), we apply a timestep limiter that dynamically refines the interval assigned to each leaf when local conditions — such as abrupt subgrid injections or rapid force variations — demand higher temporal resolution. When the Saitoh limiter is triggered, certain particle leaves may transition to a shorter timestep partway through their KDK sequence. To maintain consistency in the velocity state, the partially completed half-kick is adjusted to match the refined interval.

Specifically, if the timestep assigned to a leaf is refined from an initial Δt_a to a shorter $\Delta t_b < \Delta t_a$ midway through a KDK cycle, the first half-kick is corrected as

$$\mathbf{v}^{1/2} = \mathbf{v}^0 + \frac{1}{2} \mathbf{a}^0 \Delta t_a \implies \mathbf{v}^{1/2} = \mathbf{v}^0 + \frac{1}{2} \mathbf{a}^0 \Delta t_b. \quad (\text{A14})$$

This adjustment re-synchronizes the stored velocity with the smaller refined timestep, where superscripts 0 and 1 denote the start and end of the refined interval. After the drift step completes over the shorter interval Δt_b , the second half-kick is applied using the updated local acceleration \mathbf{a}^1 ,

$$\mathbf{v}^1 = \mathbf{v}^{1/2} + \frac{1}{2} \mathbf{a}^1 \Delta t_b = \mathbf{v}^0 + \frac{1}{2} (\mathbf{a}^0 + \mathbf{a}^1) \Delta t_b. \quad (\text{A15})$$

If the updated acceleration necessitates an even shorter, CFL-constrained timestep Δt_c — for example following a strong stochastic subgrid event — the final kick is further refined using a piecewise-constant approximation:

$$\mathbf{v}^1 = \mathbf{v}^0 + \mathbf{a}^0 (\Delta t_b - \Delta t_c) + \frac{1}{2} (\mathbf{a}^0 + \mathbf{a}^1) \Delta t_c. \quad (\text{A16})$$

In practice, this correction advances particles under constant acceleration \mathbf{a}^0 until the remaining portion of the step is completed with a standard KDK update using \mathbf{a}^0 and \mathbf{a}^1 over the refined interval Δt_c . This ensures that the final velocity remains consistent with the resolved timestep hierarchy, preventing spurious excursions during completion of Δt_b and allowing the leaf to reduce its timestep level to Δt_c in the next KDK cycle. The approach mirrors the timestep adjustments described by Durier & Dalla Vecchia (2011) and maintains robustness under abrupt subgrid refinements.

A final modification concerns evaluation of the drift operation described in Eq. (A13) for passive particles. Following FRO23, we adopt a piecewise-parabolic trajectory consistent with the constant-acceleration approximation used for passive motion in the KDK hierarchy. Instead of drifting with a fixed half-step velocity $\mathbf{v}^{1/2}$, a local half-step velocity $\mathbf{v}_j^{1/2}$ is computed for each drift subinterval, ensuring that the particle follows the parabolic path implied by constant acceleration rather than a linear trajectory across the full active step:

$$\mathbf{v}_j^{1/2} = \mathbf{v}^{1/2} + \mathbf{a}^0 \left[\Delta t_{\text{elapse}} + \frac{1}{2} (\Delta t_{\min}^{(j)} - \Delta t_a) \right], \quad (\text{A17})$$

where $\Delta t_{\text{elapse}} \equiv \sum_{k=1}^{j-1} \Delta t_{\min}^{(k)}$ is the elapsed time since the start of the active interval up to (but not including) substep j . Applying this correction, the total drift displacement in Eq. (A13) becomes

$$\mathbf{x}^1 = \mathbf{x}^0 + \sum_j \mathbf{v}_j^{1/2} \Delta t_{\min}^{(j)}, \quad (\text{A18})$$

ensuring that passive drifts follow a trajectory consistent with piecewise-constant acceleration.

This drift modification does not alter the stored $\mathbf{v}^{1/2}$ state but is important for maintaining accurate passive positions during limiter-triggered mid-step refinements

and for ensuring consistent neighbor interactions between active and passive particles at smaller timesteps. If no refinements occur, the final integrated position at the end of the active interval is equivalent to that obtained from a drift computed with a constant $\mathbf{v}^{1/2}$.

Since all particles drift on the smallest timestep interval — and the integration hierarchy can extend to much deeper levels under subgrid physics — single-precision arithmetic may become insufficient to accumulate small displacements accurately over many drift steps. To maintain long-term numerical stability, position updates are accumulated in double precision on the GPU, while force kernels and host-side particle states remain in single precision. This strategy preserves performance for the dominant force calculations and ensures accurate trajectories with only a modest increase in GPU memory footprint. Since CRK-HACC already evolves sub-volumes entirely on the GPU with numerous derived state arrays allocated, this additional storage cost is negligible in practice.

B. SELF-SIMILARITY WITH COOLING

The validation of cosmological simulations is complicated by the nonlinear nature of gravitational collapse, which precludes straightforward comparison to analytic predictions. An effective strategy to address this challenge is to perform simulations in which the only physical scale is the amplitude of density fluctuations. In this way, structure formation evolves in a temporally self-similar manner, enabling validation of the simulation solver even in the nonlinear regime.

We employed this method in [FRO23](#) to validate the non-radiative CRK-HACC hydrodynamic solver. The subgrid models introduced in this paper incorporate a multitude of physical scales, making them incompatible with a scale-free framework. However, [Owen et al. \(1998\)](#) demonstrated that self-similar evolution can still be preserved under radiative cooling, provided that the cooling function follows a power law whose slope is a specific function of the spectral index of density perturbations. While this cooling function is not physically realistic, it serves as a useful idealization for validating the radiative solver in the nonlinear regime.

In what follows, we assume an Einstein–de Sitter (EdS) cosmology with $(\Omega_c, \Omega_b, h) = (0.8, 0.2, 0.5)$ and an initial power spectrum $P(k) = A_0 k^{n_s}$, where the spectral index is $n_s = -2$ (similar to Λ CDM on the scales considered), and the normalization A_0 is set by requiring $\sigma_8 = 0.5$. The cooling function takes the form

$$\frac{\Lambda(u)}{n_H^2} = A_1 u^\beta, \quad (\text{B19})$$

with self-similarity enforced by requiring that the cooling time of a halo collapsing at the nonlinear scale is a fixed fraction, f_* , of the Hubble time. This condition constrains the exponent β to depend on the spectral index as

$$\beta = \frac{3}{2} \cdot \frac{3 + n_s}{1 - n_s} + 1, \quad (\text{B20})$$

as derived in [Owen et al. \(1998\)](#). For our choice of $n_s = -2$, self-similarity requires a power-law slope of $\beta = 1.5$.

The normalization

$$A_1 = \frac{1}{f_*} \frac{H_0}{\rho_*} \left[\frac{T_* k_B}{\mu m_H (\gamma - 1)} \right]^{1-\beta}, \quad (\text{B21})$$

is set by the free parameter f_* . We use asterisks to denote quantities evaluated at the nonlinear collapse scale, which — as shown in [FRO23](#) — is characterized by the following mass, density, radius, temperature, and entropy:

$$\begin{aligned} M_* &= 4.05 \times 10^{11} a^6 h^{-1} M_\odot, \\ \rho_* &= 5.55 \times 10^{13} a^{-3} h^2 M_\odot \text{Mpc}^{-3}, \\ R_* &= 0.12 a^3 h^{-1} \text{Mpc}, \\ T_* &= 5.19 \times 10^5 a^3 \text{K}, \\ S_* &= -7.94 + 5 \ln(a). \end{aligned} \quad (\text{B22})$$

We run three simulations, each containing $N = 2 \times 512^3$ dark matter and baryonic particles in a box of width $L_{\text{box}} = 40 h^{-1} \text{Mpc}$, with mass resolutions of $m_{\text{dm}} = 1.06 \times 10^8 h^{-1} M_\odot$ and $m_b = 2.65 \times 10^7 h^{-1} M_\odot$. The three runs differ only in the normalization of the cooling law, with the cooling time set to $f_* = 1, 10, 100$ times the Hubble time at the nonlinear collapse scale. Each simulation evolves from $z = 200$ to 0 with a gravitational softening length of $\epsilon_{\text{soft}} = 4.88 h^{-1} \text{kpc}$. These tests include only radiative gas cooling, with all prescriptions for star formation, winds, and AGN feedback disabled.

We identify spherical overdensity (SO) halos using a threshold of $\Delta_c = 200$ relative to the critical density and compare halos across redshift to assess temporal self-similarity. Only halos with mass $M_{200c} \geq 3 \times 10^{11} h^{-1} M_\odot$ are included, as this threshold was shown by [FRO23](#) to avoid artificial mass segregation effects. To minimize scatter from major mergers, we further restrict the sample to relaxed halos where the offset between the potential minimum and the center of mass is less than 7% of the SO radius, R_{200c} ([Child et al. 2018](#)).

The results from the three simulations are summarized in Figure 15, which shows halo baryon density, temperature, and entropy as functions of scaled mass across

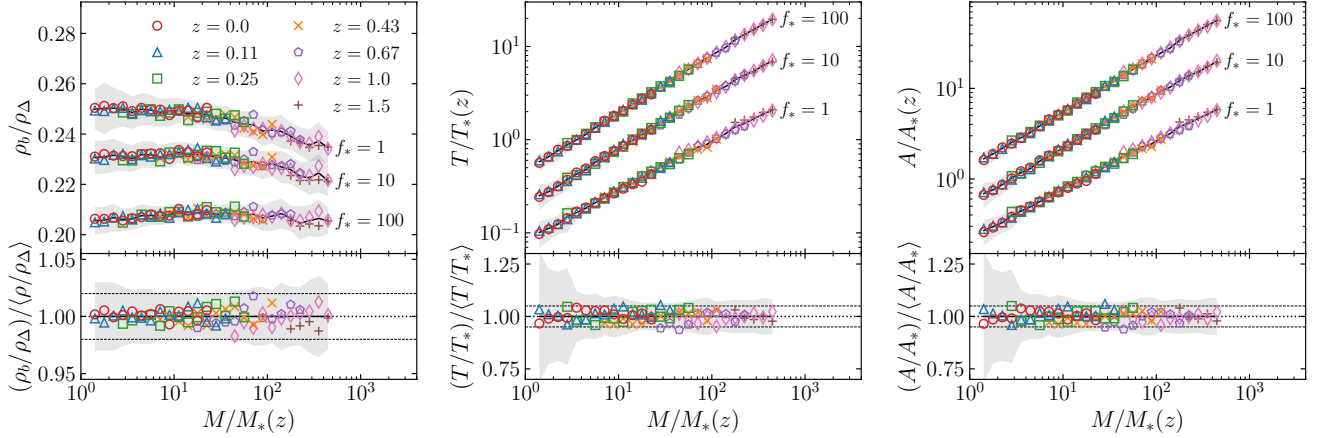


Figure 15. Baryon density (left), temperature (center), and entropy (right) as functions of scaled halo mass for three scale-free radiative simulations parameterized by the cooling amplitude f_* . Density is normalized to the spherical overdensity threshold $\rho_\Delta = 200\rho$, while mass, temperature, and entropy are normalized to the redshift-dependent nonlinear scales defined in Eq. (B22). We plot the entropic function A , related to the entropy by $S \propto \ln A$. Each marker denotes the mean value for halos in a given redshift and mass bin containing at least ten halos; only bins with contributions from more than one redshift sample are shown. The solid black line traces the overall mean across all redshifts, and the shaded gray band indicates the corresponding standard deviation. The bottom panels show the deviation of all measurements from the mean curve. Horizontal dashed lines mark $\pm 2\%$, $\pm 5\%$, and $\pm 5\%$ spreads for the left, center, and right panels, respectively. To reduce visual overlap in the top panel of the density plot, the $f_* = 10$ and $f_* = 1$ curves are shifted upward by 0.01 and 0.02, respectively.

two decades, for redshifts $0 \leq z \leq 1.5$. The density refers specifically to the baryonic component, calculated as $\rho_b = 3M_{200c,b}/(4\pi R_{200c}^3)$, where $M_{200c,b}$ is the total baryonic mass within radius R_{200c} . For temperature, we compute the mass-weighted average over all baryonic particles in each halo. The two quantities are combined into the entropy $S = \ln(T/\rho_b^{2/3})$. Each marker in the figure denotes the mean value for halos within a given M/M_* (where M denotes M_{200c}) and redshift bin.

To assess self-similarity, we compare halos at fixed M/M_* across different redshifts. For example, at $M/M_* = 20$, the sample includes five redshifts between $z = 0$ and $z = 0.67$. Since $M_* \propto a^6$, the corresponding physical halo masses in this bin differ by more than an order of magnitude. Despite this variation, the density, temperature, and entropy agree to within a few percent across redshifts in this bin. This low level of scatter is consistent across the full scaled mass range for all three radiative simulations, indicating a strong degree of self-similarity. As expected, the simulation with more efficient cooling (i.e., lower f_*) exhibits higher baryon density, lower temperature, and correspondingly lower entropy.

C. CLUSTER CODE COMPARISON

We present results from CRK-HACC subgrid runs initialized with the nIFTy dataset (Sembolini et al. 2016a). The nIFTy initial conditions were generated using a zoom-in technique (Klypin et al. 2001) to extract a massive galaxy cluster within the large-volume Multidark

simulation (Prada et al. 2012). The adopted cosmology is WMAP-7+BAO+SNI (Komatsu et al. 2011), with parameters $(\Omega_m, \Omega_b, \Omega_\Lambda, n_s, \sigma_8, h) = (0.27, 0.0469, 0.73, 0.95, 0.82, 0.7)$. In the zoomed region, the highest-resolution particle masses are $m_{\text{dm}} = 9.01 \times 10^8 h^{-1} M_\odot$ for dark matter and $m_b = 1.9 \times 10^8 h^{-1} M_\odot$ for baryons.

The nIFTy initial conditions were first used by Sembolini et al. (2016a) to compare various cosmological codes employing non-radiative hydrodynamic solvers. We extended this comparison to the non-radiative CRK-HACC solver in FRO23, where we found excellent agreement with both Eulerian and modern SPH codes. This agreement is particularly notable since modern SPH methods typically require artificial conductivity to match Eulerian codes, but no such treatment is necessary within the CRKSPH framework.

Here, we further extend our comparison to the radiative hydrodynamic simulations presented in Sembolini et al. (2016b), which include a broad range of methods: grid-based (RAMSES; Teyssier 2002), hybrid moving-mesh (AREPO; Springel 2010), modern SPH (G3-X; Beck et al. 2016; G3-PESPH; Huang et al. 2019; G3-MAGNETICUM; Hirschmann et al. 2014), and traditional SPH codes (G3-MUSIC; Sembolini et al. 2013; G3-OWLS; Schaye et al. 2010; G2-X; Pike et al. 2014). In addition, these codes implement a wide variety of subgrid models for cooling, star formation, wind, and AGN feedback. To compare against this suite, we perform two CRK-HACC runs using the nIFTy initial conditions: one

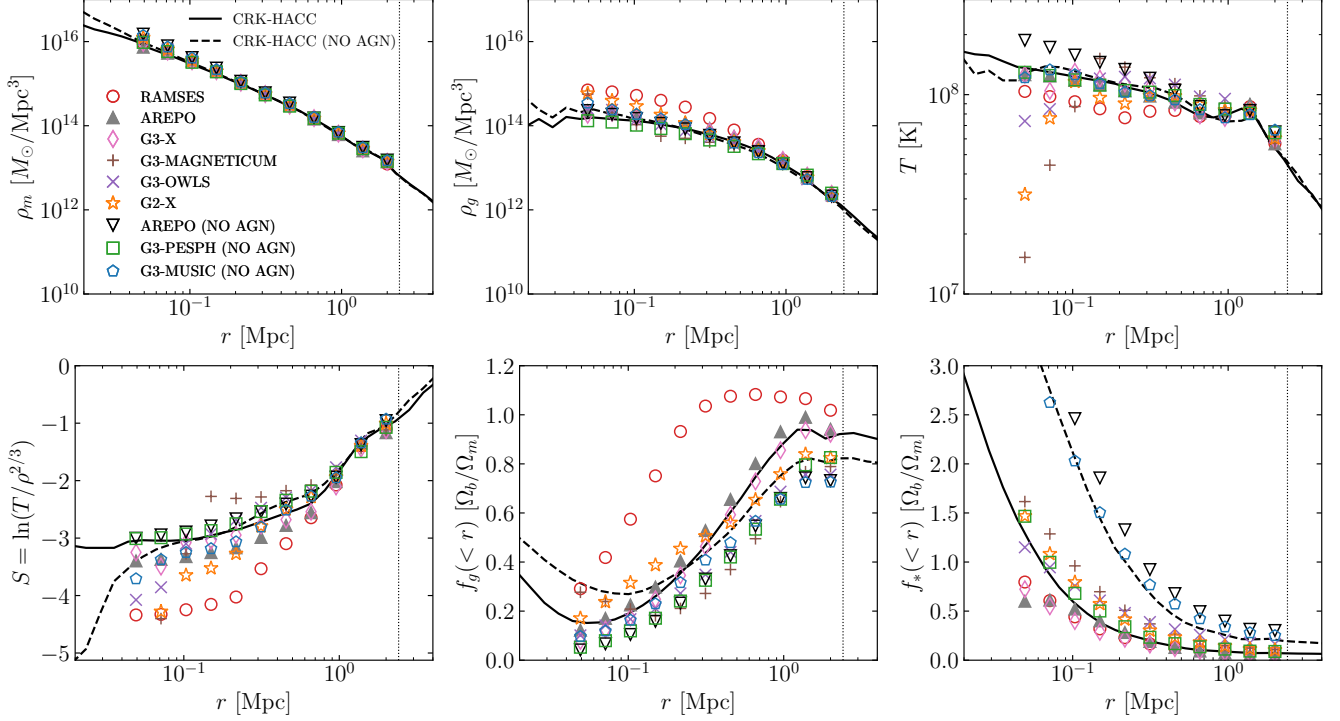


Figure 16. Clockwise from top left: Radial profiles of the total matter density, gas density, temperature, stellar fraction, gas fraction, and entropy for the nIFTy cluster at $z = 0$. Solid and dashed lines represent the CRK-HACC subgrid runs with and without AGN feedback, respectively. Symbols show results from the simulations presented in Sembolini et al. (2016b). The vertical dotted line in each panel marks $R_{200c} = 2.41$ Mpc, the cluster radius in the CRK-HACC run with full subgrid physics.

including the full set of subgrid models described in this work, and one omitting AGN feedback. Conveniently, the mass resolution in the nIFTy zoom-in region closely matches that used for calibrating our subgrid models (Section 3), allowing us to directly apply our fiducial parameters.

We find the main cluster to have a mass $M_{200c} = 1.59 \times 10^{15} M_{\odot}$ ($1.61 \times 10^{15} M_{\odot}$) and radius $R_{200c} = 2.41$ Mpc (2.42 Mpc) at $z = 0$ in the full subgrid (non-AGN) simulation. These values are consistent with the range reported by Sembolini et al. (2016b), with the slight increase in mass in the non-AGN run also observed in the two AREPO simulations. Radial profiles of the main cluster from our two runs are compared to the full suite of radiative nIFTy simulations in Figure 16.

As noted by Sembolini et al. (2016b), systematic differences between Eulerian and traditional SPH codes are largely washed out once subgrid physics is included, particularly for this massive, unrelaxed cluster. Instead, all codes consistently produce entropy cores, regardless of the presence of AGN feedback; a trend reproduced in our two CRK-HACC runs. The primary effect of AGN feedback is the suppression of star formation on small scales, along with a slightly steeper gas fraction profile.

Overall, CRK-HACC produces nIFTy cluster profiles in broad agreement with those from current state-of-the-art hydrodynamic codes.

D. GENERATED CLOUDY TABLES

The inputs to CLOUDY specify a gas of hydrogen number density n_H [cm^{-3}], temperature T [K], helium abundance n_{He}/n_H , individual metal abundances n_{Z_i}/n_H , and redshift z . We provide CLOUDY with the input radiation field from either Faucher-Giguère (2020) or optionally Haardt & Madau (2012) (hereafter FG20 and HM12), modeling a uniform time-dependent UV background. As was done in Vogelsberger et al. (2013), to incorporate self-shielding effects for high-density gas — where the optically thin approximation is invalid — we attenuate the background radiation field using a density- and redshift-dependent fit from Appendix A in Rahmati et al. (2013). Namely, the correction amplitude A_{corr} , follows:

$$A_{\text{corr}} = (1 - f) \left[1 + \left(\frac{n_H}{n_0} \right)^{\beta} \right]^{\alpha_1} + f \left[1 + \left(\frac{n_H}{n_0} \right) \right]^{\alpha_2} \quad (\text{D23})$$

where coefficients $(f, n_0, \alpha_1, \alpha_2, \beta)$ are redshift-dependent (specified in Table A1 in Rahmati et al.

2013), and linearly interpolated. Equation (D23) asymptotically tends to unity for low-density gas, i.e. no correction, and rapidly decreases toward zero at high density. We do not apply any attenuation for redshift $z > 6$.

Although this approach does not rigorously simulate radiative transfer, it self-consistently modifies our cooling treatment using an approximated attenuation that was measured by post-processing cosmological simulations using the radiative transfer code TRAPHIC (Pawlik & Schaye 2008, 2011).

To tabulate radiative cooling rates, we ran a suite of CLOUDY simulations across a broad parameter space encompassing conditions relevant to cosmological gas. Specifically, we sampled hydrogen number density n_{H} over the range $\log_{10}(n_{\text{H}} [\text{cm}^{-3}]) \in [-8, +5]$ using 200 points, and temperature $\log_{10}(T [\text{K}]) \in [0, 9]$ with 226 points. Metallicity was parameterized using the solar-scaled factor R (defined in Eq. (7)), which was sampled linearly over the range $R \in [0, 10]$ with 50 values. The helium composition was parameterized using the helium mass fraction assuming zero metallicity $Y_{Z=0}$, sampled linearly at 5 values in the range $Y_{Z=0} \in [0.25, 0.37]$. This quantity is mapped to the helium abundance required by CLOUDY via the relation:

$$\frac{n_{\text{He}}}{n_{\text{H}}} = \frac{Y_{Z=0}}{1 - Y_{Z=0}} \cdot \frac{m_{\text{H}}}{m_{\text{He}}}, \quad (\text{D24})$$

as derived from Eq. (9). The advantage of parameterizing the table by $Y_{Z=0}$ is that it is metallicity independent, as opposed to directly using the total helium fraction Y .

We generated separate tables for redshifts linearly sampled in scale factor using 50 values between $z = 0$ and $z = 15$ for the HM12 model, and capped at $z = 7.7$ for the FG20 model due to discontinuities in the cooling rates at higher redshift. At runtime, for any particle with properties $n_{\text{H},i}, T_i, X_i, Y_i, Z_i, z_i$, the corresponding R_i and $Y_{Z=0,i}$ values are computed using Eq. (11) and the transformation

$$\frac{Y_i}{X_i} = \frac{Y_{Z=0,i}}{1 - Y_{Z=0,i}}.$$

The simulation then identifies the two tabular redshifts z_1 and z_2 that bracket z_i , and performs linear interpolation across all five parameters — $n_{\text{H}}, T, R, Y_{Z=0}$, and z — to compute the local cooling function Λ_i .

In practice, simulation particles evolve internal energy $u \propto T/\mu$, rather than temperature. Thus, for consistency we tabulate and interpolate CLOUDY cooling rates as a function of T/μ . The mean molecular weight (per

particle) is defined as,

$$\mu = \frac{\bar{m}}{m_{\text{H}}} = \frac{1}{m_{\text{H}}} \frac{n_{\text{H}}m_{\text{H}} + n_{\text{He}}m_{\text{He}} + \sum_i n_{Z_i}m_{Z_i} + n_{\text{e}}m_{\text{e}}}{n_{\text{H}} + n_{\text{He}} + \sum_i n_{Z_i} + n_{\text{e}}} \approx \frac{1}{X + Y \frac{m_{\text{H}}}{m_{\text{He}}} + Z \sum_i \frac{m_{\text{H}}}{m_{Z_i}} + X \frac{n_{\text{e}}}{n_{\text{H}}}} \quad (\text{D25})$$

where \bar{m} is the mean mass of the gas, and we ignore the electron mass contribution ($n_{\text{e}}m_{\text{e}}$).

In addition to storing the tabulated cooling rates Λ , we also save several CLOUDY output quantities that are used in analysis, including values relevant for X-ray and Lyman- α observables. These include the neutral hydrogen abundance n_{HI} , the free electron number density n_{e} , the mean molecular weight μ , and the volumetric emissivity $J_{E_{\text{min}}-E_{\text{max}}}$ [$\text{erg cm}^{-3} \text{s}^{-1}$], which is used to compute luminosity measurements. The high-bandwidth memory and parallel compute capacity of the GPU enable efficient tabular lookups and interpolation across all CLOUDY outputs, making the five-dimensional tables well-suited for on-the-fly evaluation of cooling and emission properties.

Following Braspenning et al. (2024), the emissivity is calculated by integrating the CLOUDY-provided continuous emission coefficient ϵ_{ν} over a spectral energy interval E_{min} to E_{max} :

$$J_{E_{\text{min}}-E_{\text{max}}} = \int_{E_{\text{min}}}^{E_{\text{max}}} \frac{\epsilon_{\nu}}{E_{\nu}} dE_{\nu}, \quad (\text{D26})$$

where E_{ν} is the midpoint spectral energy of each frequency bin. The integrated energy bands we store include the bolometric range (0.5-10 keV), the ROSAT band (0.5-2.0 keV), and the low (0.2-2.3 keV) and high (2.3-8.0 keV) eROSITA bands. These bands are defined in the rest frame at redshift zero and are scaled by a factor of $1+z$ in the integral, with $E_{\text{min}}(z) = (1+z) E_{\text{min}}^{z=0}$ and $E_{\text{max}}(z) = (1+z) E_{\text{max}}^{z=0}$.

Table 4 provides an example CLOUDY parameter file used to sample a fixed $n_{\text{H},i}, X_i, Y_i, Z_i, z_i$ for all temperature values. Occasionally, CLOUDY fails to converge on an answer, typically at low redshift and high density, in which case we linearly interpolate an answer from the nearest converged sample points.

For completeness, we also store individual components of the emergent emission spectrum, which outputs direct and reflected contributions to both the diffuse continuum and line emission in XSPEC-compatible FITS format.²³ These tables report photon fluxes in units

²³ XSPEC is a spectral fitting software package widely used in X-ray astronomy; see <https://heasarc.gsfc.nasa.gov/xanadu/xspec/>.

Table 4. Example CLOUDY parameter file

| Input Command | Notes |
|--|--|
| hden LOGNH | Sets the log hydrogen number density, LOGNH, sampled at 200 points in $\log_{10}(n_{\text{H}} [\text{cm}^{-3}]) \in [-8, +5]$. |
| element abundance helium NHE linear | Sets the helium abundance, NHE, computed using Eq. (D24), and sampled at 5 points in $Y_{\text{Z}=0} \in [0.25, 0.37]$. |
| metals R linear | Sets the metal abundance with R following equation Eq. (7), sampled at 50 points in $R \in [0, 10]$. |
| constant temperature 0.0 vary grid 0.0, 9.0, 0.04 ncpus 1 | Sets the temperature grid from 226 points in $\log_{10}(T [\text{K}]) \in [0, 9]$. |
| CMB redshift Z | Sets the CMB at redshift Z, sampled at 50 points in $a = 1/(1+z)$ from $z = 0$ to 7.7 (15) for the FG20 (HM12) UV model. |
| table HM12 redshift Z factor LOGA | Sets the UV background at redshift Z, with the log attenuation factor, LOGA, computed using Eq. (D23). The FG20 model is applied by replacing the HM12 source file, <code>hm12_galaxy.ascii</code> , with the FG20 data. |
| stop zone 1 | Sets the stopping condition and iterative convergence for single-zone models. |
| iterate to convergence | |
| set continuum resolution 1.0 | Sets the frequency resolution to its default value. |
| save grid last "output_grid" | Saves the failure status of the run. |
| save cooling last "output_cooling" | Saves the cooling rate. |
| save overview last "output_overview" | Saves the heating rate, neutral fraction, and free electron abundance. |
| save diffuse continuum last "output_diffuse" | Saves the continuous emission coefficient used in Eq. (D26). |
| save xspec atable lines last "output_lines" | Saves the XSPEC line emission additive table. |
| save xspec atable reflected lines last "output_reflect_lines" | Saves the XSPEC reflected line emission additive table. |
| save xspec atable diffuse continuum last "output_contin_diffuse" | Saves the XSPEC diffuse continuum emission additive table. |
| save xspec atable reflected diffuse continuum last "output_reflect_diffuse" | Saves the XSPEC reflected diffuse continuum emission additive table. |
| save xspec mtable last "output_mtable" | Saves the XSPEC multiplicative table. |
| save radius last "output_rad" | Saves the cloud radius. |

of $[\text{photons s}^{-1} \text{cm}^{-2} \text{bin}^{-1}]$, and offer an alternative, photon-based format suitable for XSPEC-style modeling and mock observation pipelines. The tables are additive, and one can reconstruct the total volume emissivity by summing all components, dividing by the CLOUDY radius output, and multiplying by the bin-centered photon energy and bin width.

E. STELLAR ENRICHMENT INTEGRATION

We present here formulae for the integrated mass loss from supernovae and stellar winds, based on the rates and yields provided in FIRE3. These integrated expressions are convenient for two reasons. First, they ensure that cumulative mass loss is independent of the timestep size. Second, in cosmological simulations with relatively coarse timesteps, on the order of 1–10 Myr, they avoid significant errors in cumulative mass loss that would otherwise result from evaluating the rates instantaneously

at the start and end of each timestep. In what follows, we measure time in Myr and compute the mass loss over time t_0 to $t_1 = t_0 + \Delta t$. Rates are expressed in Gyr^{-1} per unit solar mass.

E.1. Supernovae Mass Loss

We begin with the SN mass loss obtained by integrating Eq. (42). For Type Ia SN, the ejecta mass is fixed at $M^{\text{Ia}} = 1.4 M_{\odot}$ and is composed entirely of metals. The SN Ia rate follows

$$R^{\text{Ia}}(t) = \begin{cases} 0, & t < t_r; \\ a(t/t_r)^c, & t \geq t_r; \end{cases} \quad (\text{E27})$$

where $a = 8.3 \times 10^{-3}$, $c = -1.1$, and $t_r = 44$ Myr. The integrated mass loss evaluates to

$$\frac{\Delta M_{T,Z}^{\text{Ia}}}{M_*} = M^{\text{Ia}} \left(\frac{a}{c+1} \frac{t^{c+1}}{t_r^c} \Big|_{\max(t_0, t_r)}^{t_1} \right), \quad (\text{E28})$$

for $t_l \geq t_r$ and 0 otherwise. As stated above, $\Delta M_Y^{\text{la}} = 0$.

For CC SN, the ejecta mass has time dependence:

$$M_{\text{CC}}(t) = \begin{cases} M_0(t/t_m)^{c_{m1}}, & t \leq t_m; \\ M_0(t/t_m)^{c_{m2}}, & t > t_m; \end{cases} \quad (\text{E29})$$

where $M_0 = 10 M_\odot$, $t_m = 6.5$, and $(c_{m1}, c_{m2}) = (-2.22, -0.267)$. The CC SN rate follows:

$$R_{\text{CC}}(t) = \begin{cases} 0, & t \leq t_{r1} \text{ or } t > t_{r3}; \\ a_{r1}(t/t_{r1})^{c_{r1}}, & t_{r1} < t \leq t_{r2}; \\ a_{r2}(t/t_{r2})^{c_{r2}}, & t_{r2} < t \leq t_{r3}; \end{cases} \quad (\text{E30})$$

where $(a_{r1}, a_{r2}, a_{r3}) = (0.39, 0.51, 0.18)$, $(t_{r1}, t_{r2}, t_{r3}) = (3.7, 7, 44)$, and $c_{rj} \equiv \ln(a_{r_{j+1}}/a_{r_j})/\ln(t_{r_{j+1}}/t_{r_j})$. The integrated total mass loss becomes

$$\frac{\Delta M_T^{\text{CC}}}{M_*} = F_{11}^T(t_{r1}, t_m) + F_{21}^T(t_m, t_{r2}) + F_{22}^T(t_{r2}, t_{r3}), \quad (\text{E31})$$

where we define the function

$$F_{ij}^T(t_l, t_u) \equiv \frac{M_0 a_{r_j}}{\alpha_{ij} + 1} \frac{t^{\alpha_{ij}+1}}{t_m^{c_{m_i}} t_{r_j}^{c_{r_j}}} \bigg|_{[t_l, t_0, t_u]}^{[t_l, t_1, t_u]}, \quad (\text{E32})$$

with coefficient $\alpha_{ij} \equiv c_{m_i} + c_{r_j}$ and the notation $[t_l, t, t_u] \equiv \min[\max(t_l, t), t_u]$ conveys that t is bounded within $[t_l, t_u]$.

The FIRE-3 helium yield is modeled using piecewise power-laws:

$$f_Y(t) = \begin{cases} 0, & t \leq t_{f1} \text{ or } t > t_{f5}; \\ a_{f1}^Y(t/t_{f1})^{c_{f1}^Y}, & t_{f1} < t \leq t_{f2}; \\ \dots & \\ a_{f4}^Y(t/t_{f4})^{c_{f4}^Y}, & t_{f4} < t \leq t_{f5}; \end{cases} \quad (\text{E33})$$

where $(a_{f1}^Y, a_{f2}^Y, a_{f3}^Y, a_{f4}^Y, a_{f5}^Y) = (0.461, 0.33, 0.358, 0.365, 0.359)$, $(t_{f1}, t_{f2}, t_{f3}, t_{f4}, t_{f5}) = (3.7, 8, 18, 30, 44)$, and $c_{f_k}^Y \equiv \ln(a_{f_{k+1}}^Y/a_{f_k}^Y)/\ln(t_{f_{k+1}}/t_{f_k})$. The integrated helium mass loss evaluates to

$$\Delta M_Y^{\text{CC}}/M_* = F_{111}^Y(t_{r1}, t_m) + F_{211}^Y(t_m, t_{r2}) + F_{221}^Y(t_{r2}, t_{f2}) + F_{222}^Y(t_{f2}, t_{f3}) + F_{223}^Y(t_{f3}, t_{f4}) + F_{224}^Y(t_{f4}, t_{f5}), \quad (\text{E34})$$

where

$$F_{ijk}^Y(t_l, t_u) \equiv \frac{M_0 a_{r_j} a_{f_k}^Y}{\alpha_{ijk}^Y + 1} \frac{t^{\alpha_{ijk}^Y+1}}{t_m^{c_{m_i}} t_{r_j}^{c_{r_j}} t_{f_k}^{c_{f_k}^Y}} \bigg|_{[t_l, t_0, t_u]}^{[t_l, t_1, t_u]}, \quad (\text{E35})$$

and the coefficient $\alpha_{ijk}^Y \equiv c_{m_i} + c_{r_j} + c_{f_k}^Y$.

Table 1 of FIRE3 provides the coefficients $a_{f_k}^{Z_i}$ for nine metal elements whose mass fraction yields, $f_{Z_i}(t)$, are modeled in the same manner as helium in Eq. (E33). Since we do not track individual metal elements in CRK-HACC, we compute the total metal mass fraction yield, $f_Z(t) = \sum_{i=1}^9 f_{Z_i}(t)$, and fit the same functional form given in Eq. (E33) to $f_Z(t)$. Our fitting procedure gives $(a_{f1}^Z, a_{f2}^Z, a_{f3}^Z, a_{f4}^Z, a_{f5}^Z) = (0.2925, 0.164, 0.166, 0.0422, 0.0237)$ with $c_{f_k}^Z$ following the same definition as above. The integrated metal mass loss, ΔM_Z^{CC} , follows identically to Eqs. (E34) and (E35) with the coefficients $a_{f_k}^Y$ replaced by $a_{f_k}^Z$.

E.2. Stellar Outflows

Next we compute the stellar outflow mass loss by integrating Eq. (43). In FIRE-3, the mass loss rate is written as the sum of two terms, $f_w(t) = f_w^1(t) + f_w^2(t)$, which model wind loss from OB and AGB stars, respectively. The OB term is modeled as a piecewise power law:

$$f_w^1(t) = \begin{cases} a_{w0}(t/t_{w0})^{c_{w0}}, & t \leq t_{w1}; \\ a_{w1}(t/t_{w1})^{c_{w1}}, & t_{w1} < t \leq t_{w2}; \\ a_{w2}(t/t_{w2})^{c_{w2}}, & t_{w2} < t \leq t_{w3}; \\ a_{w3}(t/t_{w3})^{c_{w3}}, & t > t_{w3}; \end{cases} \quad (\text{E36})$$

where $(a_{w1}, a_{w2}, a_{w3}) = (3z_{\text{Fe}}^{0.87}, 20z_{\text{Fe}}^{0.45}, 0.6z_{\text{Fe}})$ with $a_{w0} = a_{w1}$, $(t_{w1}, t_{w2}, t_{w3}) = (1.7, 4, 20)$ with $t_{w0} = t_{w1}$, and $c_{w_i} = \ln(a_{w_{i+1}}/a_{w_i})/\ln(t_{w_{i+1}}/t_{w_i})$ with $c_{w0} = 0$ and $c_{w3} = -3.1$. We also have that $z_{\text{Fe}} \equiv 10^{[\text{Fe}/\text{H}]}$ which reduces to R in our model. We separate the AGB component into two terms, $f_w^2(t) = f_w^{2a}(t) + f_w^{2b}(t)$, with

$$f_w^{2a}(t) = a_{w4}(t_{w4}/t)^{1.6} e^{-(t_{w4}/t)^6} \\ f_w^{2b}(t) = a_{w4}(t_{w4}/t)^{1.6} [a_{w5}^{-1} + (t_{w4}/t)^2]^{-1}, \quad (\text{E37})$$

where $(a_{w4}, a_{w5}) = (0.11, 0.01)$ and $t_{w4} = 800$. Combining all of this, the total integrated mass loss is

$$\frac{\Delta M_T^{\text{w}}}{M_*} = F_0^T(0, t_{w1}) + F_1^T(t_{w1}, t_{w2}) + F_2^T(t_{w2}, t_{w3}) + F_3^T(t_{w3}, \infty) + \int_{t_0}^{t_1} f_w^{2a}(t) dt + \int_{t_0}^{t_1} f_w^{2b}(t) dt, \quad (\text{E38})$$

where

$$F_i^T(t_l, t_u) \equiv \frac{a_{w_i}}{c_{w_i} + 1} \frac{t^{c_{w_i}+1}}{t_{w_i}^{c_{w_i}}} \bigg|_{[t_l, t_0, t_u]}^{[t_l, t_1, t_u]}. \quad (\text{E39})$$

The last two integrals in Eq. (E38) cannot be solved analytically. Instead, we numerically evaluate each integral

and construct a fitting function made from a piecewise combination of straight line segments and tanh functions in log space. The fits are summarized in Table 5.

The helium yield is modeled by taking into account the formation of helium from nuclear hydrogen burning as well as the loss of helium to heavier elements during nuclear helium burning. More specifically, we have

$$f_Y(t) = X_* y_{\text{HHe}}(t) + Y_* [1 - y_{\text{HeC}}(t)], \quad (\text{E40})$$

where y_{HHe} (y_{HeC}) describes the formation (loss) of helium to hydrogen (helium) burning, and X_* and Y_* are the hydrogen and helium fractions of the SSP. The time dependence of the formation and loss channels is modeled in FIRE-3 using piecewise power laws:

$$y_j(t) = \begin{cases} a_{j0} (t/t_{j0})^{c_{j0}}, & t \leq t_{j1}; \\ a_{j1} (t/t_{j1})^{c_{j1}}, & t_{j1} < t \leq t_{j2}; \\ \dots & \dots \\ a_{jn} (t/t_{jn})^{c_{jn}}, & t_{jn} < t \leq t_{j_{n+1}}; \end{cases} \quad (\text{E41})$$

where $c_{jn} \equiv \ln(a_{j_{n+1}}/a_{jn})/\ln(t_{j_{n+1}}/t_{jn})$, $a_{j0} = a_{j1}$, and $t_{j0} = t_{j1}$. For y_{HHe} , we have $(a_{\text{HHe1}}, a_{\text{HHe2}}, a_{\text{HHe3}}, a_{\text{HHe4}}, a_{\text{HHe5}}) = \{0.4\min[(z_{\text{CNO}}+0.001)^{0.6}, 2], 0.08, 0.07, 0.042, 0.042\}$, $(t_{\text{HHe1}}, t_{\text{HHe2}}, t_{\text{HHe3}}, t_{\text{HHe4}}, t_{\text{HHe5}}) = (2.8, 10, 2300, 3000, 10^5)$, and $c_{\text{HHe0}} = 3$. We also have $z_{\text{CNO}} \equiv (Z_{*,\text{C}} + Z_{*,\text{N}} + Z_{*,\text{O}})/(Z_{\text{C}} + Z_{\text{N}} + Z_{\text{O}})_{\odot}$ which reduces to $\tilde{Z}_* \equiv Z_*/Z_{\odot}$ in our model. For y_{HeC} , we have $(a_{\text{HeC1}}, a_{\text{HeC2}}, a_{\text{HeC3}}, a_{\text{HeC4}}) = (10^{-6}, 0.001, 0.005, 0.005)$, $(t_{\text{HeC1}}, t_{\text{HeC2}}, t_{\text{HeC3}}, t_{\text{HeC4}}) = (5, 40, 10^4, 10^5)$, and $c_{\text{HeC0}} = 3$. The total integrated helium mass loss evaluates to

$$\frac{\Delta M_Y^w}{M_*} = Y_* \left(\frac{\Delta M_T^w}{M_*} - \int_{t_0}^{t_1} f_w(t) y_{\text{HeC}}(t) dt \right) + X_* \int_{t_0}^{t_1} f_w(t) y_{\text{HHe}}(t) dt. \quad (\text{E42})$$

As before, we separate the f_w term into its (integrable) OB term, f_w^1 , and its (non-integrable) AGB terms, f_w^{2a} and f_w^{2b} . The first integral in Eq. (E42) evaluates to

$$\begin{aligned} \int_{t_0}^{t_1} f_w y_{\text{HeC}} dt &= F_{00}^{\text{HeC}}(0, t_{w1}) + F_{10}^{\text{HeC}}(t_{w1}, t_{w2}) \\ &+ F_{20}^{\text{HeC}}(t_{w2}, t_{\text{HeC1}}) + F_{21}^{\text{HeC}}(t_{\text{HeC1}}, t_{w3}) \\ &+ F_{31}^{\text{HeC}}(t_{w3}, t_{\text{HeC2}}) + F_{32}^{\text{HeC}}(t_{\text{HeC2}}, t_{\text{HeC3}}) \\ &+ F_{33}^{\text{HeC}}(t_{\text{HeC3}}, t_{\text{HeC4}}) \\ &+ \int_{t_0}^{t_1} f_w^{2a} y_{\text{HeC}} dt + \int_{t_0}^{t_1} f_w^{2b} y_{\text{HeC}} dt, \end{aligned} \quad (\text{E43})$$

where

$$F_{ij}^s(t_l, t_u) \equiv \frac{a_{w_i} a_{s_j}}{\alpha_{ij} + 1} \frac{t^{\alpha_{ij}+1}}{t_{w_i}^{\alpha_{ij}+1} t_{s_j}^{\alpha_{ij}+1}} \bigg|_{[t_l, t_0, t_u]}^{[t_l, t_1, t_u]}, \quad (\text{E44})$$

with $\alpha_{ij} \equiv c_{w_i} + c_{s_j}$. As before, Table 5 provides fitting functions for the f_w^2 integrals in Eq. (E43). The second integral in Eq. (E42) evaluates to

$$\begin{aligned} \int_{t_0}^{t_1} f_w y_{\text{HHe}} dt &= F_{00}^{\text{HHe}}(0, t_{w1}) + F_{10}^{\text{HHe}}(t_{w1}, t_{\text{HHe1}}) \\ &+ F_{11}^{\text{HHe}}(t_{\text{HHe1}}, t_{w2}) + F_{21}^{\text{HHe}}(t_{w2}, t_{\text{HHe2}}) \\ &+ F_{22}^{\text{HHe}}(t_{\text{HHe2}}, t_{w3}) + F_{32}^{\text{HHe}}(t_{w3}, t_{\text{HHe3}}) \\ &+ F_{33}^{\text{HHe}}(t_{\text{HHe3}}, t_{\text{HHe4}}) + F_{34}^{\text{HHe}}(t_{\text{HHe4}}, t_{\text{HHe5}}) \\ &+ G(\tilde{Z}_*) \frac{t}{t_{\text{HHe2}}} \bigg|_{[0, t_0, t_{\text{HHe2}}]}^{[0, t_1, t_{\text{HHe2}}]} \\ &+ \int_{\max(t_0, t_{\text{HHe2}})}^{\max(t_1, t_{\text{HHe2}})} f_w^{2a} y_{\text{HHe}} dt \\ &+ \int_{\max(t_0, t_{\text{HHe2}})}^{\max(t_1, t_{\text{HHe2}})} f_w^{2b} y_{\text{HHe}} dt, \end{aligned} \quad (\text{E45})$$

where F_{ij}^{HHe} follows Eq. (E44). The final three terms in this expression arise from the $\int f_w^2 y_{\text{HHe}}$ integral which has metallicity dependence at early times, $t \leq t_{\text{HHe2}} = 10$ Myr, due to the presence of the $z_{\text{CNO}} = \tilde{Z}_*$ term in a_{HHe1} . To capture this metallicity dependence, we fit the function,

$$G(\tilde{Z}_*) = \begin{cases} \exp(g_l), & \tilde{Z}_* \leq \tilde{z}_l; \\ \exp\left[g_1 + g_2(\ln \tilde{Z}_* - g_4) + g_3(\ln \tilde{Z}_* - g_4)^2\right], & \tilde{z}_l < \tilde{Z}_* < \tilde{z}_u; \\ \exp(g_u), & \tilde{Z}_* \geq \tilde{z}_u; \end{cases} \quad (\text{E46})$$

to the numerical integral of $\int f_w^2 y_{\text{HHe}}$ evaluated from $t = 0$ to t_{HHe2} for different \tilde{Z}_* values. We find the best-fit coefficients $(g_l, g_1, g_2, g_3, g_4, g_u) = (-5.420649, -4.819271, 0.207927, 0.017928, -3.40815, -3.468966)$ with $(\tilde{z}_l, \tilde{z}_u) = (1.555676 \times 10^{-4}, 3.199267)$. We make the assumption in Eq. (E45) that the metallicity dependence of the f_w^2 integral grows linearly with time up to t_{HHe2} and then use the fitting functions provided in Table 5 to approximate the f_w^2 integrals at later times.

The FIRE-3 metal yield is modeled as

$$f_Z(t) = Z_* + (1 - Z_*) y_{\text{HeC}}(t) - X_* y_{\text{HHe}}(t) y_{\text{HeC}}(t), \quad (\text{E47})$$

with the corresponding integrated metal mass loss

$$\begin{aligned} \frac{\Delta M_Z^w}{M_*} &= Z_* \frac{\Delta M_T^w}{M_*} + (1 - Z_*) \int_{t_0}^{t_1} f_w(t) y_{\text{HeC}}(t) dt \\ &- X_* \int_{t_0}^{t_1} f_w(t) y_{\text{HHe}}(t) y_{\text{HeC}}(t) dt. \end{aligned} \quad (\text{E48})$$

The first integral was solved previously in Eq. (E43) while the second integral evaluates to

$$\begin{aligned}
\int_{t_0}^{t_1} f_w y_{\text{HHe}} y_{\text{HeC}} dt &= F_{000}(0, t_{w_1}) \\
&+ F_{100}(t_{w_1}, t_{\text{HHe}_1}) + F_{110}(t_{\text{HHe}_1}, t_{w_2}) \\
&+ F_{210}(t_{w_2}, t_{\text{HeC}_1}) + F_{211}(t_{\text{HeC}_1}, t_{\text{HHe}_2}) \\
&+ F_{221}(t_{\text{HHe}_2}, t_{w_3}) + F_{321}(t_{w_3}, t_{\text{HeC}_2}) \\
&+ F_{322}(t_{\text{HeC}_2}, t_{\text{HHe}_3}) + F_{332}(t_{\text{HHe}_3}, t_{\text{HHe}_4}) \\
&+ F_{342}(t_{\text{HHe}_4}, t_{\text{HeC}_3}) + F_{343}(t_{\text{HeC}_3}, t_{\text{HeC}_4}) \\
&+ G(\tilde{Z}_*) \frac{t}{t_{\text{HHe}_2}} \bigg|_{[0, t_0, t_{\text{HHe}_2}]}^{[0, t_1, t_{\text{HHe}_2}]} \\
&+ \int_{\max(t_0, t_{\text{HHe}_2})}^{\max(t_1, t_{\text{HHe}_2})} f_w^{2a} y_{\text{HHe}} y_{\text{HeC}} dt \\
&+ \int_{\max(t_0, t_{\text{HHe}_2})}^{\max(t_1, t_{\text{HHe}_2})} f_w^{2b} y_{\text{HHe}} y_{\text{HeC}} dt, \quad (\text{E49})
\end{aligned}$$

where

$$\begin{aligned}
F_{ijk}(t_l, t_u) &= \frac{a_{w_i} a_{\text{HHe}_j} a_{\text{HeC}_k}}{\alpha_{ijk} + 1} \times \\
&\frac{t^{\alpha_{ijk} + 1}}{t_{w_i}^{c_{w_i}} t_{\text{HHe}_j}^{c_{\text{HHe}_j}} t_{\text{HeC}_k}^{c_{\text{HeC}_k}}} \bigg|_{[t_l, t_0, t_u]}^{[t_l, t_1, t_u]}, \quad (\text{E50})
\end{aligned}$$

and $\alpha_{ijk} \equiv c_{w_i} + c_{\text{HHe}_j} + c_{\text{HeC}_k}$. We model the metallicity dependence in the same manner as before, with the best-fit coefficients to $G(\tilde{Z}_*)$ being $(g_l, g_1, g_2, g_3, g_4, g_u) = (-17.61843, -17.61708, 0.007352, 0.007056, -9.173174, -16.78266)$ and $(\tilde{z}_l, \tilde{z}_u) = (9.545485 \times 10^{-5}, 3.199267)$. Fitting functions for the remaining two f_w^2 integrals are provided in Table 5.

E.3. Initial Versus Evolved Mass

We note that the integrals provided above assumed that the stellar mass, M_* , in Eqs. (42) and (43) is constant and equal to its initial value at time $t = 0$. In FIRE3, the rates are instead normalized so that the mass loss equations can be evaluated using the time-evolving $M_*(t)$. To account for this, we introduce a correction factor,

$$\alpha^{\text{enrich}} = M_*(t_0) \frac{1 - \exp[-\Delta M_T^{\text{enrich}}/M_*(t_0)]}{\Delta M_T^{\text{enrich}}}, \quad (\text{E51})$$

where $M_*(t_0)$ is the SSP mass at the start of the timestep, and $\Delta M_T^{\text{enrich}}$ is the total mass lost due to supernovae and stellar winds computed using the formulae provided above for $M_*(t = 0)$. The correction factor is derived by separating variables in Eqs. (42) and (43) and using $\int dM/M = \ln M$. The mass loss for each individual component, $\Delta M_c^{\text{enrich}}$, is corrected by multiplication

with α^{enrich} . This correction is analytically exact in the case of the total mass and we find that it is accurate to within 2% for the helium and metal components.

Table 5. Fitting coefficients of the numerical integrals used in the FIRE-3 AGB stellar wind mass loss. Each integral is fit in log-space with a piecewise series of straight line segments, $\exp[a + b \ln t]$, and tanh functions, $\exp[a + b \tanh(c(\ln t - d))]$. Rows with empty entries in the c and d columns indicate a straight-line fit; otherwise, the tanh function applies. The lower and upper time bounds of each piecewise fit, t_l and t_u , are provided in Myr.

| Integral | a | b | c | d | t_l | t_u |
|--|-----------|----------|----------|----------|-------|----------|
| $\int_0^t f_w^{2a}(t) dt$ | -431.99 | 66.81093 | | | 0 | 600 |
| | -96.7544 | 100.0 | 2.43306 | 5.73977 | 600 | 900 |
| | -95.70486 | 100.0 | 1.254149 | 5.00497 | 900 | 1800 |
| | -2.458194 | 0.849421 | | | 1800 | 2400 |
| | -0.530956 | 0.601807 | | | 2400 | 3200 |
| | 0.992478 | 0.413051 | | | 3200 | 4800 |
| | 2.20617 | 0.269867 | | | 4800 | 8000 |
| | 2.9763 | 0.184177 | | | 8000 | ∞ |
| $\int_0^t f_w^{2b}(t) dt$ | -5.2309 | 1.395576 | | | 0 | 20 |
| | -4.877508 | 1.277652 | | | 20 | 50 |
| | -2.980048 | 4.863875 | 0.421655 | 2.123926 | 50 | ∞ |
| $\int_0^t f_w^{2a}(t) y_{\text{HeC}}(t) dt$ | -390.0083 | 59.29077 | | | 0 | 600 |
| | -102.7369 | 100.0 | 2.403543 | 5.7355 | 600 | 900 |
| | -101.5443 | 100.0 | 1.182235 | 4.931659 | 900 | 1800 |
| | -9.3368 | 0.977616 | | | 1800 | 2400 |
| | -7.38478 | 0.726819 | | | 2400 | 3200 |
| | -5.7873 | 0.528893 | | | 3200 | 4800 |
| | -4.4839 | 0.375126 | | | 4800 | 8000 |
| | -3.600583 | 0.276840 | | | 8000 | ∞ |
| $\int_0^t f_w^{2b}(t) y_{\text{HeC}}(t) dt$ | -25.49524 | 4.672025 | | | 0 | 22 |
| | -9.886332 | 3.693667 | 1.291699 | 3.344415 | 22 | 65 |
| | -39.50205 | 34.87625 | 0.402449 | 0 | 65 | 700 |
| | -6.56253 | 0.241310 | | | 700 | 2000 |
| | -5.69778 | 0.127541 | | | 2000 | ∞ |
| $\int_{10}^t f_w^{2a}(t) y_{\text{HHe}}(t) dt$ | -434.459 | 66.78649 | | | 10 | 600 |
| | -99.392 | 100.0 | 2.435569 | 5.740131 | 600 | 900 |
| | -98.35381 | 100.0 | 1.260357 | 5.010987 | 900 | 2000 |
| | -4.663074 | 0.791674 | | | 2000 | 2500 |
| | -1.685144 | 0.411062 | | | 2500 | 3200 |
| | -0.50251 | 0.264532 | | | 3200 | 4800 |
| | 0.19617 | 0.182106 | | | 4800 | 8000 |
| | 0.678 | 0.128502 | | | 8000 | ∞ |
| $\int_{10}^t f_w^{2b}(t) y_{\text{HHe}}(t) dt$ | -103.755 | 100.0 | 1.611936 | 1.072965 | 10 | 18 |
| | -6.93124 | 6.186073 | 0.427509 | 1.83905 | 18 | ∞ |
| $\int_{10}^t f_w^{2a}(t) y_{\text{HHe}}(t) y_{\text{HeC}}(t) dt$ | -334.945 | 50.2729 | | | 10 | 600 |
| | -105.3747 | 100.0 | 2.406011 | 5.735859 | 600 | 900 |
| | -104.1948 | 100.0 | 1.188165 | 4.937966 | 900 | 2000 |
| | -11.53772 | 0.919162 | | | 2000 | 2500 |
| | -8.25936 | 0.500152 | | | 2500 | 3200 |
| | -7.0058 | 0.344835 | | | 3200 | 4800 |
| | -6.29761 | 0.261287 | | | 4800 | 8000 |
| | -5.759975 | 0.201465 | | | 8000 | ∞ |
| $\int_{10}^t f_w^{2b}(t) y_{\text{HHe}}(t) y_{\text{HeC}}(t) dt$ | -59.9234 | 17.13235 | | | 10 | 12.5 |
| | -30.05034 | 5.304919 | | | 12.5 | 22.5 |
| | -12.57509 | 3.888042 | 1.229671 | 3.318168 | 22.5 | 75 |
| | -42.61491 | 35.40138 | 0.404669 | 0.0 | 75 | 1000 |
| | -8.81622 | 0.193901 | | | 1000 | 2500 |
| | -7.87374 | 0.073443 | | | 2500 | ∞ |

REFERENCES

- Angulo, R. E., & Hahn, O. 2021, arXiv preprint arXiv:2112.05165
- Bahé, Y. M., Schaye, J., Schaller, M., et al. 2022, *Monthly Notices of the Royal Astronomical Society*, 516, 167
- Bassini, L., Feldmann, R., Gensior, J., et al. 2024, *Monthly Notices of the Royal Astronomical Society: Letters*, 532, L14
- Beck, A. M., Murante, G., Arth, A., et al. 2016, *Monthly Notices of the Royal Astronomical Society*, 455, 2110
- Behroozi, P., Hearin, A., & Moster, B. P. 2022, *Monthly Notices of the Royal Astronomical Society*, 509, 2800
- Behroozi, P., Wechsler, R. H., Hearin, A. P., & Conroy, C. 2019, *Monthly Notices of the Royal Astronomical Society*, 488, 3143
- Belfiore, F., Maiolino, R., Bundy, K., et al. 2018, *Monthly Notices of the Royal Astronomical Society*, 477, 3014
- Bernardi, M., Meert, A., Sheth, R. K., et al. 2017, *Monthly Notices of the Royal Astronomical Society*, 467, 2217
- Bondi, H., & Hoyle, F. 1944, *Monthly Notices of the Royal Astronomical Society*, 104, 273
- Booth, C., & Schaye, J. 2009, *Monthly Notices of the Royal Astronomical Society*, 398, 53
- Bouwens, R. J., Illingworth, G., Oesch, P., et al. 2015, *The Astrophysical Journal*, 803, 34
- Bower, R. G., Vernon, I., Goldstein, M., et al. 2010, *Monthly Notices of the Royal Astronomical Society*, 407, 2017
- Braspenning, J., Schaye, J., Schaller, M., et al. 2024, *Monthly Notices of the Royal Astronomical Society*, 533, 2656
- Chabrier, G. 2003, *Publications of the Astronomical Society of the Pacific*, 115, 763
- Chaikin, E., Schaye, J., Schaller, M., et al. 2025a, arXiv preprint arXiv:2509.04067
- . 2025b, arXiv preprint arXiv:2509.07960
- CHEX-MATE Collaboration, Arnaud, M., Ettori, S., et al. 2021, *A&A*, 650, A104, doi: [10.1051/0004-6361/202039632](https://doi.org/10.1051/0004-6361/202039632)
- Child, H. L., Habib, S., Heitmann, K., et al. 2018, *The Astrophysical Journal*, 859, 55
- Chisari, E., Mead, A. J., Joudaki, S., et al. 2019, *The Open Journal of Astrophysics*, 2, doi: [10.21105/astro.1905.06082](https://doi.org/10.21105/astro.1905.06082)
- Conroy, C., & Gunn, J. E. 2010, *The Astrophysical Journal*, 712, 833
- Conroy, C., Gunn, J. E., & White, M. 2009, *The Astrophysical Journal*, 699, 486
- Copeland, D., Taylor, A., & Hall, A. 2018, *Monthly Notices of the Royal Astronomical Society*, 480, 2247
- Crain, R. A., & van de Voort, F. 2023, *Annual Review of Astronomy and Astrophysics*, 61, 473
- Cristallo, S., Straniero, O., Piersanti, L., & Gobrecht, D. 2015, *The Astrophysical Journal Supplement Series*, 219, 40
- Curti, M., Mannucci, F., Cresci, G., & Maiolino, R. 2020, *Monthly Notices of the Royal Astronomical Society*, 491, 944
- Daddi, E., Dickinson, M., Morrison, G., et al. 2007, *The Astrophysical Journal*, 670, 156
- Dalla Vecchia, C., & Schaye, J. 2008, *Monthly Notices of the Royal Astronomical Society*, 387, 1431
- Davé, R., Anglés-Alcázar, D., Narayanan, D., et al. 2019, *Monthly Notices of the Royal Astronomical Society*, 486, 2827
- Davies, L., Robotham, A., Lagos, C. d. P., et al. 2019, *Monthly Notices of the Royal Astronomical Society*, 483, 5444
- Davis, M., Efstathiou, G., Frenk, C. S., & White, S. D. 1985, *The Astrophysical Journal*, 292, 371
- De Graaff, A., Trayford, J., Franx, M., et al. 2022, *Monthly Notices of the Royal Astronomical Society*, 511, 2544
- Di Matteo, T., Colberg, J., Springel, V., Hernquist, L., & Sijacki, D. 2008, *The Astrophysical Journal*, 676, 33
- Dib, S., Bell, E., & Burkert, A. 2006, *The Astrophysical Journal*, 638, 797
- Donnari, M., Pillepich, A., Nelson, D., et al. 2021, *Monthly Notices of the Royal Astronomical Society*, 506, 4760
- . 2019, *Monthly Notices of the Royal Astronomical Society*, 485, 4817
- Driver, S. P., Andrews, S. K., Da Cunha, E., et al. 2018, *Monthly Notices of the Royal Astronomical Society*, 475, 2891
- Driver, S. P., Bellstedt, S., Robotham, A. S., et al. 2022, *Monthly Notices of the Royal Astronomical Society*, 513, 439
- Du, P., Zhang, Z.-X., Wang, K., et al. 2018, *The Astrophysical Journal*, 856, 6
- Dubois, Y., Pichon, C., Welker, C., et al. 2014, *Monthly Notices of the Royal Astronomical Society*, 444, 1453
- Durier, F., & Dalla Vecchia, C. 2011, *Monthly Notices of the Royal Astronomical Society*, 419, 465
- Eckert, D., Ghirardini, V., Ettori, S., et al. 2019, *Astronomy & Astrophysics*, 621, A40
- Ester, M., Kriegel, H.-P., Sander, J., & Xu, X. 1996, *Proceedings of the Second International Conference on Knowledge Discovery and Data Mining*, 226
- Fabian, A. C. 2012, *Annual Review of Astronomy and Astrophysics*, 50, 455

- Faucher-Giguère, C.-A. 2020, *Monthly Notices of the Royal Astronomical Society*, 493, 1614 [FG20]
- Ferland, G., Chatzikos, M., Guzmán, F., et al. 2017, *Revista mexicana de astronomía y astrofísica*, 53
- Frontiere, N., Emberson, J. D., Buehlmann, M., et al. 2023, *The Astrophysical Journal Supplement Series*, 264, 34 [FRO23]
- Frontiere, N., Raskin, C. D., & Owen, J. M. 2017, *Journal of Computational Physics*, 332, 160 [FRO17]
- Frontiere, N., Emberson, J., Buehlmann, M., et al. 2025, in *Proceedings of the International Conference for High Performance Computing, Networking, Storage and Analysis, SC '25* (New York, NY, USA: Association for Computing Machinery), 25–35, doi: [10.1145/3712285.3771786](https://doi.org/10.1145/3712285.3771786)
- Furlong, M., Bower, R., Theuns, T., et al. 2015, *Monthly Notices of the Royal Astronomical Society*, 450, 4486
- Furlong, M., Bower, R., Crain, R., et al. 2016, *Monthly Notices of the Royal Astronomical Society*, stw2740
- Gallazzi, A., Bell, E. F., Zibetti, S., Brinchmann, J., & Kelson, D. D. 2014, *The Astrophysical Journal*, 788, 72
- Gallazzi, A., Charlot, S., Brinchmann, J., White, S. D., & Tremonti, C. A. 2005, *Monthly Notices of the Royal Astronomical Society*, 362, 41
- Ghirardini, V., Eckert, D., Etti, S., et al. 2019, *Astronomy & Astrophysics*, 621, A41
- Ghirardini, V., Bulbul, E., Kraft, R., et al. 2021, *The Astrophysical Journal*, 910, 14
- Graham, A. W., & Sahu, N. 2023, *Monthly Notices of the Royal Astronomical Society*, 518, 2177
- Grevesse, N., & Sauval, A. 1998, *Space Science Reviews*, 85, 161
- Haardt, F., & Madau, P. 2012, *The Astrophysical Journal*, 746, 125 [HM12]
- Habib, S., Pope, A., Finkel, H., et al. 2016, *New Astronomy*, 42, 49
- Hardwick, J. A., Cortese, L., Obreschkow, D., Catinella, B., & Cook, R. H. 2022, *Monthly Notices of the Royal Astronomical Society*, 509, 3751
- Harnois-Déraps, J., van Waerbeke, L., Viola, M., & Heymans, C. 2015, *Monthly Notices of the Royal Astronomical Society*, 450, 1212
- Heckman, T. M., & Best, P. N. 2014, *Annual Review of Astronomy and Astrophysics*, 52, 589
- Hernquist, L., & Katz, N. 1989, *ApJS*, 70, 419, doi: [10.1086/191344](https://doi.org/10.1086/191344)
- Hirschmann, M., Dolag, K., Saro, A., et al. 2014, *Monthly Notices of the Royal Astronomical Society*, 442, 2304
- Holweger, H. 2001, *AIP Conference Proceedings*, 598, 23, doi: [10.1063/1.1433974](https://doi.org/10.1063/1.1433974)
- Hopkins, P. F., & Quataert, E. 2010, *Monthly Notices of the Royal Astronomical Society*, 407, 1529
- Hopkins, P. F., Wetzel, A., Kereš, D., et al. 2018, *Monthly Notices of the Royal Astronomical Society*, 480, 800
- Hopkins, P. F., Wetzel, A., Wheeler, C., et al. 2023, *MNRAS*, 519, 3154 [FIRE3]
- Hoyle, F., & Lyttleton, R. A. 1939, in *Mathematical Proceedings of the Cambridge Philosophical Society*, Vol. 35, Cambridge University Press, 405–415
- Huang, S., Katz, N., Davé, R., et al. 2019, *Monthly Notices of the Royal Astronomical Society*, 484, 2021
- Ikeuchi, S., & Ostriker, J. 1986, *Astrophysical Journal*, Part 1 (ISSN 0004-637X), vol. 301, Feb. 15, 1986, p. 522-543., 301, 522
- Jiang, Y.-F., Blaes, O., Stone, J. M., & Davis, S. W. 2019, *The Astrophysical Journal*, 885, 144
- Jo, Y., Genel, S., Wandelt, B., et al. 2023, *The Astrophysical Journal*, 944, 67
- Katz, N., Weinberg, D. H., & Hernquist, L. 1995, arXiv preprint astro-ph/9509107
- Klypin, A., Kravtsov, A. V., Bullock, J. S., & Primack, J. R. 2001, *The Astrophysical Journal*, 554, 903
- Klypin, A. A., & Shandarin, S. F. 1983, *Monthly Notices of the Royal Astronomical Society*, 204, 891
- Komatsu, E., Smith, K. M., Dunkley, J., et al. 2011, *The Astrophysical Journal Supplement Series*, 192, 18, doi: [10.1088/0067-0049/192/2/18](https://doi.org/10.1088/0067-0049/192/2/18)
- Koprowski, M., Wijesekera, J., Dunlop, J., et al. 2024, *Astronomy & Astrophysics*, 691, A164
- Kormendy, J., & Ho, L. C. 2013, *Annual Review of Astronomy and Astrophysics*, 51, 511
- Kravtsov, A., Vikhlinin, A., & Meshcheryakov, A. 2018, *Astronomy Letters*, 44, 8
- Kroupa, P. 2001, *Monthly Notices of the Royal Astronomical Society*, 322, 231
- Kugel, R., Schaye, J., Schaller, M., et al. 2023, *Monthly Notices of the Royal Astronomical Society*, 526, 6103
- Lacey, C., & Cole, S. 1994, *Monthly Notices of the Royal Astronomical Society*, 271, 676
- Lebrun-Grandié, D., Prokopenko, A., Turcksin, B., & Slattery, S. R. 2020, *ACM Trans. Math. Softw.*, 47, doi: [10.1145/3412558](https://doi.org/10.1145/3412558)
- Lehle, K., Nelson, D., Pillepich, A., Truong, N., & Rohr, E. 2024, *A&A*, 687, A129, doi: [10.1051/0004-6361/202348609](https://doi.org/10.1051/0004-6361/202348609)
- Leitherer, C., Ekström, S., Meynet, G., et al. 2014, *The Astrophysical Journal Supplement Series*, 212, 14
- Leja, J., Van Dokkum, P. G., Franx, M., & Whitaker, K. E. 2015, *The Astrophysical Journal*, 798, 115

- Leja, J., Speagle, J. S., Ting, Y.-S., et al. 2022, *The Astrophysical Journal*, 936, 165
- Leslie, S. K., Schinnerer, E., Liu, D., et al. 2020, *The Astrophysical Journal*, 899, 58
- Leung, S.-C., & Nomoto, K. 2018, *The Astrophysical Journal*, 861, 143
- Li, Q., Cui, W., Yang, X., et al. 2023, *Monthly Notices of the Royal Astronomical Society*, 523, 1228
- Limongi, M., & Chieffi, A. 2018, *The Astrophysical Journal Supplement Series*, 237, 13
- Lovisari, L., Reiprich, T., & Schellenberger, G. 2015, *Astronomy & Astrophysics*, 573, A118
- Lyskova, N., Churazov, E., Khabibullin, I., et al. 2023, *Monthly Notices of the Royal Astronomical Society*, 525, 898
- Madau, P., & Dickinson, M. 2014, *Annual Review of Astronomy and Astrophysics*, 52, 415
- Maoz, D., & Graur, O. 2017, *The Astrophysical Journal*, 848, 25
- McCarthy, I. G., Schaye, J., Bird, S., & Le Brun, A. M. C. 2016, *Monthly Notices of the Royal Astronomical Society*, stw2792
- McDonald, M., Allen, S., Bayliss, M., et al. 2017, *The Astrophysical Journal*, 843, 28
- McKee, C. F., & Ostriker, J. P. 1977, *Astrophysical Journal*, Part 1, vol. 218, Nov. 15, 1977, p. 148-169., 218, 148
- Moster, B. P., Naab, T., & White, S. D. 2013, *Monthly Notices of the Royal Astronomical Society*, 428, 3121
- . 2018, *Monthly Notices of the Royal Astronomical Society*, 477, 1822
- Muzzin, A., Marchesini, D., Stefanon, M., et al. 2013, *The Astrophysical Journal*, 777, 18
- Naab, T., & Ostriker, J. P. 2017, *Annual review of astronomy and astrophysics*, 55, 59
- Nagaraj, G., Forbes, J. C., Leja, J., Foreman-Mackey, D., & Hayward, C. C. 2022, *The Astrophysical Journal*, 932, 54
- Nelson, D., Pillepich, A., Springel, V., et al. 2017, *Monthly Notices of the Royal Astronomical Society*, 475, 624, doi: [10.1093/mnras/stx3040](https://doi.org/10.1093/mnras/stx3040)
- Nelson, D., Springel, V., Pillepich, A., et al. 2019, *Computational Astrophysics and Cosmology*, 6, 2
- Novak, M., Smolčić, V., Delhaize, J., et al. 2017, *Astronomy & astrophysics*, 602, A5
- Oppenheimer, B. D., & Davé, R. 2006, *Monthly Notices of the Royal Astronomical Society*, 373, 1265
- Owen, J. M., Weinberg, D. H., & Villumsen, J. V. 1998, *arXiv preprint astro-ph/9805097*
- Pacifici, C., Kassin, S. A., Weiner, B. J., et al. 2016, *The Astrophysical Journal*, 832, 79
- Pakmor, R., Springel, V., Coles, J. P., et al. 2023, *Monthly Notices of the Royal Astronomical Society*, 524, 2539
- Pawlik, A. H., & Schaye, J. 2008, *Monthly Notices of the Royal Astronomical Society*, 389, 651
- . 2011, *Monthly Notices of the Royal Astronomical Society*, 412, 1943
- Pike, S. R., Kay, S. T., Newton, R. D., Thomas, P. A., & Jenkins, A. 2014, *Monthly Notices of the Royal Astronomical Society*, 445, 1774
- Pillepich, A., Springel, V., Nelson, D., et al. 2018a, *Monthly Notices of the Royal Astronomical Society*, 473, 4077
- Pillepich, A., Nelson, D., Hernquist, L., et al. 2018b, *Monthly Notices of the Royal Astronomical Society*, 475, 648
- Planck Collaboration, Aghanim, N., Akrami, Y., et al. 2020, *A&A*, 641, A6, doi: [10.1051/0004-6361/201833910](https://doi.org/10.1051/0004-6361/201833910)
- Popesso, P., Concas, A., Cresci, G., et al. 2023, *Monthly Notices of the Royal Astronomical Society*, 519, 1526
- Popesso, P., Biviano, A., Marini, I., et al. 2024, *arXiv preprint arXiv:2411.16555*
- Prada, F., Klypin, A. A., Cuesta, A. J., Betancort-Rijo, J. E., & Primack, J. 2012, *Monthly Notices of the Royal Astronomical Society*, 423, 3018
- Pratt, G., Arnaud, M., Biviano, A., et al. 2019, *Space Science Reviews*, 215, 25
- Pratt, G., Croston, J. H., Arnaud, M., & Böhringer, H. 2009, *Astronomy & Astrophysics*, 498, 361
- Prieto, C. A., Lambert, D. L., & Asplund, M. 2001, *The Astrophysical Journal*, 556, L63
- . 2002, *The Astrophysical Journal*, 573, L137
- Prokopenko, A., Arndt, D., Lebrun-Grandié, D., et al. 2025, *The International Journal of High Performance Computing Applications*, 39, 167, doi: [10.1177/10943420241298296](https://doi.org/10.1177/10943420241298296)
- Rahmati, A., Pawlik, A. H., Raičević, M., & Schaye, J. 2013, *Monthly Notices of the Royal Astronomical Society*, 430, 2427
- Saitoh, T. R., & Makino, J. 2009, *The Astrophysical Journal Letters*, 697, L99
- Sanders, R. L., Shapley, A. E., Jones, T., et al. 2021, *The Astrophysical Journal*, 914, 19
- Schaye, J., & Dalla Vecchia, C. 2008, *Monthly Notices of the Royal Astronomical Society*, 383, 1210
- Schaye, J., Vecchia, C. D., Booth, C., et al. 2010, *Monthly Notices of the Royal Astronomical Society*, 402, 1536
- Schaye, J., Crain, R. A., Bower, R. G., et al. 2015, *Monthly Notices of the Royal Astronomical Society*, 446, 521
- Schaye, J., Kugel, R., Schaller, M., et al. 2023, *Monthly Notices of the Royal Astronomical Society*, 526, 4978

- Schaye, J., Chaikin, E., Schaller, M., et al. 2025, arXiv preprint arXiv:2508.21126
- Sembolini, F., Yepes, G., De Petris, M., et al. 2013, *Monthly Notices of the Royal Astronomical Society*, 429, 323
- Sembolini, F., Yepes, G., Pearce, F. R., et al. 2016a, *Monthly Notices of the Royal Astronomical Society*, 457, 4063, doi: [10.1093/mnras/stw250](https://doi.org/10.1093/mnras/stw250)
- Sembolini, F., Elahi, P. J., Pearce, F. R., et al. 2016b, *Monthly Notices of the Royal Astronomical Society*, 459, 2973, doi: [10.1093/mnras/stw800](https://doi.org/10.1093/mnras/stw800)
- Shuntov, M., Ilbert, O., Toft, S., et al. 2025, *Astronomy & Astrophysics*, 695, A20
- Sijacki, D., Springel, V., Di Matteo, T., & Hernquist, L. 2007, *Monthly Notices of the Royal Astronomical Society*, 380, 877
- Smith, B., Sigurdsson, S., & Abel, T. 2008, *Monthly Notices of the Royal Astronomical Society*, 385, 1443
- Smith, B. D., Bryan, G. L., Glover, S. C., et al. 2017, *Monthly Notices of the Royal Astronomical Society*, 466, 2217
- Somerville, R. S., & Davé, R. 2015, *Annual Review of Astronomy and Astrophysics*, 53, 51
- Springel, V. 2010, *Monthly Notices of the Royal Astronomical Society*, 401, 791
- Springel, V., Di Matteo, T., & Hernquist, L. 2005, *Monthly Notices of the Royal Astronomical Society*, 361, 776
- Springel, V., & Hernquist, L. 2003, *Monthly Notices of the Royal Astronomical Society*, 339, 289 [SH03]
- Springel, V., Yoshida, N., & White, S. D. 2001, *New Astronomy*, 6, 79
- Strang, G. 1968, *SIAM journal on numerical analysis*, 5, 506
- Sukhbold, T., Ertl, T., Woosley, S., Brown, J. M., & Janka, H.-T. 2016, *The Astrophysical Journal*, 821, 38
- Sultan, I., Faucher-Giguère, C.-A., Stern, J., et al. 2025, *Monthly Notices of the Royal Astronomical Society*, 540, 1017
- Sun, M., Voit, G., Donahue, M., et al. 2009, *The Astrophysical Journal*, 693, 1142
- Teyssier, R. 2002, *Astronomy & Astrophysics*, 385, 337
- Thacker, R., Tittley, E., Pearce, F., Couchman, H., & Thomas, P. 2000, *Monthly Notices of the Royal Astronomical Society*, 319, 619
- Thomas, N., Davé, R., Anglés-Alcázar, D., & Jarvis, M. 2019, *Monthly Notices of the Royal Astronomical Society*, 487, 5764
- Thorne, J. E., Robotham, A. S., Davies, L. J., et al. 2021, *Monthly Notices of the Royal Astronomical Society*, 505, 540
- Tomczak, A. R., Quadri, R. F., Tran, K.-V. H., et al. 2016, *The Astrophysical Journal*, 817, 118
- Torrey, P., Vogelsberger, M., Marinacci, F., et al. 2019, *Monthly Notices of the Royal Astronomical Society*, 484, 5587, doi: [10.1093/mnras/stz243](https://doi.org/10.1093/mnras/stz243)
- Townsend, R. 2009, *The Astrophysical Journal Supplement Series*, 181, 391
- Traina, A., Gruppioni, C., Delvecchio, I., et al. 2024, *Astronomy & Astrophysics*, 681, A118
- Tremmel, M., Governato, F., Volonteri, M., & Quinn, T. R. 2015, *Monthly Notices of the Royal Astronomical Society*, 451, 1868
- Tremonti, C. A., Heckman, T. M., Kauffmann, G., et al. 2004, *The Astrophysical Journal*, 613, 898
- van Daalen, M. P., Schaye, J., Booth, C., & Dalla Vecchia, C. 2011, *Monthly Notices of the Royal Astronomical Society*, 415, 3649
- Vikhlinin, A., Burenin, R., Ebeling, H., et al. 2009, *The Astrophysical Journal*, 692, 1033
- Vogelsberger, M., Genel, S., Sijacki, D., et al. 2013, *Monthly Notices of the Royal Astronomical Society*, 436, 3031
- Vogelsberger, M., Marinacci, F., Torrey, P., & Puchwein, E. 2020, *Nature Reviews Physics*, 2, 42
- Wang, E., Wang, H., Mo, H., et al. 2018, *The Astrophysical Journal*, 860, 102
- Weaver, J. R., Davidzon, I., Toft, S., et al. 2023, *A&A*, 677, A184, doi: [10.1051/0004-6361/202245581](https://doi.org/10.1051/0004-6361/202245581)
- Weinberger, R., Springel, V., Hernquist, L., et al. 2016, *Monthly Notices of the Royal Astronomical Society*, 465, 3291
- Wendland, H. 1995, *Advances in Computational Mathematics*, 4, 389
- Wetzel, A. R., Tinker, J. L., Conroy, C., & Van Den Bosch, F. C. 2013, *Monthly Notices of the Royal Astronomical Society*, 432, 336
- Widynski, B. 2020, arXiv preprint arXiv:2004.06278
- Wiersma, R. P., Schaye, J., & Smith, B. D. 2009, *Monthly Notices of the Royal Astronomical Society*, 393, 99
- Wilkins, S. M., Trentham, N., & Hopkins, A. M. 2008, *Monthly Notices of the Royal Astronomical Society*, 385, 687
- Yu, H., & Wang, F. 2016, *The Astrophysical Journal*, 820, 114
- Zahid, H. J., Dima, G. I., Kewley, L. J., Erb, D. K., & Davé, R. 2012, *The Astrophysical Journal*, 757, 54
- Zahid, H. J., Dima, G. I., Kudritzki, R.-P., et al. 2014, *The Astrophysical Journal*, 791, 130